NASA Technical Memorandum 4323

A Thermal/Nonthermal Approach to Solar Flares

Stephen G. Benka

DECEMBER 1991

(NASA-TM-4323)   A THERMAL/NONTHERMAL   N92-14955
APPROACH TO SOLAR FLARES   (NASA)   109 p
                              CSCL 03B
                                              Unclas
                                      H1/92   0053402

NASA Technical Memorandum 4323

A Thermal/Nonthermal Approach to Solar Flares

Stephen G. Benka
Goddard Space Flight Center
Greenbelt, Maryland

PAGE ____ INTENTIONALLY BLANK

Stephen G. Benka
A THERMAL/NONTHERMAL APPROACH TO SOLAR FLARES
(under the direction of Gordon D. Holman and Wayne A. Christiansen)

ABSTRACT

A new approach for modeling solar flare high energy emissions is developed in which both thermal and nonthermal particles coexist and contribute to the radiation. The thermal/nonthermal distribution function is interpreted physically by postulating the existence of DC current sheets in the flare region. These current sheets then provide both primary plasma heating through Joule dissipation, and runaway electron acceleration. The physics of runaway acceleration is discussed. Several methods are presented for obtaining approximations to the thermal/nonthermal distribution function, both within the current sheets and outside of them. Theoretical hard X-ray spectra are calculated, allowing for thermal bremsstrahlung from the heated plasma external to the current sheets, as well as thick-target bremsstrahlung from runaway electrons impinging on the chromosphere. A simple model for hard X-ray images of two-ribbon flares is presented. Theoretical microwave gyrosynchrotron spectra are calculated and analyzed, uncovering important new effects caused by the interplay of thermal and nonthermal particles. The theoretical spectra are compared with observed high resolution spectra of solar flares, and excellent agreement is found, in both hard X-rays and microwaves. The future detailed application of this approach to solar flares is discussed, as are possible refinements of this theory.

ACKNOWLEDGEMENTS

Contents

List of Tables

PAGE INTENTIONALLY BLANK

List of Figures

Notation

(**cgs units are used throughout**)

A : Effective Area of emission, either thick-target bremsstrahlung or gyrosynchrotron

$a_{\theta\pm}$: θ-polarization coefficient for the o (+) and x (−) modes, p 64

$AU = 1.5 \times 10^{13}$ cm : 1 Astronomical Unit

B : Magnetic field strength

B_J : Induction Magnetic field strength, p 11

c : Speed of light

D : Line-of-sight depth of microwave emitting source, p 63

e : Charge of electron

E : Electric Field strength

$E_D = p_{th}\nu_{th}/e$: Critical Dreicer electric field, p 10

$\mathcal{E} = (\gamma - 1)mc^2$: Kinetic energy of electron with momentum p, p 11

$\mathcal{E}_{co} = (\gamma_{co} - 1)mc^2$: High energy cutoff for runaway electrons, p 11

$\mathcal{E}_{cr} = (\gamma_{cr} - 1)mc^2$: Critical energy for runaway electron production, p 11

ε : Hard X-ray photon energy

EM : Emission Measure for thermal bremsstrahlung, p 30

$F(\mathcal{E}_o)$: Flux of nonthermal electrons above energy $\mathcal{E}_o$, p 31

$\mathcal{F}(\mathcal{E}_o)$: Energy flux carried by nonthermal electrons, p 31

f : Electron Distribution Function

f_{bg} : Distribution function of background electrons, outside of current sheet, p 15

f_{co} : Distribution function of runaway electrons above $\mathcal{E}_{co}$, p 18

f_{cs} : Distribution function of current sheet electrons, p 15, 22

f_{HdG} : Hakim − deGroot distribution function for drifting electrons, p 22

$f_{Num}(p_{co})$: Normalization factor for f_{rw}, p 16, 17

f_{nt} : Distribution function of nonthermal electrons, p 23

f_{rw} : Distribution function of runaway electrons, p 13, 15, 17

f_{th} : Distribution function of thermal electrons, p 23, 24

f_{tnt} : Distribution function of thermal/nonthermal electrons, p 25

$\bar{g}_{ff}$: Temperature-averaged Gaunt factor for free-free emission, p 30

H-n $\equiv$ Nonthermal microwave enhancement associated with n^{th} harmonic, p 71

$h\nu = \varepsilon$: Hard X-ray photon energy

I : Current, p 11

I : Radiation intensity, for bremsstrahlung, p 30, 31, or gyrosynchrotron, p 63, 64

I_n : Photon flux with $\varepsilon \geq n$ keV, p 52

$\vec{J}$: Current density, p 9

J_s : Bessel function of order s, p 64

$j(\nu)$: Bremsstrahlung emissivity, p 30

$j_\pm$: Gyrosynchrotron emissivity for the o (+) and x (−) modes, p 63, 64

k : Boltzman's constant

L : Length of Current Sheet

$\mathcal{L}$: Loss factor for particles escaping the Current Sheet, p 16, 17

ℓ : Scale length of losses, p 17

m : Mass of electron

$mc^2 = 511\,keV$: Rest energy of an electron

N : Density of plasma particles, usually electrons

N_e , N_i : Density of electrons, i^{th} ionic species

N_{th} , N_{nt} : Density of Thermal, Nonthermal electrons, p 25

N_V : Density of plasma outside of current sheets, p 12

$n_\pm$: Plasma index of refraction for the o (+) and x (−) modes, p 64

NT $\equiv$ NonThermal, p 66

$p = \gamma m v$: Momentum of electron

p_o : Initial momentum, p 13, 14

p_{co} : High energy cutoff momentum in current sheet, p 11

p_{cr} : Critical momentum for electron runaway, p 10

p_{dr} : Current drift momentum, p 9

p_{th} : Thermal momentum of electrons, p 10

PC $\equiv$ "Primary Component" of microwave spectrum, p 71

RJ $\equiv$ Rayleigh-Jeans portion of microwave spectrum, p 71

$r_L = m v_\perp c / eB$: Larmor or gyroradius, p 11

$r_o = e^2/mc^2$: Classical electron radius, p 30

s : Harmonic number, p 65

$\mathcal{S}$: Source function for runaway electrons, p 16

sfu $\equiv$ Solar Flux Unit $= 10^{-19}\,erg\ cm^{-2}\ sec^{-1}\ Hz^{-1}$, p 66

T : Temperature of plasma electrons

$T_\perp$: Measure of perpendicular spreading of f_{rw} from numerical solution, p 17

t_J : Plasma heating time scale, p 12

TH $\equiv$ Thermal, p 66

TNT $\equiv$ Thermal / NonThermal, p 66

V : Plasma volume

V_J : Volume of current sheets, p 12

w : Width of current sheet

$v = p/\gamma m$: Electron velocity

$v_{th} = \sqrt{kT/m}$: Nonrelativistic electron thermal velocity, p 9

x, dx : Position in, element of current sheet

x_o : Retarded position in current sheet, p 17

Z_i : Charge state of ith ionic species, p 11, 30

α : Momentum-dependence of current sheet losses ("Diffusion Index"), p 17

$\beta = p/\gamma mc = v/c$

δ : Spectral index for f_{nt}, p 23

δr : Thickness of current sheet, p 11

$\epsilon = E / E_D$, p 10

$\eta = 1/\sigma$: Electrical resistivity of the plasma, p 32

$\eta_{\pm}$: Single electron gyrosynchrotron emissivity, p 64

Γ : Runaway rate, p 11

$\gamma = \sqrt{(p/mc)^2 + 1}$: Lorentz factor of an electron with momentum p

$\gamma_{co} = \gamma(p_{co}) = \gamma_{cr} + eEL/mc^2$

$\gamma_{cr} = \gamma(p_{cr})$

$\gamma_{th} = \gamma(p_{th})$

$\kappa_{\pm}$: Gyrosynchrotron absorption coefficient for the o (+) and x (−) modes, p 64

$\ln \Lambda$: Coulomb logarithm, p 9

ν : Frequency of microwave radiation

$\nu_b = eB/2\pi mc$: Electron gyrofrequency, p 62, 64

$\nu_p = \sqrt{Ne^2/\pi m}$: Plasma frequency, p 61, 64

ν_{peak} : Peak frequency of microwave spectrum, p 71

$\nu_{th} = 4\pi N me^4 \ln \Lambda/p_{th}^3$: Thermal collision frequency, p 9

$\nu_x = \nu_b/2 + \sqrt{\nu_p^2 + \nu_b^2/4}$: Extraordinary mode cutoff frequency, p 64

ν_1 , ν_2 : Transition frequencies in microwave spectrum, p 70

ϕ : Pitch angle of electron with respect to magnetic field, p 64

Π : Fractional microwave polarization, p 77

$\sigma = Ne^2/m\nu_{th}$: Electrical conductivity of the plasma, p 9

σ_{BH} : Bethe-Heitler cross section for bremsstrahlung, p 31

$\tau_J = \epsilon^{-2}\nu_{th}^{-1}$: Joule heating time scale, p 12

θ : Angle between wave normal and magnetic field, p 63

χ_ν^2 : Reduced chi-square statistic, p 43

ξ : Acceleration distance, p 14, 15

Chapter 1

INTRODUCTION

Solar flares represent one of the most spectacular, powerful, and intriguing phenomena in our solar system. A great flare can release $> 10^{32}$ ergs, much of it explosively, over a period of $\sim 10^3$ seconds, over an area of the sun's surface of perhaps several times 10^{19} cm^2. Great flares can profoundly affect human activities, posing life-threatening hazards to astronauts, disrupting communications both in space and on the ground, and even knocking out entire metropolitan power grids as happened in Toronto, Canada in March of 1989. At the other extreme, microflares have been observed down to the limits of instrumental sensitivity, releasing $\sim 10^{28}$ ergs in just a few seconds. Two recent reviews are Dennis (1988) and Dennis and Schwartz (1989). A good compendium of both observations and theory of solar flares, up to 1988, is found in Tandberg-Hanssen and Emslie (1988). Elaborations on the following background material may be found in these sources.

Almost all flares occur in or near so-called "active regions" on the sun, where several sunspots and complicated magnetic field configurations may be present. Although the actual triggering of a flare has never been observed, it is generally accepted that the source of energy for the flare phenomenon is the magnetic free energy associated with nonpotential (i.e. current carrying) coronal magnetic fields, which are rarely found outside of active regions. Supporting this view is the fact that flares have been observed to occur in locations, within an active region, where highly sheared magnetic fields are present (e.g. Hagyard *et al.* 1984; Venkatakrishnan *et al.* 1988). The magnetic free energy is converted to one or more other forms of energy, in which it manifests itself: (1) radiations spanning the electromagnetic spectrum from decametric radio to > 10 MeV gamma rays; (2) energetic particles including electrons, ions, and neutrons; (3) heating of the local solar plasma up to temperatures perhaps a hundredfold hotter than the quiet corona; and (4) mass motions of solar plasmas including eruptive prominances and coronal mass ejections.

There is a great diversity among flares, above and beyond the energy and time scale differences already mentioned. For instance, some produce copious numbers of interplanetary particles, while others do not. Some produce gamma rays > 1 MeV, others do not. Some flares are visible in white light, most are not. Some flares are associated with a coronal mass ejection while most are not. Any given flare may or may not produce metric radio bursts. Some but not all flares show radiation bursts on a time scale of milliseconds. Some show very smooth time profiles, with

1

no rapid enhancements at all. Although most astronomers think of a solar flare as a well-defined phenomenon, any general description, except in the vaguest and most qualitative terms, is bound to meet numerous observational exceptions.

Despite this great variety of flares, many of them do share *some* common characteristics. Notable is the presence of a so-called "impulsive" phase, shown schematically in Figure 1.1. This phase is characterized by bursts of radiation from highly energized electrons, and signals the "start" of a flare, although some precursory phenomena may be observed first. Often in the largest and longest-lived events, a brief ($\sim$ minutes) impulsive phase initiates the event, later to be followed by a more gradual phase in which the flare slowly decays and emissions of the highest energy electrons are largely absent. Many of the smaller and shorter-lived events are purely impulsive in character. It is widely believed that the impulsively radiating particles derive their energy directly from the primary flare trigger and energy release mechanism itself, and so studying their emissions can help to uncover the underlying physics of flares. Many events show impulsive emission superposed on a more gradually varying emission, leading to the possibility that more than one form of energy release can operate simultaneously.

As depicted in Figure 1.1, the impulsive phase burst emissions can be seen at metric and microwave radio frequencies, at extreme ultraviolet wavelengths, and at hard X-ray energies. The most extensively analyzed of these emissions are hard X-rays ($>$ 10 keV) produced via collisional bremsstrahlung, and microwaves (1-100 GHz) produced via gyrosynchrotron radiation, since the electrons spiral along magnetic field lines in the corona. Although the energies of these radiations are very different (a 10 GHz photon has $\sim 10^{-8}$ keV), electrons of very similar energies are required to produce them, being on the order of tens to few hundred keV. The time profiles of these two impulsive emissions are often very complex, and yet well correlated with each other, as shown in Figure 1.2. They show fast ($\sim$ seconds) rise times from preflare conditions, and "spikey" bursts of radiation which are usually coincident in the two wavelength regimes to within a second or so.

This close correlation suggests that the hard X-rays and microwaves are two manifestations of a single underlying phenomenon. For instance, the electrons which produce these emissions may have been subjected to a common energization mechanism. The connection between the two time profiles has been much investigated (e.g. Marsh *et al.* 1981; Wiehl *et al.* 1985; Lu and Petrosian 1989, 1990; Nitta *et al.* 1991), but no general and compelling explanation has been put forth. Recently, Batchelor (1989, 1990) has uncovered some observational clues about the nature of the microwave/hard X-ray correlation, but it is difficult to interpret what they mean.

The first solar hard X-ray spectra were taken in three energy channels (Anderson and Winckler 1962) The first regular observations of hard X-rays from flares were made with the Orbiting Solar Observatory satellites in the 1960s and 1970s. Spectra were typically taken in 5-10 energy channels between about 25 and 200 keV. Similarly, solar patrol microwave spectra are taken at 3-6 frequencies between 1 GHz and 30 GHz (cf. Kundu 1965; Stäli *et al.* 1989). Because of the low spectral resolution in both wavelength regimes, most analysis to date has focused on the time profiles of the emission, in individual energy or frequency bands.

Nonetheless, models were constructed to fit the spectra as observed. It was
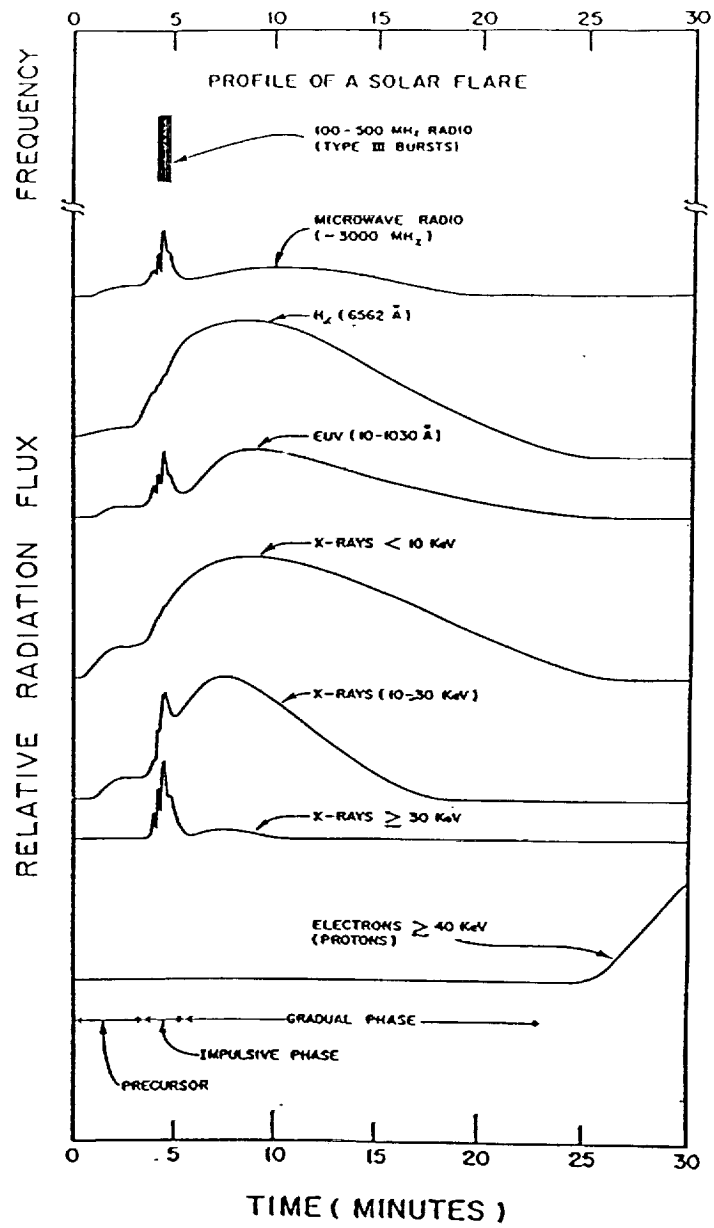
Figure 1.1: A schematic representation of the different phases of a solar flare as observed in the electromagnetic and particle radiation (from Kane 1974)
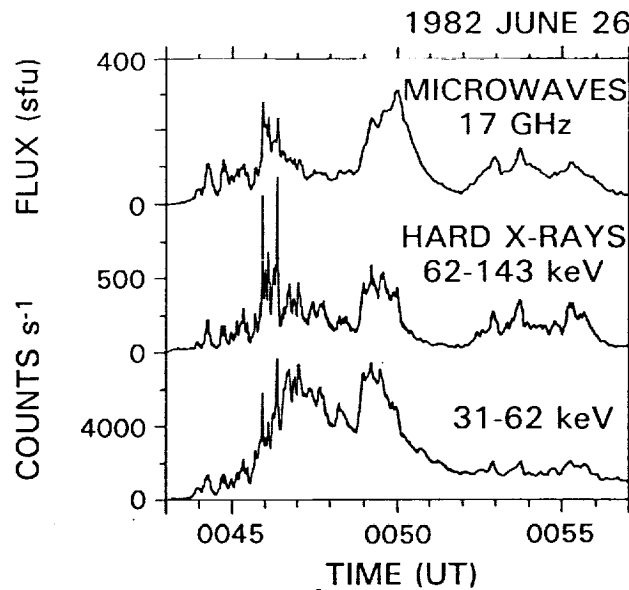
Figure 1.2: A complex impulsive flare showing the close correlation between the hard X-ray and microwave time profiles (from Kosugi, Dennis, and Kai 1988).

found that the steep hard X-ray spectra could be reasonably well fit with either one of two basic models, and the radio observations could be made to be more or less consistent with either.

The first model to arise, dubbed the "thermal" model, postulates that the primary energy release of a solar flare is used to impulsively heat the flaring plasma to temperatures in excess of 10^8 K. The hard X-rays are then interpreted as arising from thermal bremsstrahlung. The general evolution of this model can be traced through: Chubb, *et al.* 1966; Brown 1974; Crannell, *et al.* 1978; Mätzler 1978; Brown, Melrose, and Spicer 1979; Batchelor, *et al.* 1985.

The second model to arise, the "nonthermal" model, is currently favored by most researchers. It postulates that the primary energy release of a solar flare is used to accelerate a large fraction of the electrons in the flaring plasma to suprathermal energies. The hard X-rays are then interpreted as arising from nonthermal bremsstrahlung, in either a thin-target (in the corona), or a thick-target (the electron "beam" enters the chromosphere from the corona). The evolution of this model can be traced through: Holt and Ramaty 1969; Brown 1971; Lin and Hudson 1976; Leach and Petrosian 1981; Lu and Petrosian 1988, 1989.

Recent works have summarized the triumphs and failings of each of these models, both observationally (Dennis 1989) and theoretically (Tandberg-Hanssen and Emslie 1988) and there is no need to do so here. It must be mentioned, however, that to date almost all modeling of flares has employed one or the other of these models, pitting them against each other to determine which of them is most nearly correct. Tandberg-Hanssen and Emslie (1988) put it thusly: "The question is whether the [hard X-ray emitting] electrons form a high-energy component interacting with a

cooler background plasma, or form part of a bulk-energized 'thermal' population. Numerous observational tests to discriminate between these scenarios ...have been devised. However, ...the question remains open, and we can but look forward to more precise observational constraints that future generations of instruments can provide".

Since 1980, observations in both hard X-rays and microwaves have achieved tremendously improved spectral resolution. Hard X-ray spectra obtained with a cooled, high-purity germanium detector (Lin *et al.* 1981; Lin and Schwartz 1987; Emslie *et al.* 1989) have shown the simultaneous presence of thermal and nonthermal components. Such a spectrum cannot be described with either a simple thermal or a simple nonthermal model. Both are required. The high resolution microwave spectra being obtained at Owens Valley Radio Observatory (Stäli *et al.* 1989) similarly show many features that cannot be interpreted in terms of simple thermal or nonthermal models.

It is a fundamental premise of this dissertation that the above-mentioned either/or, thermal or nonthermal, approach to modeling solar flares is overly restrictive and somewhat misguided, as demonstrated by recent sophisticated observations. Indeed, virtually all flare energization mechanisms one might think of will produce *both* plasma heating and particle acceleration. In contrast to the above stated, widely prevalent view of flares and flare modeling, a more accurate assessment is given in Holman *et al.* (1989) which I quote at some length (see also Holman 1986):

> In the past there has been considerable controversy over thermal versus nonthermal models for flare hard X-ray and microwave emission. It is apparent from both observational and theoretical considerations, however, that both heating and particle acceleration will occur in any given flare, and that both thermal and nonthermal processes are likely to contribute to the hard X-ray and microwave emissions. Sorting out the thermal and nonthermal contributions to flare emission is necessary in order to identify the heating and acceleration mechanisms, and the important transport processes that determine the character of the flare emission. Hence, it is important that well-observed flares be analyzed with this in mind, and that future observations be designed with this as a primary goal.

This dissertation explores the possibility of marrying the two previously disparate approaches (viz. thermal and nonthermal), making possible the sorting out of their relative contributions. To accomplish this, I construct a single electron distribution function having both thermal and nonthermal components, and then use it to calculate hard X-ray and/or microwave emission spectra. These theoretical spectra are then compared with, fitted to, and used to interpret, high spectral resolution data in both wavelength regimes.

The thermal/nonthermal distribution function is placed in a physically plausible framework by postulating that the primary flare trigger and energy release mechanism involves the presence of large scale DC electric fields (current sheets) within the flaring coronal plasma. This postulate has the advantage of being fully consistent with the widely held view, mentioned earlier, that flares are powered by the free energy available in current-carrying magnetic fields. In addition to consistency, this

postulate represents perhaps the simplest physics which can simultaneously have both thermal and nonthermal consequences. The current sheets heat the ambient plasma, in which they are embedded, through Joule dissipation. The heated plasma surrounding the current sheets then emits both thermal hard X-ray bremsstrahlung and thermal gyrosynchrotron radiation. At the same time, a fraction of the electrons within the current sheets undergo runaway acceleration. Some of the accelerated electrons penetrate to denser regions of the solar atmosphere, where they emit nonthermal thick-target hard X-ray bremsstrahlung. Others of the accelerated electrons are pitch-angle scattered out of the current sheets, and emit nonthermal gyrosynchrotron radiation. Thus, in this model, there are both thermal and nonthermal aspects to both the hard X-ray and microwave emission that we observe. As we will see, this "unified duality" of the thermal/nonthermal approach leads to some very important observational consequences.

The existence of current sheets is an *a priori* postulate of this dissertation, but the origins of such structures in the solar corona is currently an area of active research (e.g. Syrovatskii 1981; van Ballegooijen 1985; Mikić *et al.* 1989; Karpen *et al.* 1990; Bhattacharjee and Wang 1991). For the development of the thermal/nonthermal model in these pages, the importance of the current sheets is derived from their plasma heating and particle acceleration capabilities, while their precise locations and arrangements are of minimal importance. Nevertheless, it can be useful to have in mind some picture of how current sheets might be incorporated into solar flare models, as long as such a picture is not taken as dogma.

One possible arrangement is depicted in the accompanying cartoon (Figure 1.3). In this scenario, a large current sheet is formed in the corona, perhaps through some magnetic reconnection process. It is coaligned with the top of an arcade of magnetic loops, shown as a continuous magnetic sheet, and probably includes some microturbulence leading to anomalous resistivity. Any parallel magnetic field in the current sheet itself is negligible. The local plasma, near the top of the arcade, is Joule-heated, producing the observed thermal radiation, both in hard X-rays and microwaves. Electrons are simultaneously accelerated by the electric field, and upon being pitch-angle scattered out of the current sheet, stream down the legs of the loops which comprise the arcade. These electrons will produce both additional gyrosynchrotron radiation as they stream, and thick-target hard X-rays when they impact the denser, cooler chromosphere. In addition, various plasma instabilities could generate sufficient turbulence in the flaring plasma to provide a mechanism for secondary, stochastic, particle acceleration. Finally, because of the unidirectionality of the imposed electric field, there could be a gradient, along the length of the arcade, in the energy of the scattered, streaming electrons. Some further discussion of this picture may be found in §§3.2 and 3.5.

This constitutes one of many possible scenarios incorporating current sheets into specific flare models. Another is to generate current structures along the length of an individual magnetic loop, possibly through stresses and gradients built up by relative motions of the footpoints of the loop. In this picture, many oppositely-directed currents are required, and the entire loop volume is heated. Microwaves would be generated throughout the loop volume, as would thermal hard X-ray bremsstrahlung. Thick-target bremsstrahlung would be produced by *all* (including both thermal current and runaway) electrons in the current sheets, as the current sheets inject them
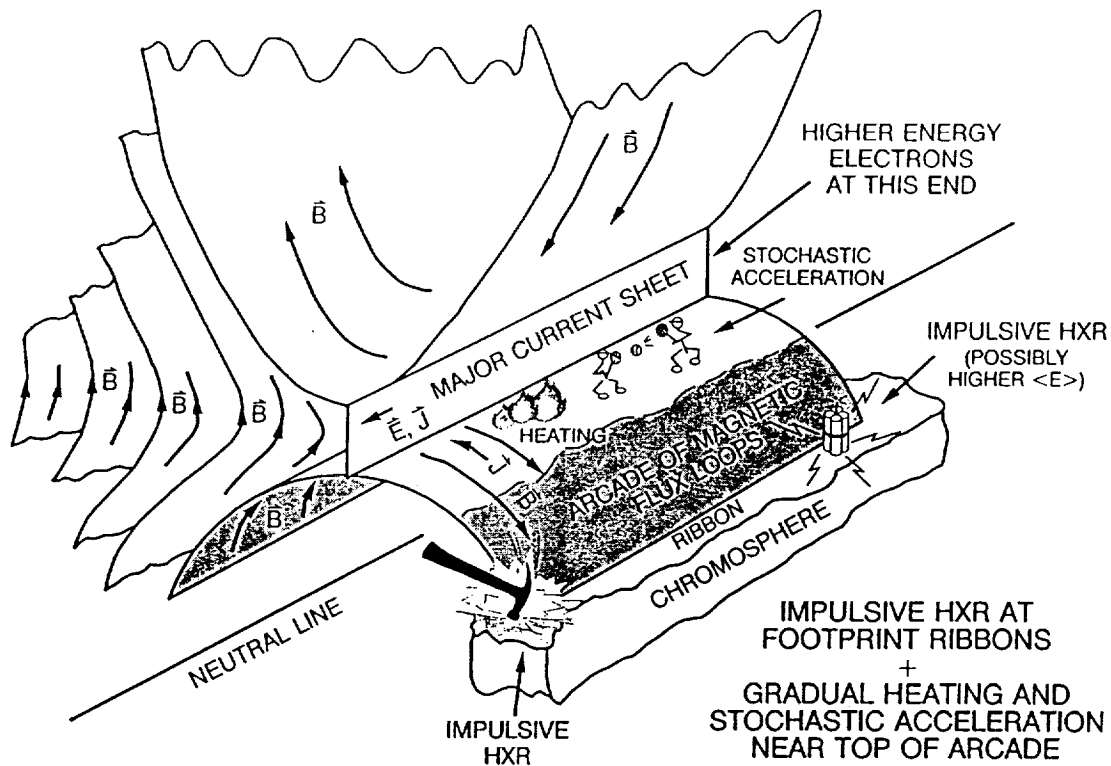
Figure 1.3: A possible solar flare scenario, incorporating current sheet heating and acceleration, as discussed in the text.

directly into the chromosphere.

The plan of this dissertation is as follows. Chapter 2 summarizes the physics of current sheets and runaway electrons. In this chapter I also present the various distribution functions to be used in later chapters, together with their derivations. This chapter represents the "meat" of the thermal/nonthermal approach. Chapter 3 is devoted to the application of the thermal/nonthermal approach to hard X-ray radiation, discussing both theoretical and observational consequences. Similarly, Chapter 4 applies the model to the microwave regime, where it is shown that some previously unexplainable phenomena can now be understood. Finally, in Chapter 5, I summarize the important results of this work, and point to a few of the many possible future applications and extensions of the ideas presented throughout this dissertation.

Chapter 2

CURRENT SHEETS, RUNAWAYS, & DISTRIBUTIONS

In this chapter I will give a brief overview of the physics of DC electric current sheets. Following this, I will discuss and present the electron distribution function for electrons within a current sheet, in both the runaway and bulk collisional regimes. I will then discuss the distribution function for electrons outside of the current sheets. Finally I will discuss limitations of these results, based on some recent, preliminary work for finite-sized current sheets.

2.1   CURRENT SHEETS & RUNAWAY ELECTRONS

The following introduction to current sheets and runaway electrons is based on Holman (1985) to which the reader is referred for further details.

The imposition of a weak external electric field $\vec{E}$ on a thermal plasma sets up a current density $\vec{J} = -eN\vec{v}_{dr} = \sigma\vec{E}$ in which the bulk thermal population, of density N, is displaced from equilibrium and moves with a drift velocity $\vec{v}_{dr}$, determined by balancing the electric field force with thermal collisions, $eE = mv_{dr}\nu_{th}$, where

$$\nu_{th} = \frac{4\pi N e^4 \ln \Lambda}{m^2 v_{th}^3} \qquad (2.1)$$

is the thermal collision frequency, and $v_{th} = \sqrt{kT/m}$ is the electron thermal velocity in a plasma of temperature T. The electrical conductivity of the plasma is $\sigma = Ne^2/m\nu_{th}$ and $\ln \Lambda = 14.7 - \ln(N^{1/2}T^{-1})$ is the Coulomb logarithm (Book 1987). The restriction that the electric field be "weak" is the restriction that $v_{dr} \ll v_{th}$, so that the plasma is not greatly displaced *en masse*.

Magnetic fields are generally ignored when discussing current sheets, and I will do the same. This is because current sheets, to be stable, must be in regions of the plasma where either $\vec{B} = 0$, or $\vec{B}\|\vec{E}$, so that $\vec{E} \times \vec{B}$ drifts are unable to disrupt them. In the latter case, the spiralling motion of the charged particles around the magnetic field line is also neglected, it being assumed that the Larmor radius is much less than the thickness of a current sheet. This is justified below (eqn [2.14]).

Every electron will experience electric field acceleration during its mean free time between collisions. The collision frequency of an electron having arbitrary velocity (of which eqn [2.1] is one case) is

$$\nu(v) = \frac{4\pi N e^4 \ln \Lambda}{m^2 v^3} .$$ (2.2)

From this we see that relatively higher energy electrons will suffer relatively fewer collisions (eqn. [2.1]), thereby experiencing relatively greater acceleration by the electric field, i.e. being pulled relatively farther out of the thermal distribution. Electrons exceeding a critical velocity, v_{cr}, at which the competing effects of collisions and the electric field just counterbalance, will be freely accelerated, unhindered by collisions. These are the runaway electrons. It is customary to express the electric field strength as a fraction of the Dreicer field

$$E_D = (m v_{th}/e)\nu_{th} = \frac{4\pi e^3}{m} \ln \Lambda \left(\frac{N}{v_{th}^2} \right)$$ (2.3)

for which a thermal electron will run away. We then have

$$v_{cr} = \sqrt{\frac{m v_{th}^3 \nu_{th}}{eE}} = \sqrt{\frac{v_{th}^3}{v_{dr}}} = \frac{v_{th}}{\sqrt{\epsilon}}$$ (2.4)

where $\epsilon \equiv E/E_D$. The restriction to a "weak" electric field is now expressed as $\epsilon \ll 1$. These expressions can be made relativistically correct by substituting $v \rightarrow p/m\gamma$ with p the electron momentum and

$$\gamma = \sqrt{(p/mc)^2 + 1}$$ (2.5)

is the Lorentz factor. We will henceforth work entirely in momentum space, in which equation (2.4) takes the form

$$\frac{p_{cr}}{mc} = \frac{(p_{th}/mc)}{\sqrt{\epsilon - (p_{th}/mc)^2(1 - \epsilon)}}$$ (2.6)

and now

$$\frac{p_{th}}{mc} = \left(\frac{mc^2}{kT} - 1 \right)^{-1/2} .$$ (2.7)

The critical momentum, p_{cr}, (or critical velocity, v_{cr}) approximately separates the electrons into two classes, the collisional (having $p < p_{cr}$), and the collisionless ($p > p_{cr}$).

Equation (2.6) implies that there are combinations of electric field strength and temperature for which no runaways will be produced, to keep the solution real. In order to generate runaways for a given temperature, T, we must have

$$\epsilon > \left(\frac{mc^2}{kT} \right)^{-1} .$$ (2.8)

For a given electric field, the restriction on T is clearly

$$T < \epsilon \frac{mc^2}{k} . \tag{2.9}$$

This relativistic restriction on runaway production was first found by Connor and Hastie (1975).

Given the electric field strength, and the length of the acceleration region, L, there exists a maximum energy gain for a runaway electron beginning with $p = p_{cr}$, and being freely accelerated for the entire length. This is

$$\Delta \mathcal{E}_{max} = \mathcal{E}_{co} - \mathcal{E}_{cr} = eEL = e\epsilon E_D L \tag{2.10}$$

where $\mathcal{E} = (\gamma - 1)mc^2$ is the kinetic energy of an electron having Lorentz factor γ. Using equations (2.5) and (2.10) we find the momentum corresponding to the high-energy cutoff,

$$p_{co}/mc = \left\{ \left[\gamma(p_{cr}) + eEL/mc^2 \right]^2 - 1 \right\}^{1/2} . \tag{2.11}$$

At the end of the acceleration region, electrons having energies in excess of $\mathcal{E}_{co}$ are expected to follow a Maxwellian distribution, having a higher temperature than that of the bulk population, since these represent bulk thermal population electrons injected at $p \sim p_{cr}$ and transported through momentum space to $p > p_{co}$.

Kinetic theory yields the following result for the relativistically accurate runaway production rate, allowing for a background of ions having average charge $\bar{Z}_i$ in units of the proton's charge (Kruskal and Bernstein 1962; Connor and Hastie 1975; Cohen 1976; Singh 1977):

$$\Gamma = (0.3 + 1.5\epsilon)\epsilon^{\frac{-3}{16}(\bar{Z}_i+1)} \exp \left[\frac{-kT}{mc^2} \left(\frac{1}{8\epsilon^2} + \frac{2}{3\epsilon^{3/2}}\sqrt{\bar{Z}_i + 1} \right) - \left(\sqrt{\frac{\bar{Z}_i + 1}{\epsilon}} + \frac{1}{4\epsilon} \right) \right] \tag{2.12}$$

For a current flowing along a finite-sized sheet of length L, width w, and thickness δr ($\delta r \ll w$), observations of magnetic field strength in the solar corona constrain the thickness as follows. The current produces an induction magnetic field, $B_J = (2\pi/c)(I/w)$, where the current $I = Jw\delta r$. The induced magnetic field can be no larger than the observed magnetic field, $B_J \le B$ which leads to

$$\delta r \le \frac{808}{\epsilon} \left(\frac{B}{100\,\mathrm{G}} \right) \left(\frac{N}{10^9\,\mathrm{cm}^{-3}} \right)^{-1} \left(\frac{T}{10^7\,\mathrm{K}} \right)^{-1/2} \mathrm{cm}. \tag{2.13}$$

Thus current sheets are very thin structures. Other possible geometries are explored in Holman (1985). Although thin, current sheets are still many Larmor radii across. The Larmor (or gyro-) radius is given by $r_L = mv_\perp c/eB$, where $v_\perp$ is the component of the particle's velocity perpendicular to the magnetic field. Taking the thermal velocity for $v_\perp$, the ratio of current sheet thickness to gyroradius is

$$\frac{\delta r}{r_L} \sim 120 \frac{B^2}{\epsilon(N/10^9)(T/10^7)} \gg 1 . \tag{2.14}$$

This justifies the neglect of spiralling motions in the treatment of runaway acceleration.

The energy dissipated by a current density $\vec{J}$ is $\vec{J} \cdot \vec{E}$ ergs cm^{-3} s^{-1}. Thus a Joule heating time scale can be defined for a current sheet by

$$\tau_J \equiv NkT/(\vec{J} \cdot \vec{E}) = \epsilon^{-2} \nu_{th}^{-1} \; . \tag{2.15}$$

In general, this is a lower limit for the plasma heating time since the total volume, V, to be heated is usually larger than the volume of the current sheet, $V_J = Lw\delta r$. Somewhat offsetting this is the fact that the plasma density outside of the sheet, N_V, is generally less than the density, N, within the sheet. Thus a more accurate estimate of the heating time scale for the flaring plasma is

$$t_J \approx \left(\frac{N_V}{N}\right)\left(\frac{V}{V_J}\right)\tau_J \; . \tag{2.16}$$

2.2 ELECTRON DISTRIBUTION FUNCTIONS IN A CURRENT SHEET

Obtaining the distribution function, f, for electrons in a plasma subjected to a weak external electric field is a formidable task. There are several factors, introduced above, contributing to the complexity of the problem. To sum up the situation, the distribution function is a drifting near-Maxwellian at the lowest momenta, becomes increasingly non-Maxwellian as we go to higher momenta, is highly non-Maxwellian throughout the runaway regime, until finally, above p_{co}, a Maxwellian again occurs.

Studies of such a distribution function have been carried out along two broad avenues. The first involves making various simplifying assumptions, and then analytically deriving approximations to the distribution function, valid in one or more regimes of momentum space. The second approach involves numerically solving the Fokker-Planck equation for the electron distribution function, and involves a different set of assumptions. To date, both approaches have assumed the plasma to be homogeneous and infinite in extent. Physical insight can be gained in both approaches by considering a test particle moving through an unchanging background plasma, as in the discussion leading to equation (2.4) above.

The first important treatment of this problem was by Spitzer and Härm (1953) who determined f numerically. Their solution is still recognized to be valid for low momenta, not much greater than p_{th}. For the weak electric fields of interest here, this is important because it includes the effect of the drift momentum, p_{dr}. An analytic form for f in this regime, including relativistic corrections, was derived by Hakim (1967; deGroot *et al.* 1980).

The work of Dreicer (1959) brought to the fore the importance of the runaway phenomenon, making necessary more sophisticated treatments than that of Spitzer and Härm. Numerous numerical studies have since been done (e.g. Kulsrud *et al.* 1973; Wiley and Hinton 1980; Wiley *et al.* 1980; Moghaddam-Taaheri *et al.* 1985; Fuchs *et al.* 1986, 1988; MacNeice *et al.* 1991). The most sophisticated analytic treatment is the unpublished work of Kruskal and Bernstein (1962; reproduced by Cohen 1976). Their basic normalized result for the runaway rate remains valid and

has been extended to include relativistic corrections (Singh 1977; Connor and Hastie 1975) (eqn [2.12] above).

All of the above-mentioned work, excepting that of MacNeice *et al.* is for an infinite plasma, and is thus of limited usefulness in applications to the sun, where finite-sized current sheets are believed to be important. Specifically, previous work has not addressed the high-energy cutoff regime of the distribution function. In the following sections I will draw on some of the above results, bringing them together in a new way, so as to be useful in the following chapters for the study of solar flares, at least in an approximate way. I will first address the distribution function of just the collisionless, high-energy, runaway electrons in a finite current sheet, then expand the discussion to include all of the current sheet electrons. Next, I will construct a simple electron distribution function for the ambient plasma in which the current sheets are embedded. In all of these derivations, I neglect any magnetic field $\vec{B}$, which means either $\vec{B} = 0$ or $\vec{B} \parallel \vec{E}$ and the electrons' spiralling is unimportant. Collective effects are also neglected. At the end of this chapter I will point out the future improvements in this analysis that will be possible when the work of MacNeice *et al.* is completed.

2.2.1   RUNAWAY ELECTRONS IN A CURRENT SHEET

Two different, but not equivalent, routes have been taken to analytically deriving the distribution function, f_{rw}, of runaway electrons in a current sheet. In the first, I consider a collection of runaways as having been accelerated from "upstream" in the current sheet, prior to which they were part of the background plasma in which the current sheet is embedded. Summing up the contributions from the entire current sheet then leads to an integral equation for f_{rw}. In the second approach, I derive a differential equation for f_{rw}, from continuity arguments, and solve it. While the former approach provides a formal solution for f_{rw}, the latter has proven to be much more fruitful and useful, as we shall see.

The runaway distributions derived here apply only to those electrons having $p > p_{cr}$, that is, we assume the particles are collisionless.

INTEGRAL EQUATION APPROACH

The Lorentz force acting on an electron for a time t imparts to it a momentum

$$p(t) = m\gamma(t)\frac{dx}{dt} = p_o + eEt \qquad (2.17)$$

$$\Delta p = p(t) - p_o = eEt \qquad (2.18)$$

where p_o is the initial momentum along the field $\vec{E} = -E\hat{x}$, m is the electron mass, and the Lorentz factor is

$$\gamma(t) = \sqrt{\left(\frac{p(t)}{mc}\right)^2 + 1}$$

$$= \sqrt{\left(\frac{p_o}{mc}\right)^2 + 1 + 2eEt\frac{p_o}{mc} + (eEt)^2} \qquad (2.19)$$

Integrating equation (2.17) yields

$$x - x_o \equiv \xi = \int_0^t \left[\frac{p_o + eEt'}{m\gamma(t')} \right] dt' , \text{ or}$$

$$\frac{eE\xi}{mc^2} = \gamma(p) - \gamma(p_o) \tag{2.20}$$

where ξ is the distance over which an electron is accelerated, and $p = p(t)$. We have used formulae 2.261 and 2.264.2 of Gradshteyn and Ryzhik (1980). Since no approximations have been made, neither Δp nor ξ need be small.

Equation (2.20) is another statement of energy conservation, as in equation (2.10) above, and is easily inverted to obtain either the initial momentum in terms of the final momentum,

$$\frac{p_o(p,x)}{mc} = \left\{ \left(\gamma(p) - \frac{eE\xi}{mc^2} \right)^2 - 1 \right\}^{1/2} \tag{2.21}$$

or vice versa, equivalent to equation (2.11) above, for a fixed acceleration distance ξ.

Consider then a current sheet of length L, subdivided into $M + 1$ elements δx_m $(0 \leq m \leq M)$, embedded in a background plasma (see Figure 2.1). The beginning of the current sheet is at $x = 0$. We are interested in obtaining the distribution function of runaway electrons $f_{rw}(x, p)$, at an arbitrary point x_m in the current sheet.

Figure 2.1: A schematic representation of a current sheet, for the derivation of equation (2.22).

The particles of a given momentum at x_m can originate from either the background plasma at x_m, or from having been accelerated up from x_{m-1}, where they had a somewhat smaller momentum, $p - \delta p$, at a somewhat earlier time, $t - \delta t$, where the notation should be obvious.

The particles at x_{m-1} can themselves have originated either from the background at x_{m-1} or from having been accelerated up from x_{m-2}, where they had a yet smaller momentum, etc.

We continue to trace the origins of the particles at x_m backward through the current sheet. At each step, we count only those particles arising from the background, since the electrons already in a given element of the sheet arose from the background at one or more prior current sheet elements. We thus continue until either (a) the beginning of the current sheet is reached, at which point there is no prior acceleration mechanism and all the plasma is background, or (b) the initial momentum, p_o, of the electrons being accelerated is decreased to p_{cr}, below which this collisionless approach fails. We then treat this point as though it were the beginning of the current sheet, with background particles having $p = p_{cr}$.

The result of all this is that the runaway electrons of a given momentum p, at the point x_m in the current sheet can be written as a sum of background contributions from "upstream":

$$f_{rw}(x_m, p) = \sum_{i=m_{min}}^{m} f_{bg}(x_m - i\delta x, p - i\delta p) .$$

The starting point of the summation depends on whether condition (a) or (b) above applies. On passing from discrete to continuous variables, we obtain an integral over acceleration distances:

$$f_{rw}(x, p)dx = \int_0^{\xi_{max}} f_{bg}(x - \xi, p_o)d\xi \qquad (2.22)$$

where $p_o(p, \xi)/mc$ is given in equation (2.21), $(x - \xi)$ represents a "retarded position" in the current sheet, f_{bg} is the electron distribution function for the background plasma in which the current sheet is embedded, and

$$\xi_{max} = \begin{cases} (mc^2/eE)[\gamma(p) - \gamma(p_{cr})] & \text{if } \gamma(p_{cr}) < \gamma(p) < \gamma(p_{cr}) + eEx/mc^2 \\ x & \text{if } \gamma(p) > \gamma(p_{cr}) + eEx/mc^2 \\ 0 & \text{otherwise} \end{cases} \qquad (2.23)$$

Given the background distribution function, we substitute $x \to (x - \xi)$ and $p \to p_o$ in $f_{bg}(x, p)$ and perform the integration indicated in equation (2.22). The upper limit of integration, ξ_{max}, represents the longest free acceleration distance available to a particle in its quest to reach the point x with momentum p.

The result (2.22) for the runaway distribution function is quite general, in the sense that it holds for any background distribution whatever, although of course some will be more physical than others. The final, complete current sheet distribution function, f_{cs}, is obtained by adding this collisionless distribution to the bulk collisional distribution in the current sheet, representing the "thermal current", to be discussed in §2.2.2. Although general, this solution is not particularly useful. For one thing, it requires a knowledge of the background distribution function which may contain nonthermal particles scattered out of the current sheet. In addition the background may have a temperature gradient along the sheet. Strictly speaking, this solution does not consider any particles pre-existing in the current sheet. Finally, this formulation does not lend itself to the treatment of losses from the current sheet.

DIFFERENTIAL EQUATION APPROACH

In this section, I derive a more useful approximate distribution function for runaway electrons in a current sheet. The derivation is one-dimensional, but losses (e.g. due to scattering out of the current sheet) are allowed for. Once again, we assume that electrons having $p > p_{cr}$ are collisionless.

The mass flowing out of an element of current sheet, dx, at position x, must equal the mass flowing in plus any sources, $\mathcal{S}$, and minus any losses, $\mathcal{L}$, within dx. Thus:

$$(p + dp)f(x + dx, p + dp) = pf(x, p) + \mathcal{S}dx - \mathcal{L}f(x, p)dx . \qquad (2.24)$$

The runaway distribution function, f_{rw}, is temporarily written as f for clarity. Rearranging, performing a Taylor expansion, keeping only 1st-order terms, and using $d/dx \equiv \partial/\partial x + (dp/dx)\partial/\partial p$, this becomes:

$$\frac{df}{dx} + \left(\frac{1}{p}\frac{dp}{dx} + \frac{\mathcal{L}}{p}\right)f = \frac{\mathcal{S}}{p} . \qquad (2.25)$$

The source term represents the mass flowing into the current sheet from the background plasma per unit time, at the position x of interest, and is thus related to f_{bg} discussed in the last section. The difference is that here, the background contributes only at the point in question. For $p \geq p_{cr}$, the background will be very underpopulated relative to particles of the same p already within the current sheet, where the electric field has pushed them up from lower momenta into a nonthermal tail. The source term thus provides only a minor contribution to the overall distribution function in the current sheet, at point x, and will be neglected. This is in contrast to the previous section, where the integrated sum of the background contributions is decidedly non-negligible. Here, we will assume that this integrated sum is absorbed in the boundary condition.

The finite length of the acceleration region means that an electron at one end having $p = p_{cr}$, will be freely accelerated to the point x, attaining the maximum cut-off momentum, $p_{co}(x)$, given by equation (2.11). The boundary condition will be that our solution match, at p_{co}, a numerical solution, from the literature, of the Fokker-Planck equation for this problem (Fuchs, *et al.* 1986; 1988). This condition is chosen because our collisionless assumption is most nearly matched by the fully collisional numerical solution at the highest attainable momenta (cf. eqn [2.2]). The numerical solution, given below, will be designated $f_{Num}(p_{co})$.

We are thus led to solve:

$$\frac{df}{dx} + \left(\frac{1}{p}\frac{dp}{dx} + \frac{\mathcal{L}}{p}\right)f = 0 , \qquad (2.26)$$

subject to $f(p_{co}) = f_{Num}(p_{co})$.

This is a linear, first-order, ordinary differential equation which has an integrating factor:

$$\text{I.F.} = \exp\left[\int_{x_o}^{x}(\frac{1}{p}\frac{dp}{dx'} + \frac{\mathcal{L}}{p})dx'\right] , \qquad (2.27)$$

where x_o is the "retarded position" in the current sheet, from which an electron having $p = p_{cr}$ would be freely accelerated to momentum p as it reaches position x. The solution is then

$$f(x,p) = (\text{I.F.})^{-1}C \tag{2.28}$$

where C is a constant of integration.

To determine C, we recognize that the numerical solution is for an infinite, homogeneous plasma, and thus does not allow for losses, so we set $\mathcal{L} = 0$ leading to I.F. $= p/p_{cr}$. Solving for f and imposing the boundary condition at $p = p_{co}$, we find $C = (p_{co}/p_{cr})f_{Num}(p_{co})$. Our solution is now:

$$f(x,p) = \frac{p_{co}(x)}{p_{cr}} f_{Num}(p_{co})(\text{I.F.})^{-1} . \tag{2.29}$$

We model the particle losses as

$$\mathcal{L} = (p/p_{th})^{\alpha}(p_{th}/\ell) \tag{2.30}$$

where ℓ is the scale length for the losses (mean free path in the current sheet) and α provides the momentum-dependence of the losses. The case of no losses ($\mathcal{L} = 0$) is obtained by letting $\ell \to \infty$ (or $\alpha \to -\infty$).

Using equation (2.20) and $dx = (mc^2/eE)d\gamma$ we get finally the distribution function for electrons undergoing runaway acceleration in a current sheet:

$$f_{rw}(x,p) = \frac{p_{co}}{p} f_{Num}(p_{co}) \exp\left[\frac{-mc^2}{eE\ell} (\frac{p_{th}}{mc})^{1-\alpha} \int_{\gamma_{cr}}^{\gamma} (\gamma'^2 - 1)^{(\alpha-1)/2} d\gamma' \right] . \tag{2.31}$$

The x-dependence is found in both p_{co} (eqn [2.11]) and in γ (and p) (eqn [2.20]). The normalization for equation (2.31) is given by (Fuchs, *et al.* 1986; 1988):

$$f_{Num}(p_{co}) \simeq \frac{\Gamma}{\epsilon}\left\{ 1 + \frac{2 + \bar{Z}_i}{\epsilon[(p_{co}/p_{th})^2 + 3T_\perp]} \right\} \tag{2.32}$$

$$T_\perp(p_{co}) = \frac{(p_{co}/p_{th})^2}{6}\left[-1 + \sqrt{1 + 12T_\infty/(p_{co}/p_{th})^2} \right] \tag{2.33}$$

$$T_\infty = \left(\frac{1 + \bar{Z}_i}{2\epsilon}\right) \ln\left(1 + \epsilon(p_{co}/p_{th})^2\right) \tag{2.34}$$

The runaway rate, Γ, was given in equation (2.12).

The solution, equation (2.31) is valid in the regime in which electrons are freely accelerated, i.e. for $p_{cr} < p < p_{co}$. For $p < p_{cr}$ we must set $f_{rw} = 0$, since collisions prevent runaway acceleration from occurring. Particles having $p > p_{co}$ are assumed to follow a Maxwellian distribution, but not necessarily having the same temperature as the plasma from which they were drawn. Equation (2.33) is a measure of the spread in the distribution function, perpendicular to the acceleration direction, in units of the original temperature. At the end of the acceleration region, for $p > p_{co}$,

we expect the parallel distribution to also be characterized by the temperature $T_\perp(p_{co})$. Thus, above p_{co}, the expression for f becomes

$$f_{co} = f_{rw} \times \exp\left[\frac{-mc^2}{kT_\perp(p_{co})}(\gamma - \gamma_{co})\right] , \qquad (2.35)$$

to give the high energy Maxwellian.

The integral in equation (2.31) can be performed analytically only for $\alpha = 0, \pm 1, \pm 2, \ldots$. The seven solutions for $-3 \leq \alpha \leq +3$ are presented below, as well as the no losses limit. Several of these are used in the accompanying figures.

Figure 2.2 displays the electron distributions used for fitting two observed hard X-ray spectra in the next chapter (Figs. 3.8 and 3.9). In both cases, the dashed line represents a Maxwellian electron distribution at the temperature of the current sheets, while the dotted line is the distribution function of runaway electrons of interest here. In the absence of detailed knowledge of the scattering processes (to fix α and ℓ), we have used the no losses solution of equation (2.36) below. The runaway regime is between $\mathcal{E}_{cr}$ and $\mathcal{E}_{co}$, the values of which are shown in the figures. This is the nearly flat ($\sim p^{-1}$) region at the 'top' of the distribution. At energies less than $\mathcal{E}_{cr}$ there are no runaways, and at energies greater than $\mathcal{E}_{co}$ there is another Maxwellian, having temperature $T_\perp(p_{co})$ given by equation (2.33). For Figure 2.2(a), $T_\perp = 3.1 \times 10^8$ K, while for Figure 2.2(b), $T_\perp = 3.5 \times 10^8$ K. The relation between the thermal and nonthermal components of these distribution functions is discussed in the next chapter.

Figures 2.3 and 2.4 show how the second of these runaway distributions changes with both α and ℓ when particle losses from the current sheets are allowed (cf. eqn [2.30]). The overall effect of particle losses is of course to reduce the population of runaways. In each figure, the dotted line is the no losses solution from Figure 2.2(b). In Figure 2.3, the scale length for losses is held constant at $\ell = 10^8$ cm and $\alpha = -3$, -2, -1, and 0 is displayed. It is apparent that for $\alpha > 0$ there would be very few runaways at all, since this means that the high energy particles are preferentially lost from the acceleration region. In Figure 2.4, we fix $\alpha = -3$ and vary ℓ, keeping it shorter than the length of the current sheet itself ($L = 3.0 \times 10^9$ cm).

SOLUTIONS TO EQUATION (2.31)

$\mathcal{L} = 0$ (no losses): This solution approximates the high energy runaway tail of the numerical solution.

$$f(\mathcal{L} = 0) = (p_{co}/p)f_{Num}(p_{co}) \qquad (2.36)$$

$\alpha = -3$: This is the momentum dependence of Coulomb collisions and, perhaps, of some anomalous resistivity processes such as ion acoustic turbulence. For Coulomb collisions, the scale length evaluated for $p = p_{cr}$ is $\ell_{Coul} = v_{cr}/\nu_{Coul} = v_{cr}^4/(v_{th}^3\nu_{th}) = (p_{cr}/\gamma_{cr})^4(\gamma_{th}/p_{th})^3(m\nu_{th})^{-1}$.
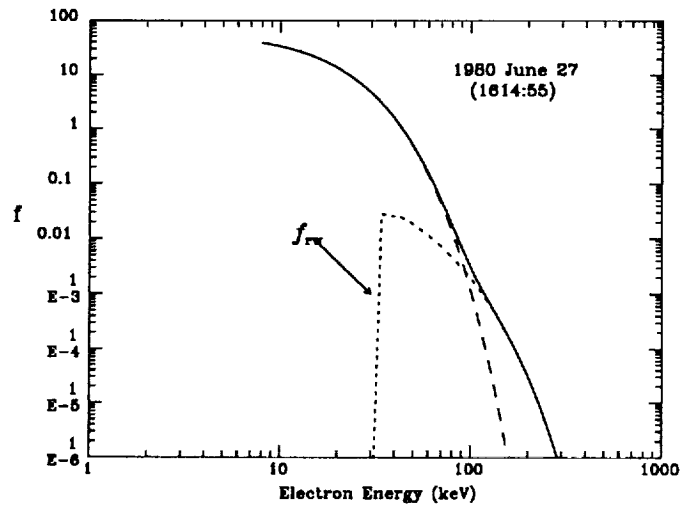
Figure 2.2(a): The electron distribution function which generates the hard X-ray spectrum of Figure 3.8. The dashed line is a Maxwellian and the dotted line is the runaway electron distribution, equation (2.36). The input parameters are $T = 9.0 \times 10^7$ K; $N = 3.44 \times 10^{10}$ cm^{-3}; $\epsilon = 0.120$; $L = 3.0 \times 10^9$ cm.
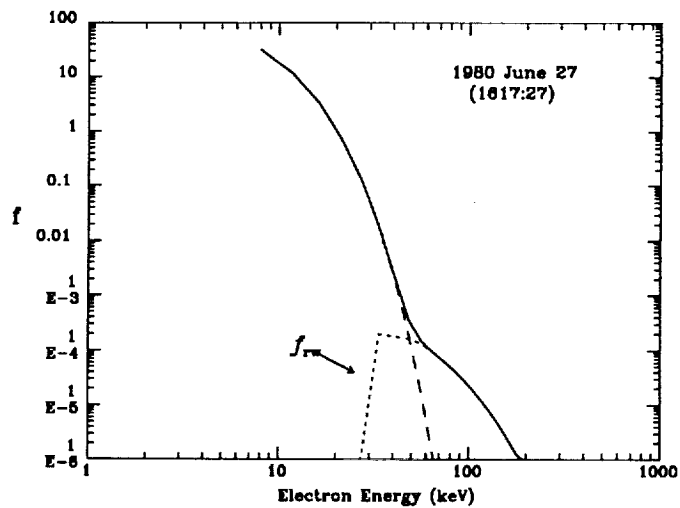
Figure 2.2(b): The electron distribution function which generates the hard X-ray spectrum of Figure 3.9. The plotting convention is as above. The input parameters are $T = 3.6 \times 10^7$ K; $N = 7.0 \times 10^{10}$ cm^{-3}; $\epsilon = 0.048$; $L = 3.0 \times 10^9$ cm.
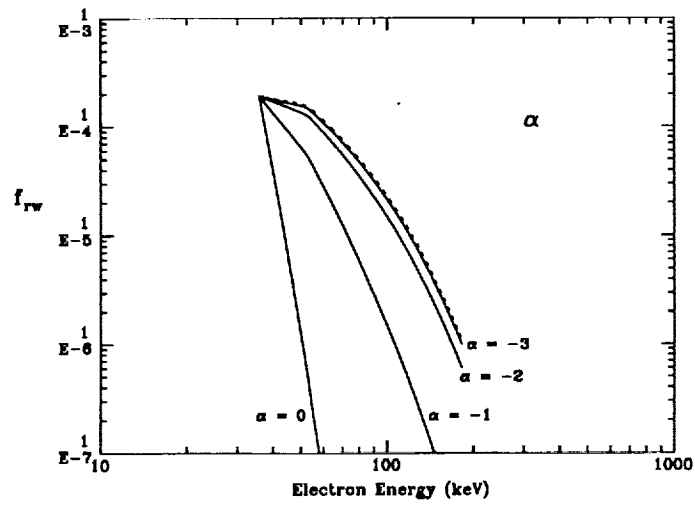
Figure 2.3: The variation with α of f_{rw} from Fig. 2.2(b) (the dotted line) as discussed in the text.
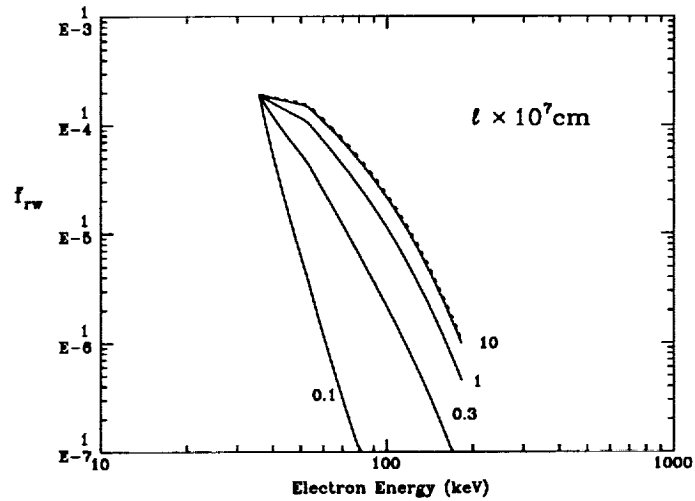
Figure 2.4: The variation of f_{rw} from Fig. 2.2(b) (the dotted line) with scale length, $10^6 < \ell < 10^8$ cm, as discussed in the text. The distributions are labelled in units of 10^7 cm.

$$f(\alpha = -3) \quad = \quad \frac{p_{co}}{p} f_{Num}(p_{co}) \left[\frac{(\gamma - 1)(\gamma_{cr} + 1)}{(\gamma + 1)(\gamma_{cr} - 1)}\right]^{(mc^2/4eE\ell)(p_{th}/mc)^4} \times$$

$$\exp\left(\frac{mc^2}{2eE\ell}(\frac{p_{th}}{mc})^4 \left[\frac{\gamma}{(p/mc)^2} - \frac{\gamma_{cr}}{(p_{cr}/mc)^2}\right]\right) \tag{2.37}$$

$\alpha = -2$:

$$f(\alpha = -2) = \frac{p_{co}}{p} f_{Num}(p_{co}) \exp\left[\frac{mc^2}{eE\ell}\left(\frac{p_{th}}{mc}\right)^3 \left(\frac{\gamma}{p/mc} - \frac{\gamma_{cr}}{p_{cr}/mc}\right)\right] \tag{2.38}$$

$\alpha = -1$:

$$f(\alpha = -1) = \frac{p_{co}}{p} f_{Num}(p_{co}) \left[\frac{(\gamma - 1)(\gamma_{cr} - 1)}{(\gamma + 1)(\gamma_{cr} + 1)}\right]^{-(mc^2/2eE\ell)(p_{th}/mc)^2} \tag{2.39}$$

$\alpha = 0$: This corresponds to particles of all energies being lost equally, e.g. during a global disruption of the current sheet.

$$f(\alpha = 0) = \frac{p_{co}}{p} f_{Num}(p_{co}) \left[\frac{\gamma + (p/mc)}{\gamma_{cr} + (p_{cr}/mc)}\right]^{-(mc^2/eE\ell)(p_{th}/mc)} \tag{2.40}$$

$\alpha = +1$: Any $\alpha > 0$ corresponds to higher energy particles being preferentially lost with respect to lower energy particles.

$$f(\alpha = +1) = \frac{p_{co}}{p} f_{Num}(p_{co}) \exp\left[\frac{-mc^2}{eE\ell}(\gamma - \gamma_{cr})\right] \tag{2.41}$$

$\alpha = +2$:

$$f(\alpha = +2) \quad = \quad \frac{p_{co}}{p} f_{Num}(p_{co}) \left[\frac{\gamma + (p/mc)}{\gamma_{cr} + (p_{cr}/mc)}\right]^{-(mc^2/2eE\ell)(mc/p_{th})}$$

$$\times \exp\left[\frac{-mc^2}{2eE\ell}\left(\gamma p/p_{th} - \gamma_{cr} p_{cr}/p_{th}\right)\right] \tag{2.42}$$

$\alpha = +3$:

$$f(\alpha = +3) = \frac{p_{co}}{p} f_{Num}(p_{co}) \exp\left(\frac{-mc^2}{eE\ell}(\frac{p_{th}}{mc})^{-2} \left[\frac{\gamma^3 - \gamma_{cr}^3}{3} - \gamma + \gamma_{cr}\right]\right) \tag{2.43}$$

2.2.2 COMPLETE ELECTRON DISTRIBUTION FUNCTION IN A CURRENT SHEET

As discussed in the introduction to this section, the collisional part of the current sheet distribution function is not easily obtained analytically. To zeroth-order, the Spitzer-Härm solution (Spitzer and Härm 1953) or its relativistic counterpart, the Hakim-deGroot distribution (Hakim 1967; deGroot *et al.* 1980) can be used. This is given by:

$$f_{HdG}(x,p) = \exp\left\{ \mathcal{N} - \gamma_{dr}\frac{mc^2}{kT}\left(\gamma(p) - \frac{p}{mc}\frac{p_{dr}}{mc} - \frac{eEx}{mc^2}\right)\right\}. \tag{2.44}$$

Here, $\mathcal{N}$ is a normalization constant, p_{dr} is the "drift momentum" of the thermal current due to the electric field, and $\gamma_{dr} = \gamma(p_{dr})$. No pitch angle effects are included here in our one-dimensional analysis of the parallel distribution. In general, $\mathcal{N}$ must be determined numerically.

In this approximation, the entire current sheet distribution function is given by

$$f_{cs} = f_{HdG} + f_{rw} ,$$

where f_{rw} is obtained from either equation (2.22) or (2.31). It is known, however, that equation (2.44) can severely underestimate the number of particles with $p > p_{th}$, and thus the important regime of $p_{th} < p < p_{cr}$ is treated quite poorly in this approximation. This regime has no satisfactory analytic treatment and yet is crucial to the runaway process. Even the sophisticated treatment of Kruskal and Bernstein (1962; Cohen 1976), in which this region of momentum space is further subdivided into three smaller regimes, generates only partial solutions in each of the three new momentum intervals, and is unable to connect them to each other. Thus it appears that at present, we cannot come up with a simple but satisfactory expression for f_{cs}.

One possible way out of this state of affairs, is to somehow parameterize the existing numerical solutions in this region of momentum space. The disadvantage of this approach is that it is largely descriptive, i.e. it is difficult to physically interpret the parameters in the resulting expression. We have nevertheless made such a parameterization, and found it to reproduce the numerically derived distribution function of Fuchs *et al.* (1988) for both $\epsilon = 0.04$ and $\epsilon = 0.1$ to within a factor of 1.5.

We achieve this parameterization as follows. We add f_{HdG} to the expressions given above for f_{rw}, but extend f_{rw} to lower than "allowable" momenta, down to p_{th}. We also multiply f_{rw} by an "enhancement factor", M, which is unity for low and high momenta and has a maximum at $p = (2/3)p_{cr}$. We use for this factor a low-order member of a δ-function sequence. Finally, to avoid a discontinuity in f at p_{th}, we "ramp up" this enhanced f_{rw} with another factor, R, which varies smoothly from zero at p_{th} to unity at p_{cr}. The complete distribution function of electrons in a current sheet is then given, in four distinct regions of momentum space, by

$$f_{cs} = \begin{cases} f_{HdG} + RMf_{rw} & \text{for } p \le p_{co} \\ f_{HdG} + Mf_{co} & \text{for } p > p_{co} \end{cases}, \tag{2.45}$$

where

$$R = \begin{cases} 0 & \text{for } p < p_{th} \\ \sin\left[(\pi/2)\frac{p-p_{th}}{p_{cr}-p_{th}}\right] & \text{if } p_{th} \le p \le p_{cr} \\ 1 & \text{if } p > p_{cr} \end{cases} \quad , \tag{2.46}$$

$$M = 1 + \frac{(p_{cr}/p_{th})\left[(p_{cr}/p_{th})-2\right]}{\pi\left\{1 + [(p/p_{th})-2/3(p_{cr}/p_{th})]^2\right\}} \ , \tag{2.47}$$

and f_{HdG} , f_{rw} , and f_{co} are given by equations (2.44), (2.31), and (2.35) respectively.

2.3 ELECTRON DISTRIBUTION OUTSIDE THE CURRENT SHEET

It is easier to obtain a believable thermal/nonthermal distribution function for the electrons in the surrounding plasma, within which the current sheets are embedded, than for the current sheets themselves. This is because, lacking an acceleration mechanism in this region, the plasma is truly thermal, albeit with some admixture of nonthermal particles arising from scattering processes within the current sheets. In addition, the temperature of the thermal plasma is constrained to be no hotter than the temperature in the current sheets, which provide the heating mechanism through Joule dissipation. Thus, outside of the current sheets we can write $f = f_{th} + f_{nt}$, where the two terms on the right represent the thermal and the nonthermal particles respectively.

There are two ways to treat the nonthermal particles in this ambient plasma, physically or descriptively. If one believes that the scattering mechanism within the current sheets is known, then the runaway electrons in the sheets can be described by equation (2.31) with the appropriate choices for α and ℓ, the momentum dependence and scale length of the losses (cf. eqn [2.30]). We then compare, at each point along the sheet, this depleted runaway distribution with that for which there are no losses at all (see Figs 2.3 and 2.4), the difference being the particles lost from the sheet, into the surrounding plasma, at each point. In other words:

$$f_{nt}(p) = \int_0^L \left[f(p,\,x\,;\mathcal{L}=0) - f(p,\,x\,;\mathcal{L}\neq 0)\right]\,\mathrm{d}x \ . \tag{2.48}$$

In this framework, the nonthermal electrons in the ambient plasma are closely coupled to the microphysics within the current sheets. Unfortunately, the various instabilities and wave turbulence spectra needed to characterize the particle scattering are not well understood at this time. Nevertheless, this procedure could be used in reverse to learn something about these microphysical processes. For instance, with simultaneous observations in hard X-rays and microwaves (see §3.2 and §4.3) we could in principle determine the values of α and ℓ which can fit both data sets, thereby characterizing the current sheet losses. Such simultaneous high-resolution spectra have not been obtained to date.

We therefore turn to a descriptive parameterization of f_{nt}, choosing the well-known power-law form

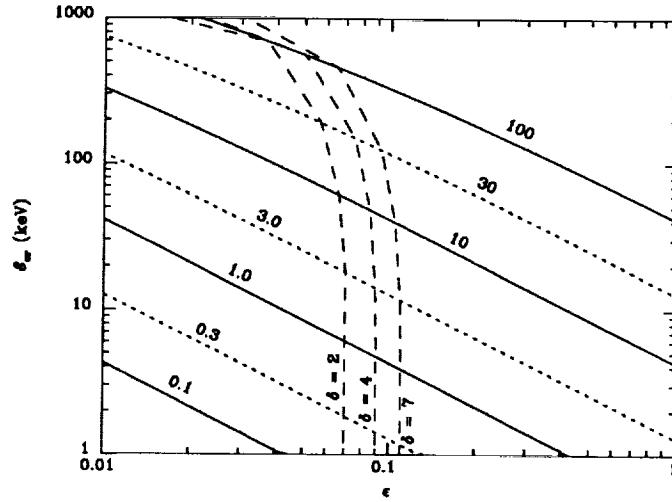$$f_{nt}(\gamma) = (4\pi)^{-1}(\delta-1)(\gamma_{cr}-1)^{\delta-1}(\gamma-1)^{-\delta} \tag{2.49}$$

Figure 2.5: $\mathcal{E}_{cr}$ vs ϵ for $10^6\,\mathrm{K} < T < 10^9\,\mathrm{K}$. The alternating solid and dotted lines are for clarity only, and are labelled in units of $10^7\,\mathrm{K}$. The long dashed lines show the suggested upper limits on ϵ for $\delta = 2$, 4, and 7 as discussed in the text.

having spectral index δ and low energy cutoff $\mathcal{E}_{cr} = (\gamma_{cr} - 1)mc^2$, with γ the Lorentz factor. The conversions between $\mathcal{E}_{cr}$ and $\epsilon \equiv E/E_D$ is shown in Figure 2.5, together with suggested maximum ϵ's, as discussed below. We restrict the spectral index to be no harder than that in the current sheets themselves. This means that $\delta \geq 1/2$, since the flattest distribution *within* the current sheets is $\propto p^{-1} \propto \mathcal{E}^{-1/2}$ for the no losses case, equation (2.36). It is seen that this is not a severe restriction. We have chosen $\mathcal{E}_{cr}$ for the low-energy cutoff for the simple reason that the nonthermal runaway electrons are overwhelmingly produced in the current sheets at this energy. Particles in the sheets having $\mathcal{E} < \mathcal{E}_{cr}$ will have predominantly a heating effect on the surrounding plasma.

For the thermal particles, we choose the first-order expansion of the Jüttner distribution, which is valid for temperatures up to $\sim 2 \times 10^9\,\mathrm{K}$. It is given by

$$f_{th}(\gamma) = \left(\frac{2}{\pi}\right)^{1/2} \left(\frac{mc^2}{kT}\right)^{3/2} \left(1 + \frac{15}{8}\frac{kT}{mc^2}\right)^{-1} \gamma(\gamma^2 - 1)^{1/2}$$

$$\times \exp\left(\frac{-mc^2}{kT}(\gamma - 1)\right) \tag{2.50}$$

Table 2.1 gives the energy, kT, associated with selected temperatures. Both equations (2.49) and (2.50) are in the form used by Dulk and Marsh (1982) and are separately normalized to unity. To join the two distributions smoothly, we let γ_{cr} set the height of the nonthermal tail, by assuming equal contributions from thermal and nonthermal particles at $\mathcal{E}_{cr}$, i.e.

$$f_{th}(\gamma_{cr}) = f_{nt}(\gamma_{cr}) . \tag{2.51}$$

For $T =$	10^7	3×10^7	5.8×10^7	10^8	3×10^8	Kelvins
$kT =$	0.862	2.59	5.00	8.62	25.9	keV

Table 2.1: Temperature/Energy Conversions

This immediately leads to an expression for the relative densities of nonthermal and thermal particles:

$$N_{nt}/N_{th} = (32\pi)^{1/2} \left(\frac{mc^2}{kT}\right)^{3/2} \left(1 + \frac{15}{8}\frac{kT}{mc^2}\right)^{-1} \frac{\gamma_{cr}(\gamma_{cr} - 1)(\gamma_{cr}^2 - 1)^{1/2}}{\delta - 1}$$

$$\times \exp\left(\frac{-mc^2}{kT}(\gamma_{cr} - 1)\right). \tag{2.52}$$

The method of joining the two distributions, equation (2.51), is not unique. For example, one can imagine separately deriving $\mathcal{E}_{cr}$ and the height of the nonthermal tail for various acceleration mechanisms. They could then be related in some fashion other than equation (2.51), or be independent of each other. It is the assumption of DC current sheet acceleration which motivates the use of equation (2.51).

The complete, normalized thermal/nonthermal distribution function in the plasma surrounding the current sheets will then be given by

$$f_{tnt}(\gamma) = (1 - \frac{N_{nt}}{N})f_{th}(\gamma) + R\frac{N_{nt}}{N}f_{nt}(\gamma) \tag{2.53}$$

using equations (2.49), (2.50), and (2.52), where $N = N_{th} + N_{nt}$ is the total electron density in the plasma, and R is again a "ramp-up" factor to avoid a discontinuity in f at p_{cr}, given by

$$R = \begin{cases} 0 & \text{if } \gamma < \gamma_R = \gamma(p_R) \text{ with} \\ & p_R = p_{cr} - p_{th}/2 \\ \sin[\frac{\pi}{2}(\gamma - \gamma_R)^2/(\gamma_{cr} - \gamma_R)^2] & \text{if } \gamma_R < \gamma < \gamma_{cr} \\ 1 & \text{if } \gamma > \gamma_{cr} \end{cases} \tag{2.54}$$

The factor R is included for completeness. Its removal has no apparent effect on the resultant spectra.

Figure 2.6 shows the distribution function, equation (2.53), used to generate the gyrosynchrotron microwave spectrum of Figure 4.12. The input parameters are $T = 7.6 \times 10^7$ K, $N_{th} = 6.0 \times 10^9$ cm^{-3}, $\delta = 4.5$, and $\epsilon = 0.077$. Notice that the discontinuity which would occur at $\mathcal{E}_{cr} = 48$ keV is largely smoothed out through the use of the ramp-up factor equation (2.54). The remaining small "hump" near $\mathcal{E}_{cr}$ has no effect on the spectrum of Figure 4.12, nor do analogous humps affect any of the other spectra in Chapter 4.

It is appropriate here to point out that for sufficiently low γ_{cr}, this particular thermal/nonthermal distribution function becomes unphysical, due to the choice of a power-law description for f_{nt}. As γ_{cr} decreases, an ever increasing fraction of the nonthermal particles are found at lower energies. For instance at $\gamma_{cr} = \gamma_{th}$,
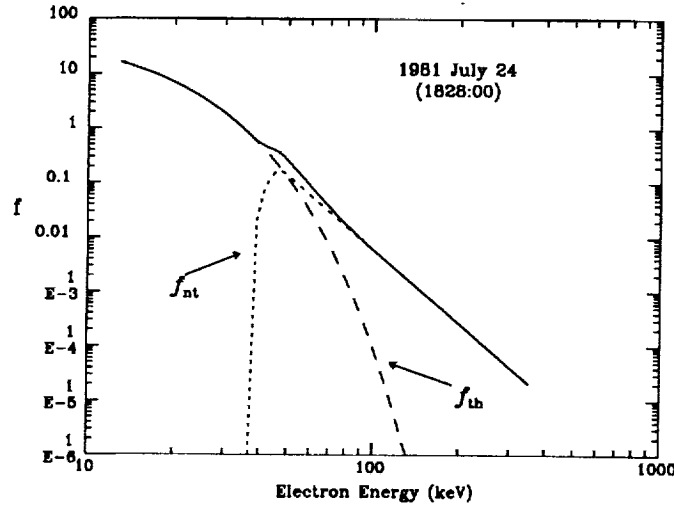
Figure 2.6: The distribution function, eqn (2.53), used to generate Figure 4.13. The input parameters are: $T = 7.6 \times 10^7 \, \text{K}$, $N_{th} = 6.0 \times 10^9 \, \text{cm}^{-3}$, $\delta = 4.5$, and $\epsilon = 0.077$.

most of the "nonthermal" particles have nearly thermal energies, and the concept of nonthermal particles loses its meaning.

The restriction that $\epsilon \ll 1$ serves to avoid this problem. We impose the (somewhat arbitrary) condition that $N_{nt} < 0.25 \, N_{th}$. Equation (2.52) then provides a maximum ϵ, for a given temperature and spectral index, to ensure that the above (arbitrary) condition is met. This ϵ_{max} is plotted as dashed lines on Figure 2.5 for $\delta = 2, 4,$ and 7. These are intended as cautionary guidelines only, and are not rigorous upper bounds on ϵ. It is seen that keeping $\epsilon \lesssim 0.1$ will keep our distribution function physical for $T \lesssim 3 \times 10^8 \, \text{K}$, except for very hard spectral indices.

I also point out that as $\gamma_{cr} \to \infty$ ($\epsilon \to 0$) equations (2.52) and (2.51) both tell us that the nonthermal contribution to f vanishes. Generally, for $\epsilon = 0.01$ or less, only the thermal population is significant.

2.4   FINITE-PLASMA EFFECTS

The thermal/nonthermal distribution function obtained in the previous section for the plasma *outside* of the current sheets (eqn [2.53]) is a useful result. Recent work by MacNeice *et al.* (1991), however, is casting some doubt on the usefulness of the distribution functions obtained so far *within* the current sheets, both earlier in this chapter and generally all previous work on the subject. The cause of the concern is that all previous work has assumed an infinite, homogeneous plasma, whereas in the real world (e.g. on the sun) either or both of the plasma, or the electric field, is finite in extent. MacNeice *et al.* show that the restriction to a finite-sized acceleration region modifies the distribution function from what has been expected.

Without going into the details of his calculations, which is a numerical Fokker-
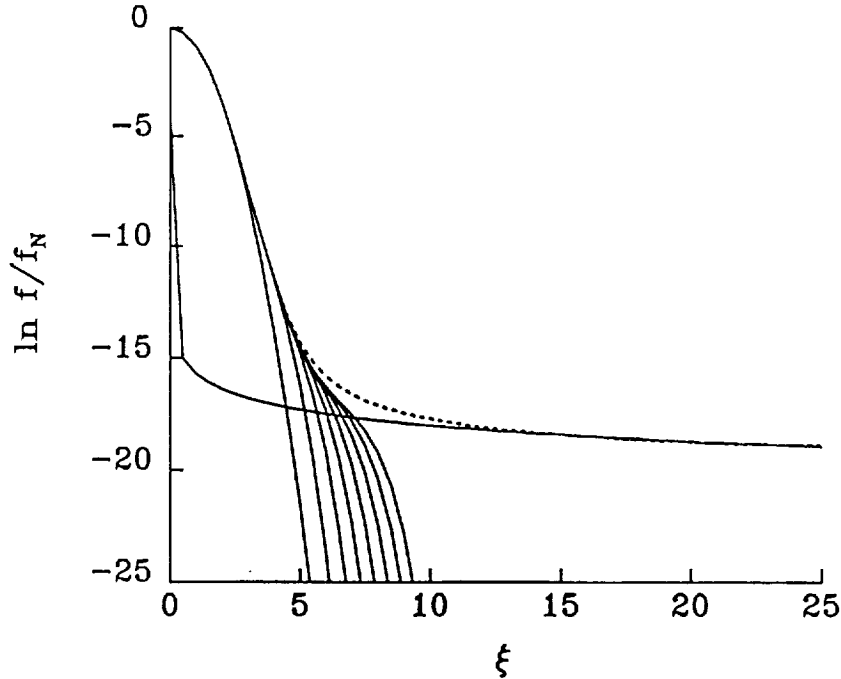
Figure 2.7: A numerically derived distribution function for a finite current sheet (MacNeice *et al.* 1991) and its comparison to eqn (2.36) as discussed in the text.

Planck solution, there are two relevant results for our purposes. First, although he finds that $f \propto p^{-1}$ in agreement with our $\mathcal{L} = 0$ solution of equation (2.31), the agreement is for very high values of p, greater than the expected p_{co}'s for solar flare-sized current sheets. Put another way, the asymptotic limit for which our solution is valid is $p_{co} \gg p_{cr}$, a regime often outside the range of applicability to solar flares. For p_{co} and p_{cr} closer together, the slope of the plateau in the electron distribution function is considerably softer than -1, and is an undetermined function of sheet length and electric field strength.

Secondly, MacNeice *et al.* find that the temperature which characterizes the high energy Maxwellian (above $\mathcal{E}_{co}$) is significantly lower than that predicted from equation (2.33). This is because $T_{\perp}(p)$ apparently does not increase indefinitely as in equation (2.33), but rather peaks at some velocity higher than v_{cr}, and subsequently decreases. When MacNeice solves the problem for the infinite homogeneous case, he finds qualitative agreement with equation (2.33).

Both of these effects can be seen in Figure 2.7 which plots $\ln f$ against his parameter $\xi \equiv v/v_{th}$, for a number of current sheet lengths. This is the sequence of plots terminating between $\xi = 5$ and 10. The dotted line is his extrapolated solution for a homogeneous, infinite current sheet, and the solid line which meets it at high ξ is just v^{-1}, normalized to his extrapolated solution. His parameters are $T = 10^6$ K, $N = 10^9$ cm^{-3}, $\epsilon = .02$, and his longest $L = 4.4 \times 10^9$ cm, although his conventions, particularly for v_{th} and E_D, differ from ours. Nevertheless, it is clear from the figure that the asymptotic agreement between his solution and that of equation (2.36) would occur at energies in excess of $\mathcal{E}_{co}$.

The results that I've just discussed are preliminary, and cannot yet be quantitatively generalized to apply to the sun. As such, in modeling hard X-rays, I will use my results from earlier in this chapter. The eventual inclusion of effects from the more accurate numerical solutions will affect, to some extent, the quantitative results of the next chapter. I nevertheless fully expect the qualitative conclusion to persist, namely that current sheets provide a viable physical framework within which to model solar flares.

Chapter 3

THERMAL/NONTHERMAL HARD X-RAYS

3.1 HARD X-RAY BREMSSTRAHLUNG

3.1.1 INTRODUCTION

When a charged particle in a plasma is accelerated in the Coulomb field of another charged particle, it emits radiation called *free-free emission* or *bremsstrahlung*. The latter term is from the German for "braking radiation". The former refers to free electrons as the accelerated particles, being free both before and after they emit their radiation. In contrast *free-bound* radiation occurs if the initially free electron is captured by the accelerating ion. *Bound-bound* radiation consists of the spectral lines formed by atomic transitions of bound electrons.

For photon energies less than $\sim 9.5\,\mathrm{keV}$, spectral lines from bound-bound transitions are of great importance in solar flare spectra. Free-bound recombination radiation may be important for the quiet corona, but for $T > 10^7\,\mathrm{K}$ free-free emission dominates (Culhane 1969). Above $\sim 400\,\mathrm{keV}$, nuclear processes begin to produce lines which contribute to the spectra. Photons having energies in the range between 10 and $\sim 400\,\mathrm{keV}$ are known as hard X-rays, and are generally agreed to be continuum radiation arising from electron-ion bremsstrahlung.

In general, any charged particle can be accelerated (scattered) by any other charged particle in a plasma. However, for particles having the same charge to mass ratio, the dipole moment $\sum e_i \mathbf{r}_i = (e/m) \sum m_i \mathbf{r}_i$ is a constant of the motion. This means that electron-electron or proton-proton interactions will not produce radiation in the dipole approximation, since the radiation is determined by the second time derivative of the dipole moment. We are thus led to consider electron-proton (electron-ion) collisions, with the electron emitting the radiation since its much smaller mass means it will undergo much greater acceleration.

The relation of the radiating electrons to their environment is also important. If the radiating electron population is not significantly affected by collisions, we say that the bremsstrahlung is produced in a *thin-target*. Conversely, if an electron population is injected into a region where collisions will significantly alter its distribution function, and emits the radiation in this region, we say that the bremsstrahlung is produced in a *thick-target*. Such a target is generally both cooler and denser than

the particles injected into it. Hard X-ray bremsstrahlung produced by a thermal population of electrons is, by definition, thin-target bremsstrahlung. Nonthermal thin-target bremsstrahlung is probably not seen from solar flares (see §3.2 below), except possibly with imaging instruments. Thin-target and thick-target emission refer to the effect of the environment on the radiating electrons. This should not be confused with optically-thin or optically-thick radiation, which refers to the effect of the environment on the *photons*. All of the hard X-rays that we observe from solar flares are optically thin, which simply means that the emitted photons are unmodified on their way out of the solar atmosphere.

I will now briefly review the radiation formulae for both thermal bremsstrahlung and nonthermal thick-target bremsstrahlung, the latter for a general electron distribution function. I will then discuss the role of current sheets in producing this radiation (§3.2), calculate theoretical spectra (§3.3), fit and discuss some high resolution solar flare hard X-ray data (§3.4), and show how these ideas can be used to model hard X-ray images of two-ribbon flares (§3.5).

3.1.2 THERMAL BREMSSTRAHLUNG

The bremsstrahlung emissivity from a Maxwellian plasma is (Tucker 1975):

$$
\begin{aligned}
j(\nu) &= \left(\frac{64\pi}{3^{3/2}}\right) N_e \sum_i (N_i Z_i^2) \left(\frac{e^2 r_o^2 c}{\bar{v}_{th}}\right) \bar{g}_{ff} e^{-h\nu/kT} \\
&= 6.8 \times 10^{-38} N_e \sum_i (N_i Z_i^2) T^{-1/2} \bar{g}_{ff} e^{-h\nu/kT} \quad \text{erg cm}^{-3}\ \text{s}^{-1}\ \text{Hz}^{-1} \quad (3.1)
\end{aligned}
$$

where r_o is the classical electron radius, $\bar{v}_{th} = \sqrt{(2kT/\pi m_e)}$, and $\bar{g}_{ff}$ is the temperature averaged Gaunt factor.

Multiplying this expression by the volume, V, of the emitting region, dividing by $4\pi R^2 \varepsilon$ with $R = 1\,\text{AU} = 1.5 \times 10^{13}\,\text{cm}$ and ε the photon energy, and converting ergs, Hz, and Kelvins to keV, we obtain the differential thermal bremmstrahlung X-ray flux (Crannell *et al.* 1978):

$$
I(\varepsilon) = 1.07 \times 10^3 \frac{\sum_i \text{EM}_i Z_i^2}{\varepsilon \sqrt{kT}} \bar{g}_{ff} e^{-\varepsilon/kT} \quad \text{photons cm}^{-2}\ \text{s}^{-1}\ \text{keV}^{-1}. \quad (3.2)
$$

The emission measure, $\text{EM}_i = N_e N_i V \times 10^{-45}$, with N_i the density of ions having charge number Z_i, and N_e the electron density. Using coronal elemental abundances (Meyer 1985), the average charge state of the fully ionized flare plasma is $\bar{Z}_i = 1.2$. Combined with charge neutrality ($N_e = \sum_i N_i Z_i$), we obtain $\sum_i \text{EM}_i Z_i^2 = 1.2\text{EM}$, with $\text{EM} = N_e^2 V$. The Gaunt factor is approximately (Tucker 1975) $\bar{g}_{ff} = (T/\varepsilon)^{0.4}$. Making these substitutions, equation (3.2) becomes

$$
I(\varepsilon) = \frac{1.3 \times 10^6 \text{EM}}{\varepsilon^{1.4}(kT)^{0.1}} \exp\left(-\frac{\varepsilon}{kT}\right) \quad (3.3)
$$

This expression is used below to calculate thermal hard X-ray bremsstrahlung.

3.1.3   THICK-TARGET BREMSSTRAHLUNG

An electron of kinetic energy $\mathcal{E}$ can generate bremsstrahlung photons of all energies $\varepsilon \leq \mathcal{E}$. The differential thick-target bremsstrahlung hard X-ray flux is given by (Brown 1971):

$$
\begin{aligned}
I(\varepsilon) &= \left(\frac{r_o}{1\mathrm{AU}}\right)^2 \frac{1}{137} \frac{mc^2}{3\pi^2 e^4 \ln\Lambda} \frac{N_r A}{\varepsilon p_{th}} \int_{\mathcal{E}_{min}}^{\mathcal{E}_{max}} f(\mathcal{E};\alpha,\ell) \int_{\mathcal{E}_{min}}^{\mathcal{E}} \sigma_{BH}(\varepsilon,\mathcal{E}')\mathrm{d}\mathcal{E}' \, \mathrm{d}\mathcal{E} \\
&= 1.345 \times 10^{-24} \frac{N_r A}{\varepsilon p_{th} \ln\Lambda} \int_{\mathcal{E}_{min}}^{\mathcal{E}_{max}} f(\mathcal{E};\alpha,\ell) \\
&\quad \times \int_{\mathcal{E}_{min}}^{\mathcal{E}} \bar{Z}_i^2 \ln \left[\frac{1 + \sqrt{(1 - \frac{\varepsilon}{\mathcal{E}'})(1 - \frac{\varepsilon}{\mathcal{E}' + 2mc^2})}}{1 - \sqrt{(1 - \frac{\varepsilon}{\mathcal{E}'})(1 - \frac{\varepsilon}{\mathcal{E}' + 2mc^2})}} \right] \mathrm{d}\mathcal{E}' \, \mathrm{d}\mathcal{E} \qquad (3.4)
\end{aligned}
$$

In these expressions, $f(\mathcal{E};\alpha,\ell)$ is the electron energy distribution function for the electrons which reach the thick-target. These can be either the entire current sheet population, or the runaways alone. Particle losses from the current sheet are parameterized by α and ℓ (eqn [2.30]). The direction-integrated Bethe-Heitler cross section for bremsstrahlung (Koch and Motz 1959, their eqn [3BNa]) is $\sigma_{BH}(\varepsilon, E)$ for photon energy ε and electron energy $\mathcal{E}$, and is valid in the form used here for ε up to ~ 400 keV. The density N_r refers to the radiating electrons, not to the target, and A is the effective surface area of the emission. The coronal charge number is again $\bar{Z}_i = 1.2$. The integration is over electron energy. The lower limit of integration is the greater of either ε or $\mathcal{E}_{cr}$ if only runaway electrons are impinging on the chromosphere (the thick-target). If the entire current sheet distribution (runaways + thermal current) is used, the lower limit is always ε, the photon energy.

Equation (3.4) is used below to generate thick-target hard X-ray spectra. The spectra tend to flatten for photon energies $\varepsilon < \mathcal{E}_{min}$.

Also of interest in thick-target modeling are the rates at which nonthermal electrons, and the energy they carry, are injected into the target. Both rates are calculated for energies above some low-energy cutoff, $\mathcal{E}_o$, which is $\mathcal{E}_{cr}$ for the present runaway electron model. These rates are given respectively by

$$
F(\mathcal{E}_o) = \int_{\mathcal{E}_o}^{\infty} f(\mathcal{E})\mathrm{d}\mathcal{E} \quad \text{electrons sec}^{-1}, \text{ and} \qquad (3.5)
$$

$$
1.6 \times 10^{-9} \mathcal{F}(\mathcal{E}_o) = \int_{\mathcal{E}_o}^{\infty} \mathcal{E} f(\mathcal{E})\mathrm{d}\mathcal{E} \quad \text{ergs sec}^{-1}. \qquad (3.6)
$$

3.2   CURRENT SHEETS AND HARD X-RAYS

The assumption that current sheets exist in a solar flare plasma provides a natural mechanism for generating the hard X-rays that are observed. The currents successfully heat the plasma surrounding them via Joule dissipation, and accelerate particles nonthermally via the runaway process. The heated plasma will then produce thermal bremsstrahlung while the nonthermal particles produce thick-target bremsstrahlung when they impinge on the chromosphere.

The nonthermal particles will also produce thin-target bremsstrahlung higher in the corona. The low flux of these particles relative to the thermal population in

this region (eqn [2.12]), means that the thin-target radiation will be unobservable in this model, except at high enough photon energies such that the thermal emission is negligible. However, at these high energies, the thick-target emission will dominate, being two powers of energy harder than the thin-target emission while produced by essentially the same population of electrons (Brown 1971; Tandberg-Hanssen and Emslie 1988). In addition, it has been shown by Gary (1985) that thin-target emission cannot be easily reconciled with microwave observations. We thus neglect nonthermal thin-target emission in this model.

There are at least two distinct scenarios, incorporating current sheets, for producing the hard X-rays. In one (Fig 1.3), a large single current sheet is located along the top of an arcade of magnetic loops in the corona. This could be produced, for example, through a coronal magnetic reconnection process. The runaway electrons cannot be accelerated along the entire length of the current sheet, since then the runaway current would generate an induced magnetic field far in excess of that observed (see discussion leading to eqn [2.13]). The runaways thus must be scattered out of the current sheet on a length scale much less than the length of the sheet itself, whereupon they will subsequently stream down the legs of the magnetic arcade and generate thick-target emission as they enter the denser regions of the solar atmosphere. The thermal current atop the arcade serves to heat the surrounding coronal plasma, from which we then observe thermal hard X-ray bremsstrahlung. When the emission measure of this thermal radiation becomes large enough, it is observed as the superhot component of flare hard X-ray spectra (Lin, *et al.* 1981). This scenario has been used to model high resolution hard X-ray spectra from a solar flare (§3.4 below). Since the thermal and nonthermal hard X-rays come from spatially distinct regions of the solar atmosphere in this scenario, it is possible to produce simple model images of two-ribbon flares (§3.5).

It was shown by Holman (1985; Holman *et al.* 1989) that anomalous resistivity is required in this scenario, if the hard X-ray emission is either purely thermal or purely nonthermal. This requirement may or may not still hold in this hybrid approach. Self-consistent modeling of simultaneous observations in hard X-rays, soft X-rays, and microwaves is needed to resolve the issue. Since the resistivity $\eta = 1/\sigma = m\nu/Ne^2$, anomalous resistivity may be incorporated by rescaling equation (2.1), if the wave turbulence scattering still has a v^{-3}-dependence. This is the case for ion acoustic turbulence. In the remainder of this chapter, classical resistivity is assumed.

The second possibility is that many ($> 10^4$) oppositely-directed current sheets exist within the flare plasma (Holman 1985). In this case we can imagine that the currents are coaligned with, and residing in, one or more magnetic loops, and thus terminate in the chromosphere. They must be oppositely directed so as to limit the *net* current, and hence the induced magnetic field. A loop may be envisioned as a cross-sectional portion of the arcade in Figure 1.3. Now the thermal current, as well as the runaways, will generate thick-target bremsstrahlung, while thermal bremsstrahlung is produced throughout the loop volume. In this picture, the entire current sheet distribution function is used for the thick-target calculation, and thus the superhot component of hard X-ray spectra can be produced by either or both of thermal and thick-target bremsstrahlung. As discussed at length in the last chapter, however, there is no entirely satisfactory expression that can be used for

f_{cs}. In addition, the current-filamentation process is not well understood. We will thus concentrate for the remainder of this chapter on the first picture, in which only the runaway electrons enter the thick-target, recognizing, however, that other possibilities exist.

It is important to bear in mind that the plasma parameters, such as temperature and density, can in general be very different in current sheets compared to the surrounding plasma. Current sheets are certainly hotter and probably more dense (Syrovatskii 1981). This has two important consequences for the the thermal emission. First, we expect to see thermal emission from the hottest regions of the flare, which means from that plasma directly heated by the current sheets to nearly the temperature of the sheets themselves. The sheets however are very thin structures (eqn [2.13]) and so their total volume can be quite small. Thus, although thermal bremsstrahlung is present, it will not necessarily be observed as a distinct thermal component until enough of the surrounding plasma is heated and thus increases the emission measure (volume) of the thermal bremsstrahlung emitting plasma. The rate at which this occurs depends in turn on the heat transport properties of the plasma. The fact that the density is likely to be different in the two regions means that the current sheet density cannot be used to determine the thermal emission measure, and *vice versa*. Current sheet density and thermal emission measure are thus independent quantities in this model.

3.3 THEORETICAL HARD X-RAY SPECTRA

3.3.1 INTRODUCTION

In this section I present theoretical spectra incorporating both nonthermal thick-target bremsstrahlung (eqn. [3.4]) and thermal bremsstrahlung (eqn. [3.3]). For the former process, in the absence of detailed knowledge of turbulence and instabilities in the current sheets, I will use the runaway electron distribution function with no current sheet losses (eqn. [2.36]). An examination of the various f_{rw} with losses in the last chapter shows that, in general, including losses will soften the runaway distribution function, and thus soften the nonthermal portion of the hard X-ray spectra as well.

With no losses, then, we have at our disposal six parameters to calculate a hard X-ray spectrum: Temperature T, and Emission Measure EM, which characterize the thermal bremsstrahlung; Electric field strength ϵ, Density N, and Length L, which characterize the current sheets; and Area A, which characterizes the thick-target source. Of these, EM and A are premultipliers, of the thermal and nonthermal components of the spectrum respectively. As such, these parameters serve only to raise or lower their respective parts of the spectrum *in toto*, not altering their respective shapes. The shape of the overall spectrum can nevertheless change, if the premultipliers are not altered in unison, as in Figures 3.3 and 3.7 below.

Although the length of the current sheet enters only in a product with the current sheet density, NL (eqn [2.11]), while the area enters only in a similar product, NA, we cannot eliminate one parameter. This is because we require both the absolute electric field strength (to determine p_{co}, which also requires L), and the ratio $\epsilon \equiv E/E_D$ (to determine p_{cr}). Thus if we eliminate N as an input parameter
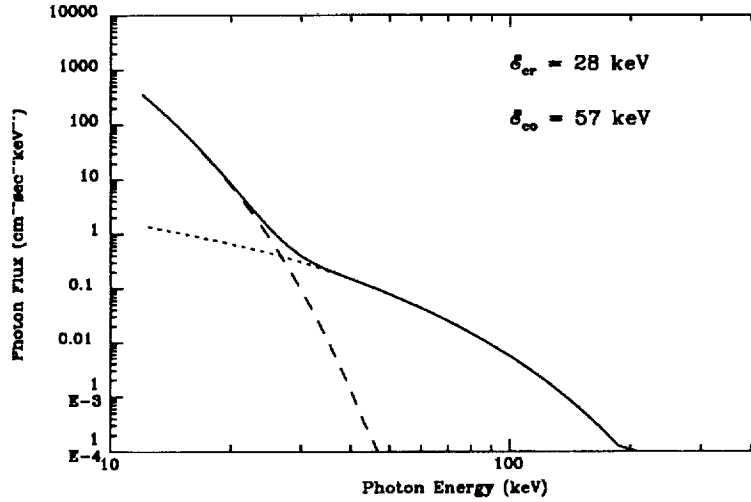
Figure 3.1: The basic hard X-ray spectrum which is varied in Figures 3.2 – 3.7. The input parameters are: $T = 3 \times 10^7$ K; EM $= 10^{48}$ cm^{-3}; $N = 10^{11}$ cm^{-3}; $\epsilon = 0.050$; $L = 3 \times 10^9$ cm; $A = 10^{15}$ cm^2. The dashed (dotted) line is thermal (thick-target) bremsstrahlung.

in favor of the above two products, we then need to specify either E, or E_D, in addition to ϵ.

The temperature is the only parameter to play a role in both parts of the spectrum, since it helps to determine the Dreicer field (eqn [2.3]) for which ϵ is a scaling factor, as well as being the temperature to which the ambient plasma is being heated. It is this coupling of the thermal and nonthermal emissions, through the common temperature, which helps constrain the full set of parameters.

It is appropriate here to mention the conventional modeling of high resolution hard X-ray spectra (Lin *et al.* 1981; Lin and Schwartz 1987). These authors also use a thermal/nonthermal approach, in which the nonthermal radiation is characterized as a double power-law. They then also employ six parameters: Temperature, Emission Measure, two break energies, and two power-law indices. They have demonstrated that six parameters are justified, by applying the F-test to the χ_ν^2-statistic (Bevington 1969). The advantage of the current approach is that the parameters are all easily interpreted physical quantities, thus enabling us to gain real insight into the physics underlying the solar flare phenomenon. In addition, because the parameters are physically coupled, only *five* of the six parameters are actually required to fit the data (see §3.4 below).

In the sections which follow, I will show and discuss how a basic theoretical spectrum changes with each of the six parameters. The basic spectrum is shown in Figure 3.1 with the thermal and nonthermal thick-target contributions shown as dashed and dotted lines respectively. This spectrum is also shown as a dot-dashed line on Figures 3.2 through 3.7, and has the following input parameters: $T = 3 \times 10^7$ K; EM $= 10^{48}$ cm^{-3}; $N = 10^{11}$ cm^{-3}; $\epsilon = 0.050$; $L = 3 \times 10^9$ cm;

$A = 10^{15}\,\mathrm{cm}^2$. The values of these parameters were chosen so that the resulting spectrum clearly shows both the superhot thermal and the nonthermal components. In §3.4 below, I will show that comparable values for the parameters can be deduced for observed spectra. For each parameter that is varied, we fix the other five. In addition, for T, N, ϵ, and L we allow both EM and A to adjust so as to fix two points in the spectrum, one in each of the thermal and nonthermal regimes. The two points, taken from the basic spectrum of Figure 3.1, are $I(13\,\mathrm{keV}) = 215$ photons $\mathrm{cm}^{-2}\,\mathrm{sec}^{-1}\,\mathrm{keV}^{-1}$ and $I(150\,\mathrm{keV}) = 5.9 \times 10^{-4}$ photons $\mathrm{cm}^{-2}\,\mathrm{sec}^{-1}\,\mathrm{keV}^{-1}$. This can help give a "feel" for how these four parameters can be used to fit an observed spectrum.

3.3.2 VARIATIONS WITH HARD X-RAY PARAMETERS

TEMPERATURE

In Figure 3.2(a) it is seen that increasing the temperature of the current sheets (and hence of the surrounding plasma) has a dramatic effect on the hard X-ray spectrum. The superhot thermal component becomes increasingly dominant over an ever increasing range of photon energies, beginning at the lower energies. In addition, the nonthermal emission is reduced as T increases, further enhancing the thermal aspect of the resultant spectrum. The reduction in nonthermal emission has two causes, which are related. First, as T goes up so does $\mathcal{E}_{cr}$ which means that only the highest energy electrons undergo runaway acceleration. Secondly, the absolute value of the Dreicer field decreases because of its T^{-1}-dependence (eqn [2.3]), so that, since ϵ is fixed, the electrons are less efficiently accelerated. Recall that we are assuming classical resistivity throughout this chapter. The opposite effects ensue when the temperature is decreased, until for $T = 10^7\,\mathrm{K}$ (the dotted line in Figure 3.2(a)), the thermal emission is unobservable, while the nonthermal emission is an order of magnitude greater than in the basic spectrum.

In Figure 3.2(b), we constrain the emission at 13 keV to be thermal with a fixed flux of 215 photons $\mathrm{cm}^{-2}\,\mathrm{sec}^{-1}\,\mathrm{keV}^{-1}$, and the emission at 150 keV to be thick-target with a flux of 5.9×10^{-4} photons $\mathrm{cm}^{-2}\,\mathrm{sec}^{-1}\,\mathrm{keV}^{-1}$. To achieve this, we allow the thermal emission measure and the thick-target area to vary freely, until both conditions are met. This is a very useful technique for fitting spectra with well-observed thermal components at low energies. The shape of this component is determined exclusively by the value of T, as shown in Figure 3.2(b). Thus the temperature and emission measure can be determined with high precision.

The dotted line in Figure 3.2(b) corresponds to that in Figure 3.2(a), with the emission measure of the former multiplied by $\sim 2 \times 10^4$ while A is decreased by a factor of $\sim .3$ to meet the constraints. The spectrum for $T = 2 \times 10^8\,\mathrm{K}$ has a dominant thermal component at the "nonthermal" constraint point, rendering this constraint meaningless. In fact, at this high a temperature, we are within the old "thermal model" regime, in which nonthermal emission is largely unobservable.
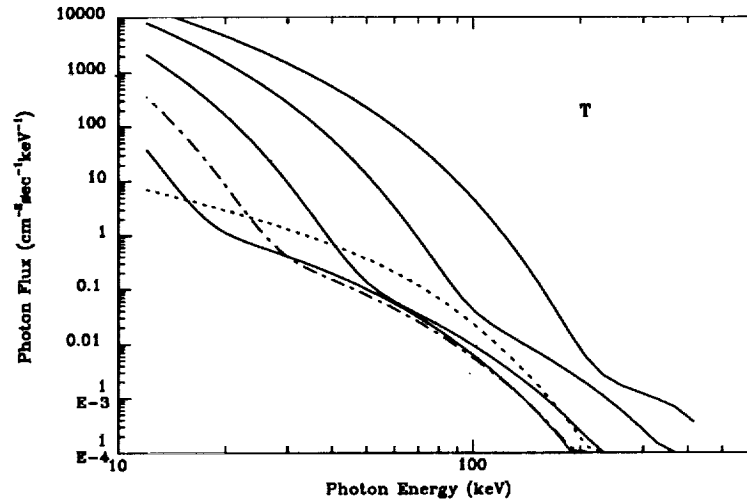
Figure 3.2(a): The temperature variation of the basic spectrum of Figure 3.1 (dot-dashed line). From bottom to top at 12 keV, $T = 10^7$ (dotted), 2×10^7, 3×10^7 (basic), 5×10^7, 10^8, and 2×10^8 K.

Figure 3.2(b): The same as Figure 3.2(a), except the spectra are constrained to pass through $I(13 \text{ keV}) = 215$, and $I(150) = 5.9 \times 10^{-4}$, as discussed in the text. The spectra are ordered, at 20 keV, the same as above. For $T = 2 \times 10^8$ K, the nonthermal constraint cannot be met, as discussed in the text.

EMISSION MEASURE

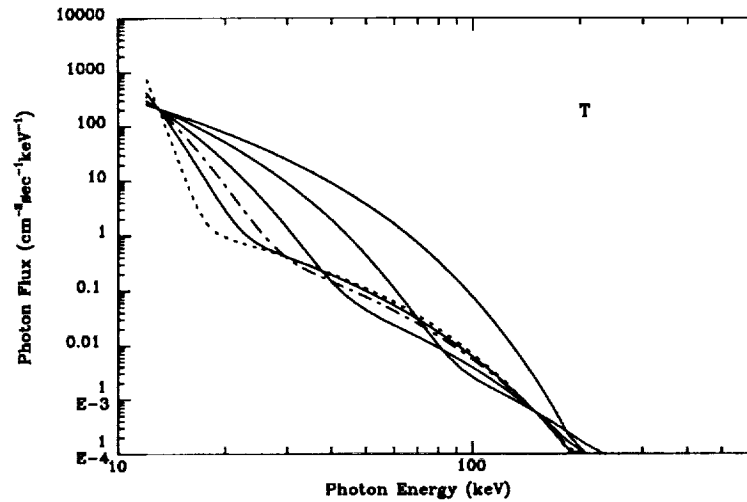Varying the emission measure of the thermal bremsstrahlung merely raises or lowers the thermal portion of the spectrum *in toto*, leaving the nonthermal tail unaffected, as seen in Figure 3.3. For a spectrum with a well-observed thermal component, this parameter can be determined very precisely, as discussed above.
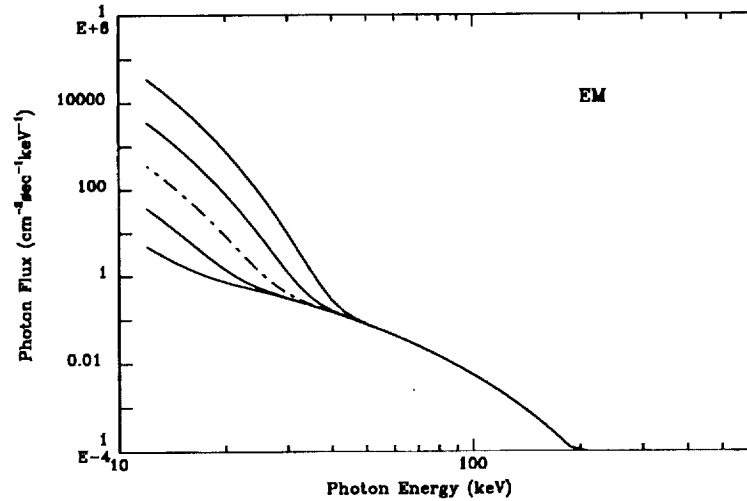

Figure 3.3: The variation of the basic spectrum with emission measure. From bottom to top, EM $= 10^{46}$, 10^{47}, 10^{48} (basic), 10^{49}, and 10^{50} cm^{-3}. Only the thermal component is affected.

ELECTRIC FIELD RATIO

Increasing the electric field strength through $\epsilon \equiv E/E_D$ increases the nonthermal character of the hard X-ray spectrum as expected, while leaving the thermal emission unchanged (Figure 3.4(a)). Recall from Chapter 2 that we are restricted to $\epsilon \ll 1$, but $\epsilon = 0.15$ is probably not excessive here, where only the runaway electrons are considered. If the "thermal" electrons within the current sheets were important for thick-target emission, the expression for their distribution function could not be trusted for $\epsilon = 0.15$, since $v_{dr} \not\ll v_{th}$. As it is, the thermal bremsstrahlung is very apparent in Figure 3.4(a) for low ϵ, significantly modified for $\epsilon = 0.07$, and overwhelmed by nonthermal emission for $\epsilon > 0.10$.

The energy gained by a runaway electron in a current sheet increases with ϵ (eqn [2.10]) for fixed acceleration distance and Dreicer field. However, although $\mathcal{E}_{cr}$ decreases monotonically with increasing ϵ, $\mathcal{E}_{co}$ does not monotonically increase. This is due to the nonlinear dependence on ϵ of equation (2.11). For instance, in Figure 3.4(a) we have for $\epsilon = 0.02$, $\mathcal{E}_{co} = 92$ keV (with $\Delta\mathcal{E} = 12$ keV) while for $\epsilon = 0.05$, $\mathcal{E}_{co} = 57$ keV (although $\Delta\mathcal{E} = 29$ keV). All of this means that the slope
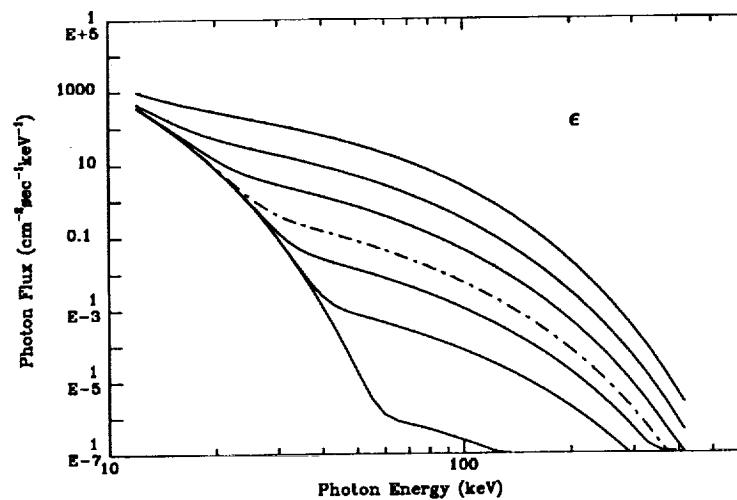
Figure 3.4(a): The ϵ variation of the basic spectrum. From bottom to top at 100 keV, ϵ = .02, .03, .04, .05 (basic), .07, .10, and .15.
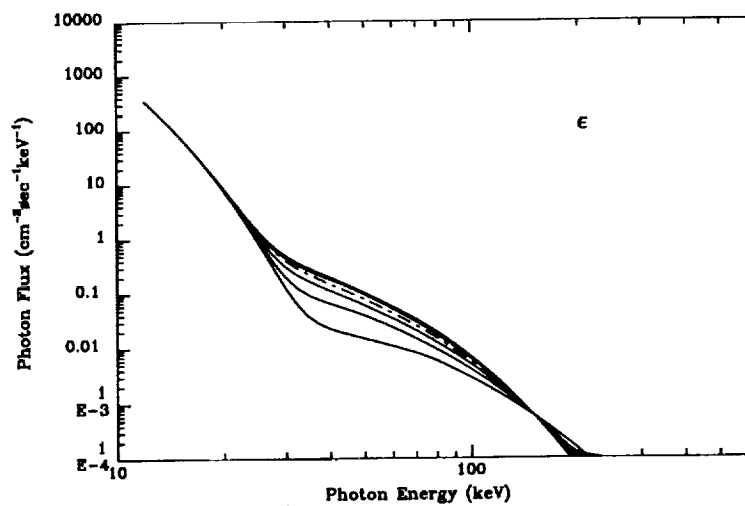

Figure 3.4(b): The same as Figure 3.4(a), except constrained as in Figure 3.2(b). The spectra are ordered, at 40 keV, as above.

of the thick-target spectrum does not necessarily change systematically with ϵ. In fact, however, when we constrain the spectra in order to fit observations (Figure 3.4(b)), we find that the spectrum changes only slightly for all but the lowest ϵ. To account for these, recall from §3.1.3 that for $\varepsilon < \mathcal{E}_{cr}$, the hard X-ray spectrum flattens out. Thus at the lowest ϵ (highest $\mathcal{E}_{cr}$), the constrained spectra of Figure 3.4(b) are flatter than, and hence lie below, those of higher ϵ.

I will argue in the next chapter that ϵ is a prime candidate for characterizing the gross evolution of a flare.

CURRENT SHEET DENSITY

At the outset of the density variation discussion, it bears repeating that the density which premultiplies equation (3.4) is that of the *radiating* particles, i.e. the runaway electrons which escape the current sheet to stream down to the chromosphere. In Figures 3.5(a) and 3.5(b) we are varying the *total* density of electrons in the current sheet. Of course increasing the total density will also increase the numbers of runaways, all other things being equal. This is seen at the lower densities in Figure 3.5(a), where a factor of 10 change in density produces a corresponding change in thick-target emission. But all things are not equal. The factor of N in equation (2.3) means that the electric field strength also changes. This means that the density of runaways increases not merely because the thermal density does, but also because the electric field accelerates more nonthermal electrons out of the thermal distribution. This enhancement of nonthermal particles is seen to have a dramatic effect at the higher densities, i.e. stronger electric fields.

Figure 3.5(b) shows the same spectra, but constrained as in Figure 3.2(b) for data fitting. It is seen that, once the thermal part of the spectrum has been determined, the nonthermal part changes with density in two ways. First, the nonthermal slope becomes flatter with increasing density, since the electric field strength increases, hardening the electron distribution. Secondly, although $\mathcal{E}_{cr}$ is unchanged with density (28 keV for these spectra), the energy of departure from thermal bremsstrahlung increases with density. This results from the steeper sloped spectra (lower densities) requiring a larger area of emission to pass through the nonthermal constraint point at 150 keV. For $N = 10^{10}\,\mathrm{cm}^{-3}$, we have that $\mathcal{E}_{co} = 31\,\mathrm{keV}$ which is only 3 keV above $\mathcal{E}_{cr}$. Thus at still lower densities the shape of the spectrum will change very little ($\mathcal{E}_{co} \to \mathcal{E}_{cr}$ as $N \to 0$; eqns [2.10] and [2.3]) since the energy gain in the sheets is approaching 0 and the normalization is constrained. The result is essentially a bithermal distribution, with temperatures T and $T_\perp$. On the other hand, as N gets large so does $\vec{E}$, causing $\mathcal{E}_{co}$ to increase. Thus the slope asymptotically flattens, but since it is constrained to pass through a data point (at 150 keV), the change due to N is bounded for large as well as small N in Figure 3.5(b).

CURRENT SHEET LENGTH

A comparison of Figures 3.6(a) & (b) with Figures 3.5(a) & (b) shows that the variations of the hard X-ray spectra with these two parameters are very similar. Recall that we are investigating the hard X-ray spectrum produced by particles which have already been accelerated through a region of length L. Thus it is intuitively
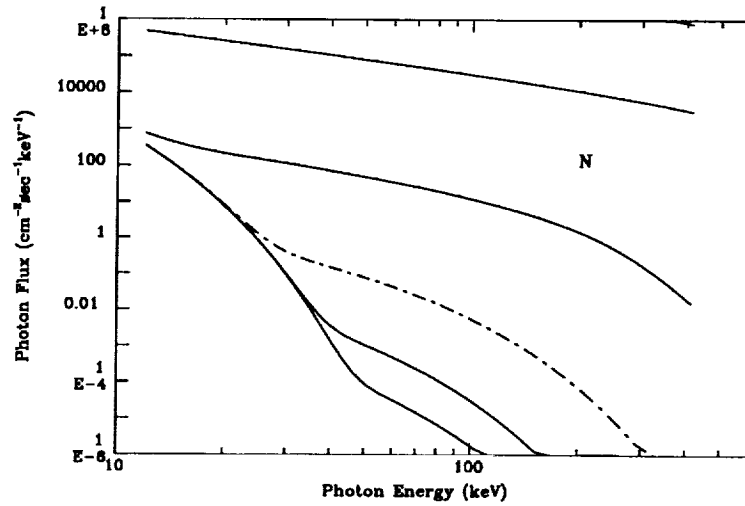
Figure 3.5(a): The density variation of the basic spectrum. From bottom to top, at 100 keV, $N = 10^9$, 10^{10}, 10^{11} (basic), 10^{12}, 10^{13}, and 10^{14} cm^{-3}.

Figure 3.5(b): The same as Figure 3.5(a), except the spectra are constrained as in Figure 3.2(b). At 40 keV, the spectra are ordered in *reverse* from above.

Figure 3.6(a): The variation of the basic spectrum with current sheet length. From bottom to top, at 100 keV, $L = 10^7$, 3×10^7, 10^8, 3×10^8, 10^9, 3×10^9 (basic), 10^{10}, and 3×10^{10} cm.

Figure 3.6(b): The same as Figure 3.6(a), except the spectra are constrained as in Figure 3.2(b). At 50 keV, the spectra are in *reverse* order from above.
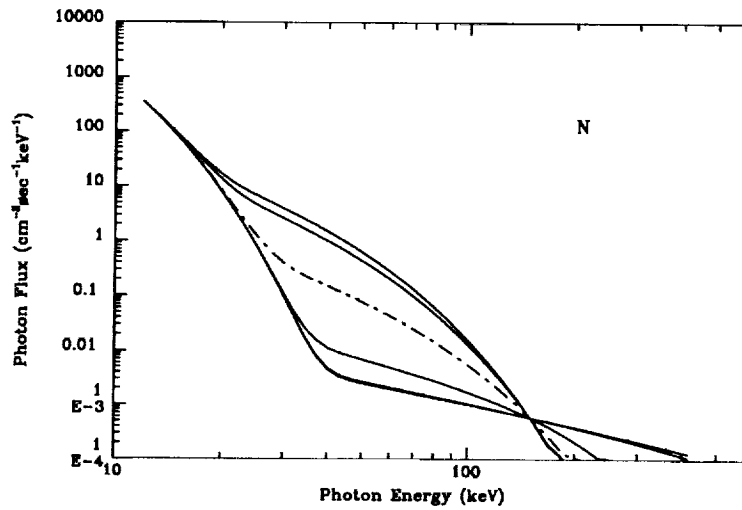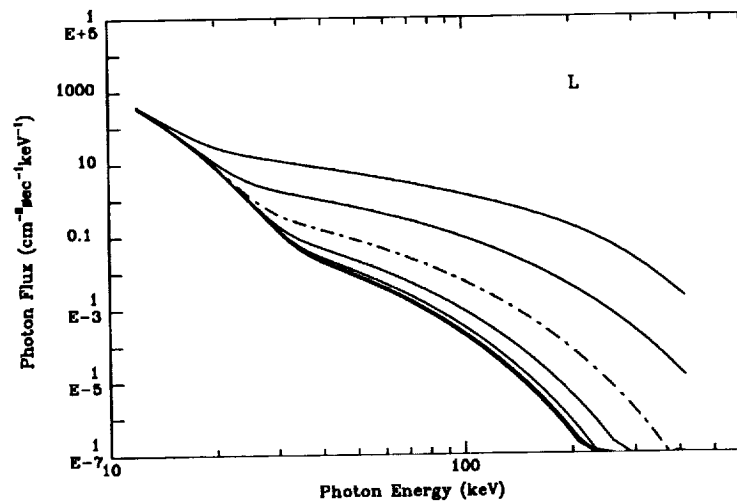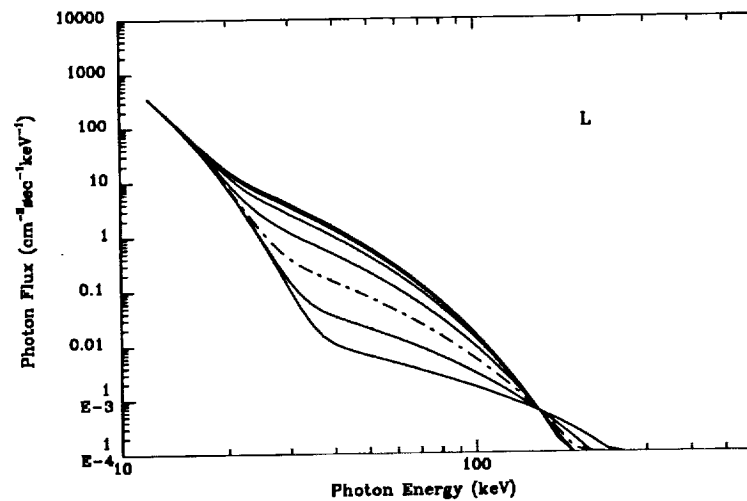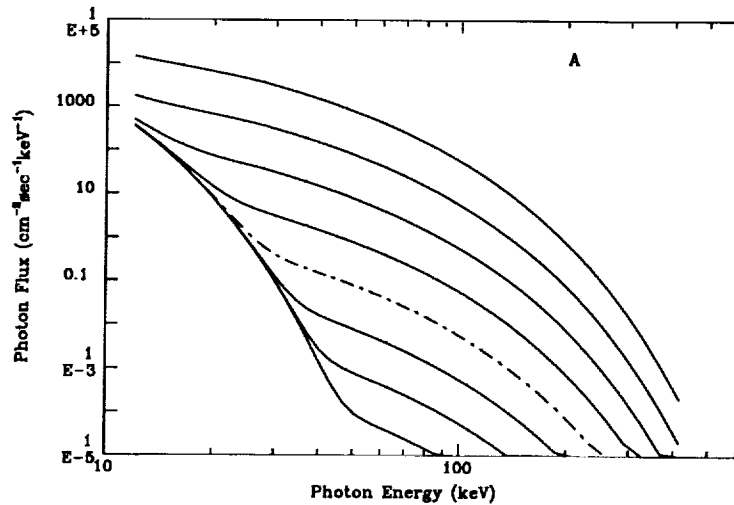
Figure 3.7: The variation of the basic spectrum with thick-target area. From bottom to top, $A = 10^{12}$, 10^{13}, 10^{14}, 10^{15} (basic), 10^{16}, 10^{17}, 10^{18}, and 10^{19} cm^2. Only the nonthermal component is affected.

obvious that increasing the acceleration distance will increase the numbers of particles with high energies.This in turn will increase the nonthermal character of the spectrum, since electrons of energy $\mathcal{E}$ produce photons of all energies $\varepsilon \leq \mathcal{E}$. This is what we see in Figure 3.6(a).

Figure 3.6(b) shows that almost any given change in the nonthermal part of the spectrum can be caused by a corresponding change in *either* N or L. We again see the changes bounded both above (as $\mathcal{E}_{co} \rightarrow \mathcal{E}_{cr}$ for $L \rightarrow 0$) and below (as $\mathcal{E}_{co} \rightarrow \infty$) just as for density.

THICK-TARGET AREA

Varying the area of the thick-target emission simply raises or lowers the nonthermal part of the spectrum relative to the thermal part, as we see in Figure 3.7. It is best used as a constraining parameter for fitting observed spectra, as in the figures above.

3.4   FITTING OBSERVED HARD X-RAY SPECTRA

With the six physically coupled parameters which are at our disposal, the spectra are overdetermined, i.e. a unique fit to an observed spectrum cannot be obtained (cf. Figs 3.4(a) & 3.7, or Figs 3.5 & 3.6). This is not the case for the "usual" modeling, in which the temperature, emission measure, two spectral indices and two break energies are all independent. If the electric field strength is expected to change value during the course of a flare, then all of T, N, and ϵ are required, as

argued above. The emission measure is also expected to increase throughout a flare, as the ambient plasma is continually heated. Heating is also the major consequence of injecting a nonthermal beam of electrons into a thick target, and thus we also expect the area of the heated target to increase as the cumulative effect of the particle injection grows. We are thus led to hold the length, L, of the current sheet constant throughout a flare. Other than these physical but qualitative arguments, there is nothing which demands that this be the case. We could as easily hold N or A constant. Simultaneous observations with high spatial resolution in hard X-rays, as well as both high spatial and high spectral resolution in other wavelength regimes (notably microwaves) are required to resolve this point.

To date, only the flare of 27 June 1980 ($\sim$ 1616 UT) has been observed with very high spectral resolution, using a cooled germanium detector on a balloon flight (Lin *et al.* 1981). This was the observation which discovered the superhot thermal component of hard X-ray bursts. This component became visible near the peak of the event, following which it became increasingly dominant at the lower energies. As the flare progressed, the temperature of this component decreased gradually. This flare provides the ideal testing ground for the ideas presented in this chapter. In order to model the entire flare, additional information is required, as discussed in the last paragraph. I have chosen to demonstrate the plausibility of the thermal/nonthermal model by fitting two of the spectra from this event. These fits are shown in Figures 3.8 and 3.9, corresponding to spectra #1 and #9 of Lin *et al.* (1981), at the beginning and end of the impulsive phase respectively. The former spectrum appears as a "pure" double power-law spectrum, while the latter has a prominent thermal component at the lower energies.

The spectra were fit as follows. For both spectra, I have set L = constant $= 3 \times 10^9$ cm which leaves five free parameters. For Figure 3.9 the temperature and emission measure were first determined by fitting only the six lowest energy channels with a pure thermal bremsstrahlung spectrum and minimizing the χ_ν^2 statistic (Bevington 1969).

This is a standard "goodness of fit" measure which is defined by

$$\chi_\nu^2 \equiv \frac{\sum_{i=1}^{N} \left(\frac{I(\varepsilon) - I_i(\varepsilon)}{\Delta I_i(\varepsilon)} \right)^2}{N - \nu} \ . \tag{3.7}$$

There are N data points in the spectrum, $I_i(\varepsilon)$ is the observed emission for the ith data point, at photon energy ε, $I(\varepsilon)$ is the calculated emission at the same photon energy, $\Delta I_i(\varepsilon)$ is the standard deviation for the observed emission (the size of the vertical error bar), and ν is the number of degrees of freedom, i.e. the number of free parameters available, in calculating $I(\varepsilon)$. In the case of the pure thermal fit discussed here, $N = 6$ and $\nu = 2$ (temperature and emission measure). For the full spectra of Figures 3.8 and 3.9 $N = 30$ and $\nu = 5$ (since we impose $L = constant = 3 \times 10^9$ cm). In the next chapter, for the spectrum of Figure (4.12), $N = 34$ and $\nu = 8$. In general, a value of χ_ν^2 near unity is desirable, and the smallest possible value of χ_ν^2, obtained by varying the input parameters of the fitting function $I(\varepsilon)$, provides the best possible fit to the data using that fitting function. Having $\chi_\nu^2 < 1$ can be construed to mean that either the error bars are too large (the data is too noisy), so that obtaining a good fit is trivial, or that there are too many free parameters in
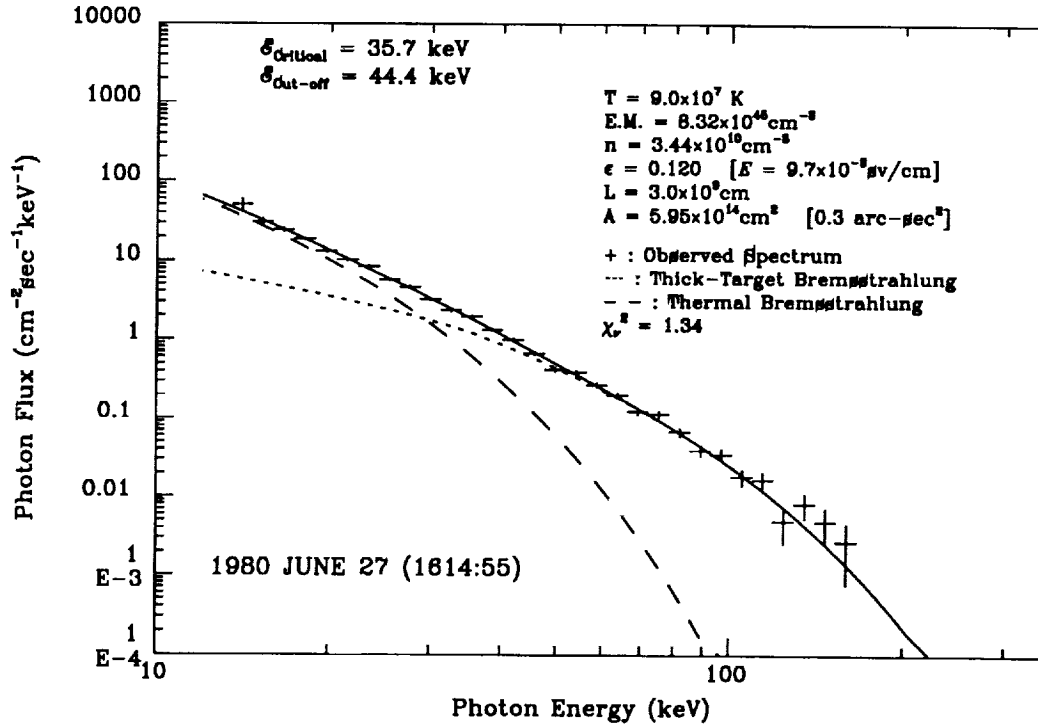
Figure 3.8: A theoretical fit to Spectrum #1 of Lin *et al.* 1981, at the start of the impulsive phase of a flare on 27 June 1980. The dotted line is thick-target bremsstrahlung from runaway electrons accelerated in current sheets. The dashed line is thermal bremsstrahlung. The sum of the two contributions provides an excellent fit to the data.
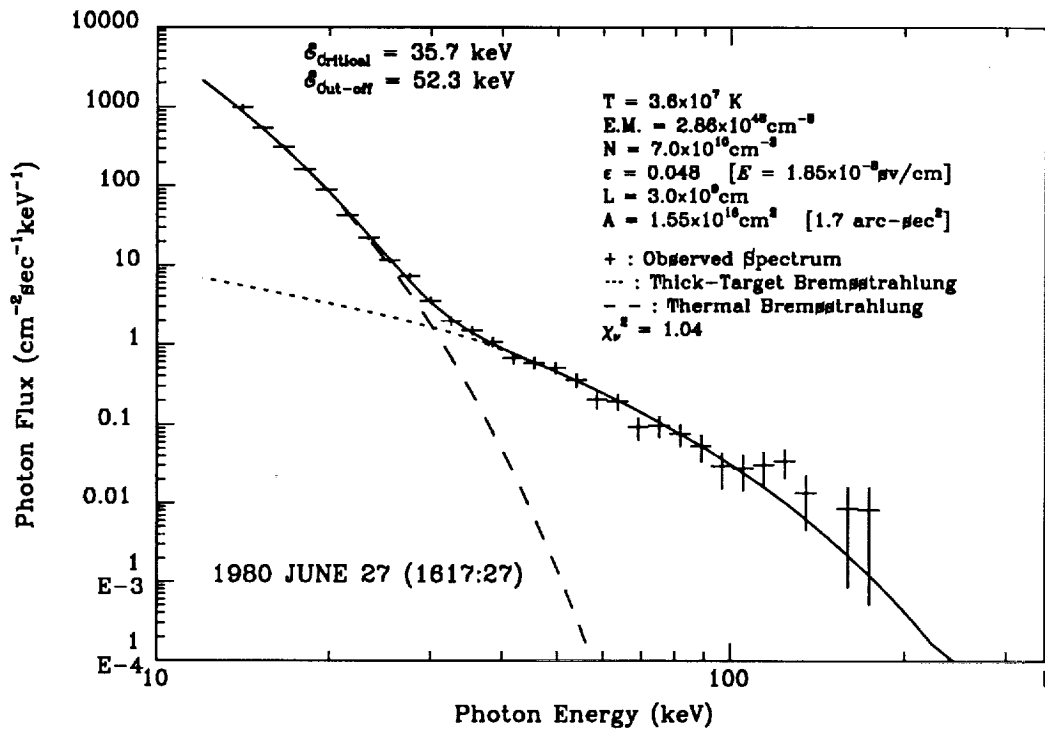
Figure 3.9: A theoretical fit to Spectrum #9 of Lin *et al.* 1981, at the end of the impulsive phase of the same flare as in Figure 3.8. The plotting conventions are the same as in Figure 3.8.

the fitting function.

Having thus determined the temperature and emission measure for Figure 3.9, I then constrain the area by forcing the resulting nonthermal thick-target bremsstrahlung spectrum to go through the point $I(53.96\,\text{keV}) = 0.35$. Determining this constraint was a matter of experimentation. I then chose a density, say $N = 2 \times 10^{11}\,\text{cm}^{-3}$, and calculate χ_ν^2, via equation (3.7), for a range of $\epsilon \equiv E/E_D$, which entails calculating a 30 point spectrum for each ϵ. I thus determine the value of ϵ which gives the lowest value of χ_ν^2 for the chosen density. I then change the density and repeat the process. If the best-fit ϵ gives a lower χ_ν^2 than before, the density was changed in the correct direction. Eventually, the combination of N and ϵ is found which minimizes χ_ν^2. At this point the constraints on area and emission measure are removed, and these quantities are varied independently until χ_ν^2 is truly at a minimum. In the unavoidable preliminary attempts to fit the spectrum, particular notice should be taken of this last step, which can lead to a very efficient choice for the area constaint, in this case $I(53.96\,\text{keV}) = 0.35$.

Figure 3.8 is more challenging to the proposed model, since there is no obvious thermal component to the observed spectrum with which to determine two of the parameters. Nevertheless, by fixing both the area and the emission measure, as in Figures 3-2b, 3-3b, and 3-4b, I could still minimize χ_ν^2. This is done by first fixing T, then iterating with respect to N and ϵ exactly as before. Now, however, there is no guarantee that the lowest possible χ_ν^2 was found, so T must be changed and the process repeated. For Figure 3.8, I stepped through T rather coarsely, in increments of $10^7\,\text{K}$, and found the best fit at $9 \times 10^7\,\text{K}$. It is possible that χ_ν^2 will be slightly lower for T slightly higher (maybe $9.2 \times 10^7\,\text{K}$), but such an exact fit is not necessary to demonstrate the plausibility of this thermal/nonthermal approach.

Figure 3.8 is particularly interesting in that the observation can be well fit only with a significant contribution from thermal bremsstrahlung. This helps alleviate a long-standing problem facing purely nonthermal models, namely that the numbers of electrons required to generate the observed emission, and the energy in these electrons, can be embarassingly large. A direct comparison is possible since, as mentioned, this spectrum is also well fit by a purely nonthermal double power-law description (Lin and Schwartz 1987).

The results are summarized in Table 3.1. The values for the electron and energy fluxes were calculated from equations (3.5) and (3.6). The first line contains the values obtained with the nonthermal distribution function, equations (2.36) and (2.35), the use of which gives

$$F_{\mathcal{E}>\mathcal{E}_{cr}} = \frac{AN}{1.6 \times 10^{-9}} f_{Num}(p_{co})(mc^2)\left(\frac{p_{co}}{mc}\right)\left[\ln\left(\frac{(p_{co}/mc)+\gamma_{co}}{(p_{cr}/mc)+\gamma_{cr}}\right) + \right.$$
$$\left. \int_{\gamma_{co}}^{\infty} \frac{e^{-(mc^2/kT_\perp)(\gamma-\gamma_{co})}}{\sqrt{\gamma^2-1}}d\gamma\right] \text{ electrons sec}^{-1} \qquad (3.8)$$

$$\mathcal{F}_{\mathcal{E}>\mathcal{E}_{cr}} = AN f_{Num}(p_{co})(mc^2)^2\left(\frac{p_{co}}{mc}\right)\left[\frac{p_{co}}{mc} - \frac{p_{cr}}{mc} - \ln\left(\frac{(p_{co}/mc)+\gamma_{co}}{(p_{cr}/mc)+\gamma_{cr}}\right) + \right.$$
$$\left. \int_{\gamma_{co}}^{\infty} \sqrt{\frac{\gamma-1}{\gamma+1}}e^{-(mc^2/kT_\perp)(\gamma-\gamma_{co})}d\gamma\right] \text{ ergs sec}^{-1} . \qquad (3.9)$$

Table 3.1: Nonthermal Fluxes for Figure 3.8

	F electrons sec^{-1}	$\mathcal{F}$ ergs sec^{-1}
Thermal/ Nonthermal	9.5×10^{33}	9.0×10^{26}
Pure Nonthermal	7.9×10^{35}	2.4×10^{28}

The second line of Table 3.1 uses the broken power-law spectral parameters of Lin and Schwartz (1987), and the spectral inversion method of Brown (1971).

It is seen that F is reduced by a factor of more than 80 while $\mathcal{F}$ is reduced by nearly a factor of 30. If these energy fluxes persisted for the course of the flare (~ 180 sec), the present model would represent a savings in the total energy budget of 4×10^{30} ergs, which is rather substantial. There are two reasons for the lower nonthermal fluxes that we see in Table 1. First and obviously, some of the radiation of Figure 3.8 is now produced by thermal electrons, reducing the need for nonthermal particles. The second and more subtle reason is that the low-energy cutoff to the nonthermal electron distribution function is $\mathcal{E}_{cr}$ ($= 35.7$ keV) in this model which is significantly higher than the low-energy cutoff used by Lin and Schwartz ($\mathcal{E}_o = 13$ keV), again leading to fewer nonthermal particles.

The problem of determining the low-energy cutoff of nonthermal electrons is a long-standing one. Invariably, this cut-off is set by the limitations of the detector. The usual argument is that if a power-law photon spectrum is observed down to some minimum photon energy, then the power-law electron distribution which generates it must extend down to a comparable energy, or else the spectrum would begin to flatten out at the lower energies. Thus the low-energy cut-off was taken to be 13 keV for the cooled germanium detector (Lin and Schwartz 1987), 20 - 25 keV for the HXRBS detector on the Solar Maximum Mission satellite, and will probably be $\sim 15 - 18$ keV for the BATSE detectors on the Gamma Ray Observatory satellite. Yet it's rather unsettling to try and believe we are really learning something about the sun this way. In the present model, on the other hand, the low-energy cutoff is precisely $\mathcal{E}_{cr}$ which is determined on physical grounds. We see in Figure 3.8 that the nonthermal spectrum does indeed begin to flatten below this energy, but the difference is made up by thermal bremsstrahlung emission.

It was not intuitively obvious that the thermal/nonthermal model presented here would satisfactorily fit a spectrum such as we see in Figure 3.8 The fact that it does points to the versatility of this approach. In the next chapter, yet another demonstration of this versatility will be presented.

3.5   MODELING HARD X-RAY IMAGES OF 2-RIBBON FLARES

3.5.1   INTRODUCTION

We can employ the scenario envisioned in §3.2, incorporating a large current sheet coaligned with the top of an arcade of magnetic loops, to model how a two-ribbon flare would look in hard X-rays. An approach similar to this may in fact be used in conjunction with *any* model for the hard X-ray production.

An instrument capable of imaging the sun in hard X-rays ($\sim$ 20 – 1000 keV) with $\sim$ 1 arc-second spatial resolution is currently under development at NASA's Goddard Space Flight Center, providing the motivation for this modeling. It uses the technique of Fourier-transform imaging, involving pairs of collimated slit-slat grids of various slit-slat spacings and orientations. Each pair of grids is separated by $\sim$ 6 feet, and together this pair is called a subcollimator. Further instrumental details need not concern us (see Crannell 1989 and Prince *et al.* 1988 and references therein) but I would like to recap some of its history. As originally proposed, this balloon-borne instrument was called GRID (Gamma Ray Imaging Device) and had 34 subcollimators arranged in an array. The axis of the array was then pointed at the sun and translated, perpendicular to itself, causing the entire array to execute a circular motion parallel to the plane of the solar disk, generating the Moire patterns which, upon deconvolution, produced the images. Due to funding cuts, the project had to be scaled down to 22 subcollimators, then it was cancelled altogether. Finally, the project was revived as HEIDI (High Energy Imaging Device). In its current modest form, HEIDI has only two subcollimators, but now they are rotated around their axis, providing adequate coverage of the u-v plane to $\sim$ 5 arc-second resolution. There are plans to upgrade it to 4 subcollimators. In its final envisioned form, as HEISPEC (High Energy Imaging Spectrometer) to be incorporated in the sought-after HESP (High Energy Solar Physics) satellite, the instrument will have < 1 arc-second spatial resolution.

The modeling discussed in this section was performed with a 22-element GRID instrument in mind, and I will refer to it as such. It is important to note, however, that except for the computer simulations in §3.5.3, the ideas which make up the modeling technique are instrument-independent.

There are three distinct regions of hard X-ray emission, two of which have the same characteristics. These are the "footpoint ribbons", whose non-thermal emission is produced by electrons, energized in and then scattered out of the current sheet, streaming down the magnetic loops and impinging on the chromospheric plasma, where they emit thick-target bremsstrahlung (cf. Fig 1.3). These ribbons are modeled with either a "hard" broken power-law spectrum, or with a "softer" single power-law spectrum.

The third emission region modeled is near the top of the arcade. Here, Joule heating by the current sheet will locally increase the temperature above that of the ambient coronal plasma. This is modeled with a thermal bremsstrahlung spectrum. In addition, the current sheet may generate some low-level plasma turbulence, which may provide further acceleration and/or heating through stochastic processes. This is not modeled here, however, since the more complex theory called for is not justified

by this zeroth-order model for GRID.

Also not modeled is a possible energy gradient along the length of the ribbons. A fraction of electrons will remain in the current sheet longer than average, reaching higher energies at locations farther down the sheet. Because of the directionality of the electric field and current, these highest energy electrons will exist only near one end of the sheet. When finally scattered out, they are capable of producing higher energy bremsstrahlung than their counterparts farther up the current sheet.

3.5.2 PROCEDURE

Recall that the flare image will have three parts: 2 footpoint ribbons which I assume to be identical, and the higher-altitude region at the top of the arcade. The reader is urged to refer back to Figure 1.3. The procedure employed to construct the model hard X-ray images has seven steps.

1.) Pick an image geometry, that is choose the dimensional size of the model flare, the ribbon orientation with respect to the solar equator, and the angular distance from the center of the solar disk.

I assumed a total flare area of 10^{19} cm^2, apportioned as shown in Figure 3.10. I also assume that the top of the arcade is 10^9 cm above the ribbons, giving rise to projection effects (cf. Fig 1.3). Some of the geometrical possibilities are shown in Figure 3.11. The top three panels (a, b, and c) depict the flaring magnetic arcade of Figure 3.10 (or 1.3) oriented parallel to the sun's equator (i.e. East-West) at 45° East longitude, disk center, and 75° West longitude respectively. The bottom three panels show the same flare at the same longitudes, but with a North-South orientation. Note that as the longitude changes, the higher-altitude arcade top is projected eastward or westward due to the curvature of the sun. In panel 3.11(d), this results in only two components being visible, the arcade top being projected on top of (and thus enhancing the brightness of) one of the footpoint ribbons. Similarly, a flare occurring near the limb of the sun, as in 3.11(c) and 3.11(f), is greatly foreshortened. More complicated flare geometries, such as curved or non-parallel or sheared ribbons, are of course possible.

2.) Pick an emission model, that is choose a combination of thermal (at any temperature) and nonthermal (either "hard" or "soft") X-ray spectra.

For a large two-ribbon flare, I used a fictional,"typical" spectral flux of photons detected at the Earth — obtained from looking at many flares in the literature, e.g. Lu and Petrosian (1989, 53 flares), and Kaastra (PhD. Dissertation, Univ. of Utrecht, Netherlands, 1985, Chapter 6, 67 flares).

Such a typical "hard" broken power-law spectrum is:

$$\frac{dN}{d\varepsilon} = 10^7 \varepsilon^{-3.5} \quad (20 < \varepsilon < 80 \,\text{keV}) ,$$

$$\frac{dN}{d\varepsilon} = 8 \times 10^8 \varepsilon^{-4.5} \quad (\varepsilon > 80 \,\text{keV}) . \tag{3.10}$$

A typical "softer"non-thermal photon spectrum is:

$$\frac{dN}{d\varepsilon} = 2 \times 10^8 \varepsilon^{-5} . \tag{3.11}$$

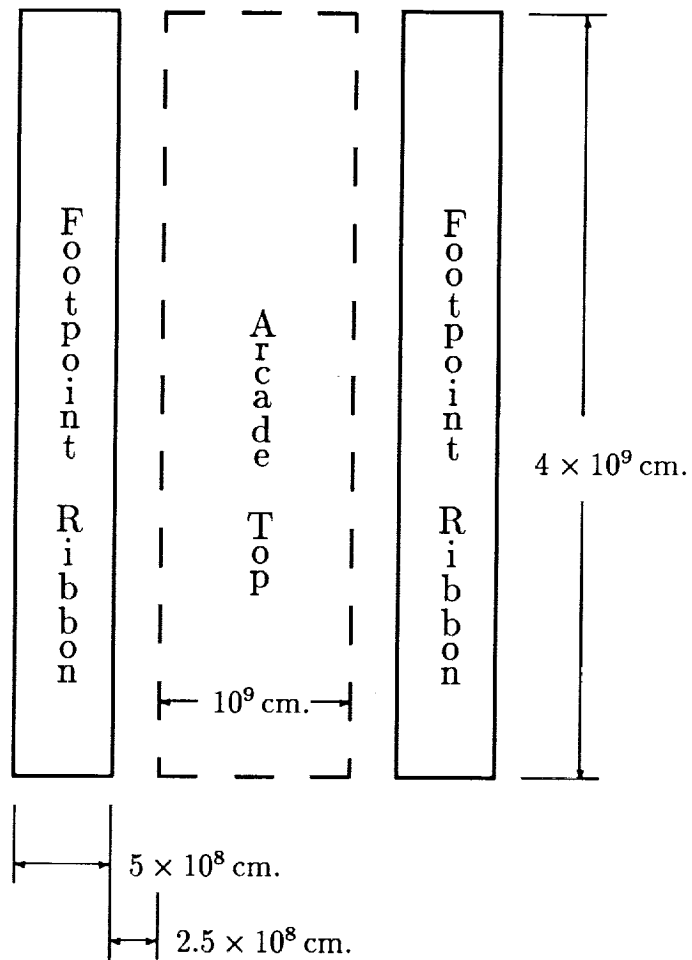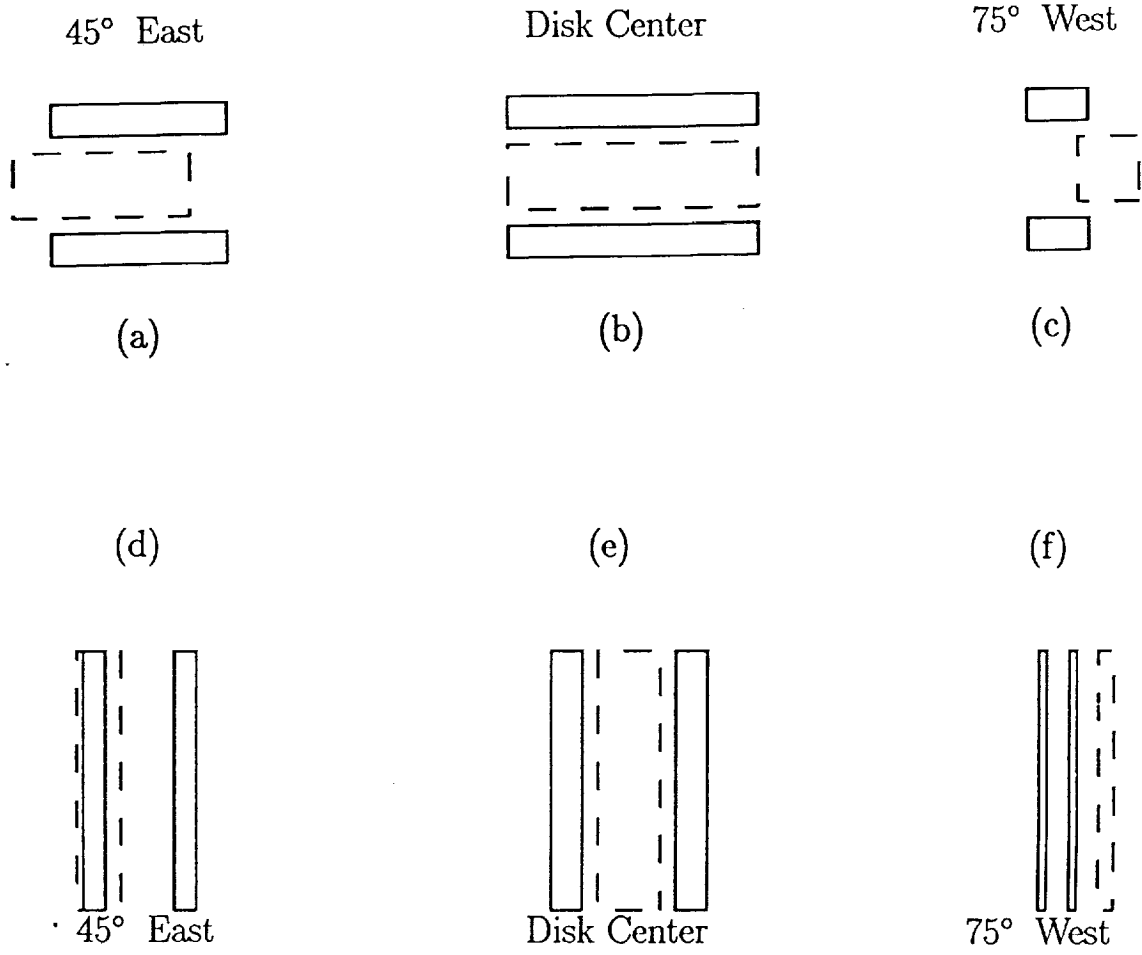Figure 3.10: Model Flare Size

East - West Ribbon Orientation

Figure 3.11: Model Flare geometries

The premultipliers and energy spectral indices in these nonthermal spectra can be changed as needed.

A typical thermal spectrum is:

$$\frac{dN}{d\varepsilon} = 10^6 \varepsilon^{-1.4} \exp(\varepsilon/kT) \,. \tag{3.12}$$

in which only the premultiplier and temperature can be varied (see eqn [3.3]).

3.) Identify the thermal (nonthermal) emission with the arcade top (footpoint ribbons), and calculate the projected area of each of these components.

To 1st - order, this involves multiplying the East-West dimensions by $\cos\theta$ where θ is the longitude angle. The North-South dimensions are similarly multiplied by the cosine of the latitude. In these models, the flare is assumed to be on the solar equator, so the North-South dimensions are unaffected.

4.) Integrate each spectrum over energy.

Since GRID's energy range is 20 – 1000 keV, the detected flux at the Earth, $I_{n\oplus}$, of photons having energies $\varepsilon > n$ keV is

$$I_{n\oplus} = \int_{n(\geq 20)}^{1000} \frac{dN}{d\varepsilon} d\varepsilon \quad \text{photons cm}^{-2}\text{s}^{-1}. \tag{3.13}$$

The results for the three spectra given above (thermal and both hard and soft non-thermal) are given in Table 3.2.

Table 3.2: Detected Photon Fluxes (photons cm^{-2} s^{-1})

Spectrum	$I_{20\oplus}$	$I_{40\oplus}$	$I_{60\oplus}$	$I_{80\oplus}$	$I_{100\oplus}$	Model
"Hard"	2,216	375.3	123.5	49.9	22.85	1
"Soft"	312.5	19.53	3.86	1.22	0.50	2
Thermal						
$T = 10^7$ K	10^{-6}					
3×10^7	14.86	0.003	10^{-6}			
5.8×10^7	1,064	8.27	0.09	10^{-3}	10^{-5}	1
10^8	8,622	377.1	22.44	1.53	0.113	2
3×10^8	81,250	18,770	5,582	1,858	660.4	

5.) Multiply by $4\pi(1\,\text{AU})^2$ to get total photons emitted per second by the flare. This assumes isotropic emission.

$$I_n = 4\pi(1\,\text{AU})^2 I_{n\oplus} \quad \text{photons s}^{-1} \text{, from the sun.} \tag{3.14}$$

6.) Divide this rate by the projected area of the relevant component of the flare. This gives the photon flux from each spatial component at the sun.

7.) Use this information as input to a simulation routine to determine what GRID will actually see.

3.5.3 RESULTS AND DISCUSSION

Simulations were performed, by Dr. Gordon Hurford at the California Institute of Technology, for two models on the geometry of Figure 3.11(a).

$$Model\ 1\ \left\{ \begin{array}{l} \text{Footpoints: Hard Non-Thermal} \\ \text{Arcade Top: } T = 5.8 \times 10^7 \text{ K.} \end{array} \right.$$

$$Model\ 2\ \left\{ \begin{array}{l} \text{Footpoints: Soft Non-Thermal} \\ \text{Arcade Top: } T = 10^8 \text{ K.} \end{array} \right.$$

The photon fluxes associated with these models are indicated in Table 3.2. Maps were generated of the spatial distribution of photons having energies $> 20, 40$, and 80 keV for each model, showing the energy dependence of the emission. These are Figures 3.12(a) – (c) and 3.13(a) – (c).

Low-level background noise was added, and atmospheric attenuation was taken into account. Both processes are energy-dependent in the simulations. Each map simulates a 2-second observation.

The maps were obtained using a straightforward application of the CLEAN algorithm. No additional special care was taken (intentionally) in either generating or cleaning the maps. In this sense, these maps represent a pessimistic view of GRID's true capabilities.

The large size of the simulated flare produced a significant response in only the coarser of GRID's subcollimators. In Figure 3.12(a) I have shown the input "flare". This position and orientation remains the same for all 6 maps.

Figures 3.12(a) – (c) show the simulated images for a flare represented by Model 1 above. The three images show the energy dependence of the emission. Figure 3.12(a) represents the total photon flux that GRID would observe, i.e. $\varepsilon > 20$ keV. The following two figures show the flux at successively higher energies, $\varepsilon > 40$, and > 80 keV respectively. Since this model has a hard nonthermal spectrum at the footpoint ribbons, and a rather moderate thermal component, we expect the footpoint emission to dominate, and it does. Notice in Figures 3.12(a) and (b), that the brightest emission is straddling a more modest "source". This would be a signature of the hard X-ray production scenario sketched in connection with Figure 1.3 when particle acceleration is as important as the plasma heating. In fact, if we employ equation (3.6) to calculate the energy flux of the nonthermal electrons which produce the thick-target spectrum (3.10), we find 5×10^{29} ergs deposited in two seconds. The energy in the thermal electrons, on the other hand, is $\sim (3/2)NkTV$, where $V = EM/N^2$ is the volume of the thermal plasma. For the chosen geometry, the volume is $\sim 2 \times 10^{27}$ cm^3 while the emission measure is EM $= (10^6/1.3 \times 10^6)(kT)^{0.1} \sim 9 \times 10^{47}$ cm^{-3}. This gives us the density $N \sim 1.7 \times 10^{10}$ cm^{-3}, and hence the energy $\mathcal{E} \sim 6 \times 10^{29}$ ergs, comparable to the nonthermal

electrons' energy. Another characteristic would be that the central component, being thermal, would fall off much quicker at high energies than the nonthermal emission. This is in fact seen in Figure 3.12(c).

A similar calculation for Model 2 yields a nonthermal electron energy of 2.0×10^{29} ergs for 2 seconds, and a thermal electron energy of 1.1×10^{30} ergs, nearly an order of magnitude greater. Thus we expect the thermal to completely dominate the observed flare, except at the highest energies. This is seen in Figures 3.13(a) – (c). In the last of these figures, it is difficult to say how much of the observed structure is real, as opposed to noise, since the total integrated flux is only 3.7 photons cm^{-2} s^{-1}.

Comparing the rate at which the total flux falls off with energy in the two models, points to the great importance of such high resolution imaging for localizing the thermal and nonthermal emissions in a flare. The fact that the emission in Model 2 drops by a factor of 2,500 over a range of 60 keV is very strong evidence that it is of a purely thermal nature. Similarly, the total flux in Model 1 drops by only a factor of 60 over 60 keV, indicating that much of the emission must be of nonthermal origin. In particular, the highest energy emission seen is almost certainly of a purely nonthermal nature. Even if this emission were obscured by thermal emission in the lowest energy channels (which it is not in this case), it would still be readily identifiable at the highest energies, since the thermal emission falls off so rapidly. If the temperature of the thermal plasma is much in excess of 10^8 K, we are back in the realm of the simple thermal models (see Chapter 1 and Table 3.2) in which nonthermal emission, even if present, will go largely unobserved.

The development of a hard X-ray imaging instrument, such as GRID, is a long-awaited and scientifically significant step forward in the study of solar flares, as demonstrated in this section. Such an instrument, having high spatial, spectral, and temporal resolutions, will give us an unprecedented view of, and information about, the solar flare phenomenon. Of primary importance is the ability to spatially separate the relative contributions of thermal and nonthermal components of the emission. As stated in Chapter 1, and repeated here, the scenario modeled in this section is only one of several possibilities. Thus a GRID-like instrument will enable us to discriminate among various theoretical models, which in turn helps us to refine our understanding of solar flares.

TOTAL INTEGRATED FLUX: 5,720 photons cm^{-2} s^{-1}
CONTOURS: 10, 30, 50, 70, 90% of peak flux.
SUBCOLLIMATORS: 10 of 22 had significant response.

The brightest contours are clearly associated with the footpoints. Note especially the 50% contours between the footpoints and compare with the nominal fluxes for $I_{20\oplus}$: Non-Thermal, 2,216; Thermal, 1,064. In this map, as in all of the following maps, there is an offset of 1 pixel ($\sim$ 2 arc-seconds).
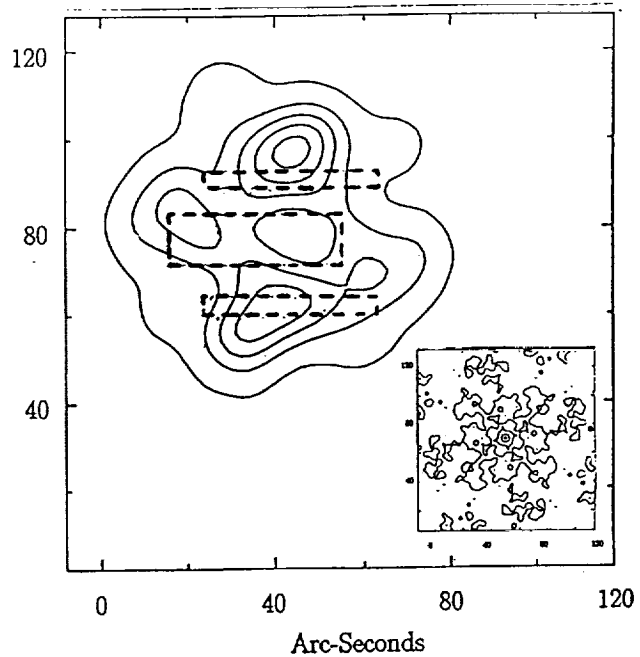
Figure 3.12(a): Simulated hard X-ray emission for GRID Model 1 — $I_{20\oplus}$. The input "flare" is superimposed on the emission. The inset shows the beam used in the simulations.

MODEL 1 — $I_{40\oplus}$

TOTAL INTEGRATED FLUX: 736 photons cm^{-2} s^{-1}
CONTOURS: 10, 30, 50, 70, 90% of peak flux.
SUBCOLLIMATORS: 12 of 22 had significant response.

The brightest contours are again clearly associated with the footpoints, which are now showing an elongation.

Arc-Seconds

Figure 3.12(b): Simulated hard X-ray emission for GRID Model 1 — $I_{40\oplus}$

MODEL 1 — $I_{80\oplus}$

TOTAL INTEGRATED FLUX: 90 photons cm^{-2} s^{-1}
CONTOURS: 10, 30, 50, 70, 90% of peak flux.
SUBCOLLIMATORS: 12 of 22 had significant response.

Above 80keV in this model, only the footpoint ribbons are detectable above noise levels.

Arc-Seconds
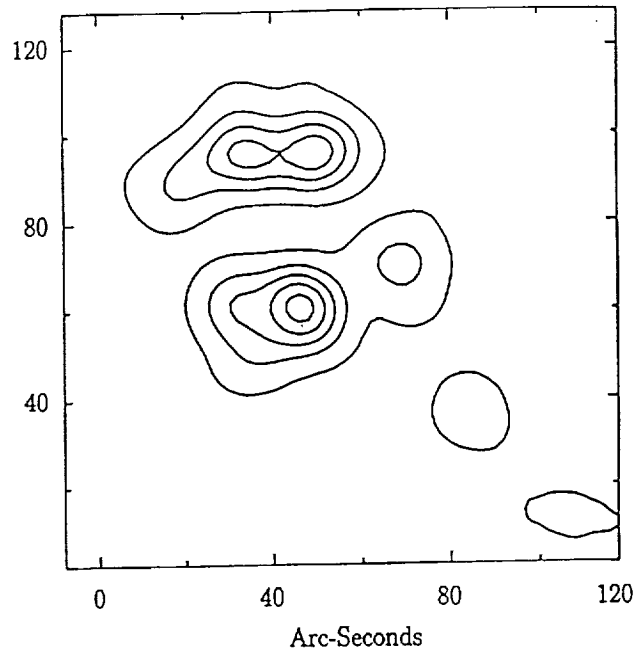
Figure 3.12(c): Simulated hard X-ray emission for GRID Model 1 — $I_{80\oplus}$

MODEL 2 — $I_{20\oplus}$

TOTAL INTEGRATED FLUX: 9,216 photons cm^{-2} s^{-1}
CONTOURS: 10, 30, 50, 70, 90% of peak flux.
SUBCOLLIMATORS: 12 of 22 had significant response.

The emission in Model 2 is entirely due to the thermal component at energies up to ~80keV. Again, the 1 pixel offset is apparant, but now in the East-West direction.
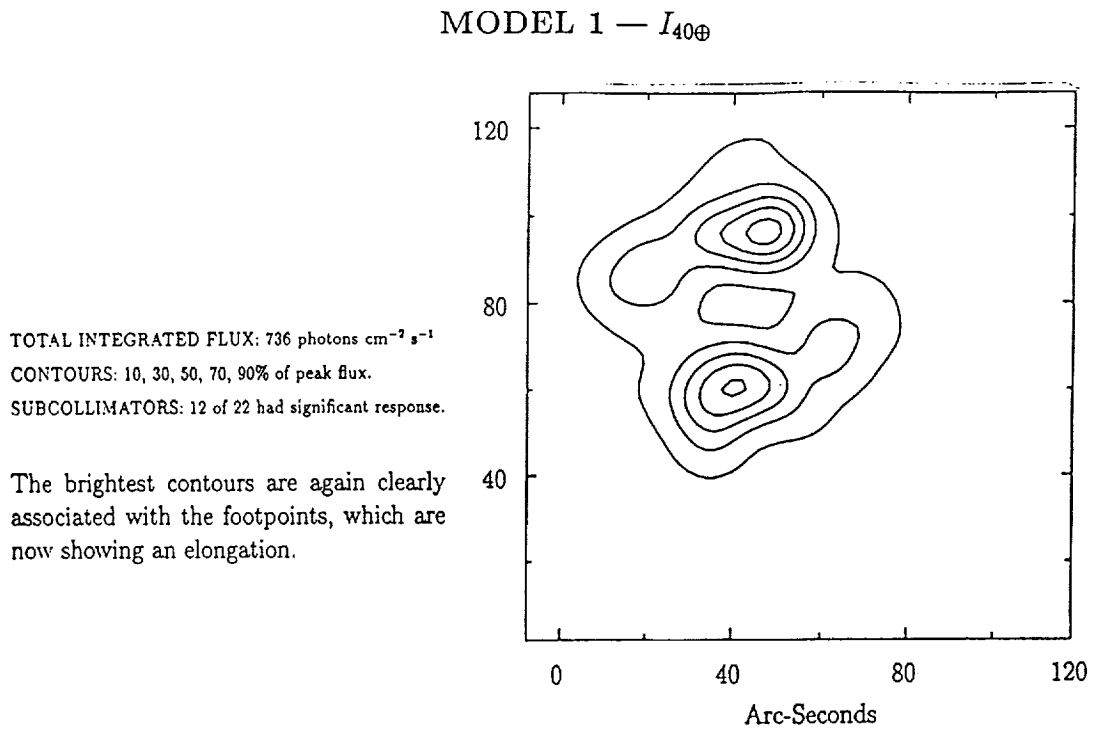
Figure 3.13(a): Simulated hard X-ray emission for GRID Model 2 — $I_{20\oplus}$

MODEL 2 — $I_{40\oplus}$

TOTAL INTEGRATED FLUX: 429 photons cm^{-2} s^{-1}
CONTOURS: 10, 30, 50, 70, 90% of peak flux.
SUBCOLLIMATORS: 12 of 22 had significant response.

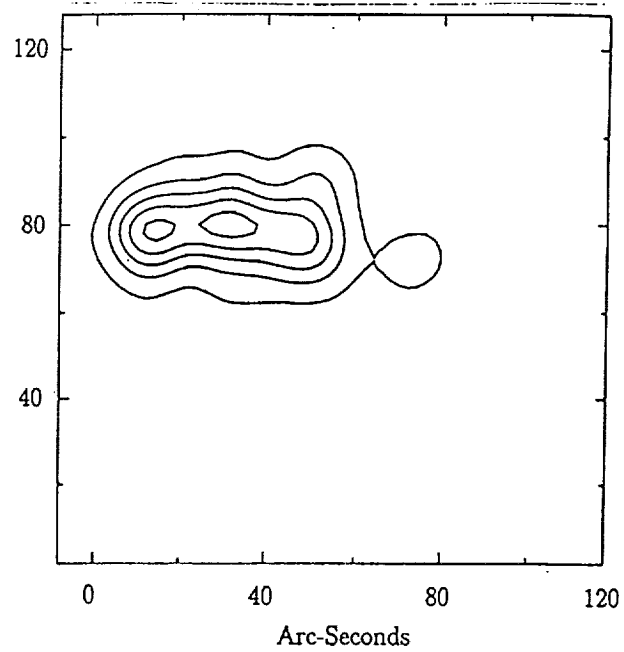Again, all of the emission is coming from the hot thermal plasma near the top of the magnetic arcade.
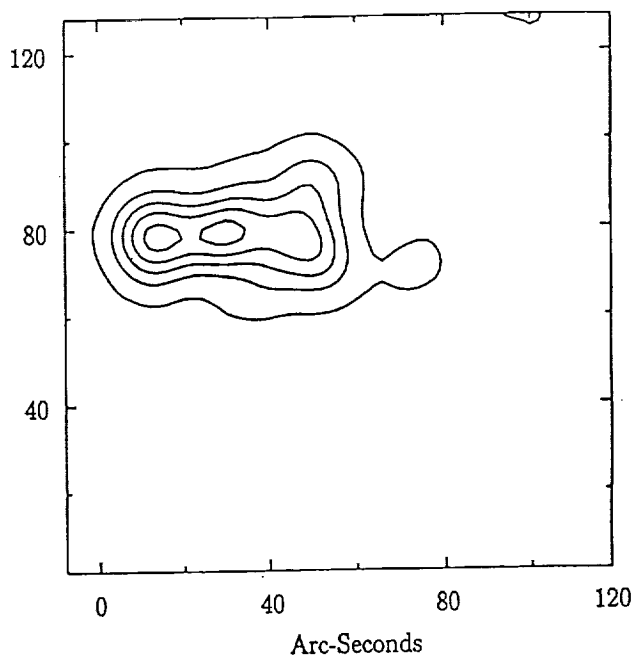
Figure 3.13(b): Simulated hard X-ray emission for GRID Model 2 — $I_{40\oplus}$

MODEL 2 — $I_{80\oplus}$

TOTAL INTEGRATED FLUX: 3.7 photons cm^{-2} s^{-1}
CONTOURS: 10, 30, 50, 70, 90% of peak flux.
SUBCOLLIMATORS: 22 of 22 used by GRID for this map.

Near 80 keV in Model 2, the thermal and non-thermal emissions become comparable. This, together with the weakness of the source at these high energies, produces the complicated map shown. Though difficult to interpret, the source geometry is clearly different from that of the purely thermal emission at lower energies.
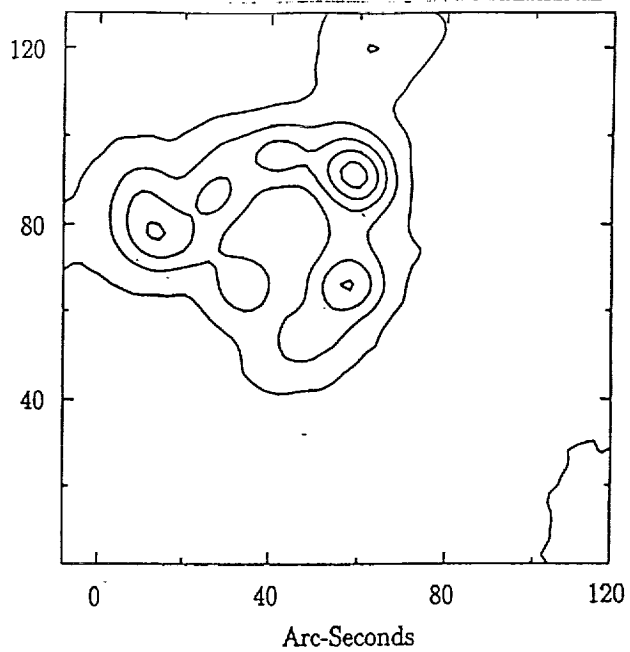
Arc-Seconds

Figure 3.13(c): Simulated hard X-ray emission for GRID Model 2 — $I_{80\oplus}$

Chapter 4

THERMAL/NONTHERMAL MICROWAVES

4.1 INTRODUCTION

Impulsive microwave radiation carries a great deal of information about the physical conditions in the solar atmosphere immediately after the onset of a flare. The microwaves, at frequencies ranging from 1 or 2 GHz to ~ 100 GHz, are widely agreed to be produced primarily by gyrosynchrotron radiation from mildly relativistic electrons spiralling along magnetic field lines in the flaring region.

The argument for gyrosynchrotron emission can be made by eliminating the other two radio emission mechanisms, namely bremsstrahlung and plasma radiation (Kundu 1965). Plasma radiation in its various forms is narrow-band emission, resulting from collective motions of plasma particles in response to some disturbance. These motions then either generate, or couple to, an electromagnetic wave in the plasma having a frequency matching that of the particles' oscillations. This frequency could be, for example, the plasma frequency ($\nu_p = \sqrt{Ne^2/\pi m}$), or the upper hybrid frequency ($\nu_h = \sqrt{\nu_p^2 + \nu_b^2}$ with the electron gyrofrequency $\nu_b = eB/(2\pi mc)$). Here N is the plasma density, e and m are the electron charge and mass respectively, B is the magnetic field strength in Gauss, and c is the speed of light. For the solar corona, the plasma frequency is generally less than 10^9 Hz = 1 GHz, since the density is less than 10^{10} cm^{-3}. The upper hybrid frequency can lie in the microwave regime for strong enough magnetic fields. Thus, although such radiation is frequently observed in the MHz range at meter wavelengths (cf. Fig 1.1), it is less seen in the microwave regime ($\nu >\sim 1$ or 2 GHz), and in any event, is narrow band emission, in contrast to the broad band ($\sim 1 - 100$ GHz) radiation of interest here.

An individual electron in a plasma is accelerated in the Coulomb field of other charged particles, and emits bremsstrahlung radiation, as discussed in §3.1. For microwaves, in contrast to X-rays, the energy of the radiation is much less than the kinetic energy of the electron ($\varepsilon \sim \Delta\mathcal{E} \ll \mathcal{E}$), meaning that small accelerations due to distant encounters with other charged particles are the dominant factor. In the sun's atmosphere, however, the presence of a magnetic field provides another acceleration mechanism, the centripetal acceleration due to the Lorentz $\vec{v} \times \vec{B}$ force which causes the electron to spiral around a magnetic field line. The frequency with

which the electron completes a circuit of the field line is known as the gyrofrequency,
$\nu_b = eB/(2\pi mc) \sim 2.8 \times 10^6 B$ where B is the magnetic field strength in Gauss and
c is the speed of light.

The centripetal acceleration imparted to the electron produces radiation having
different characteristics, depending on the energy of the electron involved (cf. Dulk
1985). A nonrelativistic electron emits radiation, over a narrow range of frequencies,
at the gyrofrequency and perhaps at the first few harmonics of ν_b. This is the case
in the chromosphere and quiet corona, at temperatures of less than a few million
degrees, where the electron thermal velocity is < 1 - 2% of the speed of light. During
flares, however, v_{th} can exceed $0.1c$, and runaway acceleration in current sheets
can impart very high energies to some electrons. For these latter particles, the
ultrarelativistic approximation ($\gamma \gg 1$), leading to the formulae for synchrotron
radiation, could perhaps be used. For an isotropic pitch angle distribution, this is
broad band emission centered at harmonic number $s \simeq (\gamma \sin \theta)^3$, where γ is the
Lorentz factor, and θ is the angle between the magnetic field and the wave vector
(our line of sight). Unfortunately, flare conditions are such that most of the radiating
electrons are in the mildly relativistic regime, where no accurate approximations can
be made. Such radiation by mildly relativistic particles is called gyrosynchrotron
radiation.

The free-free emission is proportional to $N^2 T^{-1/2}$ (cf. Ramaty and Petrosian
1972) and gyrosynchrotron emission is proportional to $NT^a B^b$, with a and b both
greater than 1 (cf. Crannell *et al.* 1988). Thus the ratio of free-free to gyrosyn-
chrotron emission is proportional to $N/(T^{a+.5} B^b)$. General conditions in the solar
atmosphere are such that this ratio can be either greater or less than one. During
flares however, both magnetic field strengths and especially temperatures are so high
that the contribution from bremsstrahlung in the microwave region of the spectrum,
is generally negligible compared to gyrosynchrotron emission. We are thus left with
gyrosynchrotron radiation as the mechanism for generating microwave bursts during
solar flares.

In principle, high quality spectral observations of impulsive microwave emission,
supplemented by spatial information, can provide information about not only the
ambient magnetic field and various plasma parameters (e.g. emission measure and
temperature for thermal models, electron energy distribution for nonthermal mod-
els) in the emission region, but also the source size and geometry. This is because
the lower microwave frequencies are generally optically thick, while the higher fre-
quencies are optically thin. This contrasts with the X-rays, which are all optically
thin.

Such high quality observations, as represented by those obtained from the
frequency-agile interferometer at Owens Valley Radio Observatory (OVRO) (Stäli,
Gary, and Hurford 1989, 1990; hereafter SGH1 and SGH2), are now available. These
observations are providing strong challenges to the conventional modeling of mi-
crowave bursts as being produced either by ultra-hot ($T > 10^8 K$) isothermal plas-
mas or by simple power-law electron distributions (SGH1). In particular, the OVRO
observations have shown that: (a) $\sim 80\%$ of microwave bursts show complex spectra,
containing two or more peaks in flux density; (b) slopes on the low-frequency side of
the spectrum are frequently steeper than expected for nonthermal gyrosynchrotron
radiation; and (c) the peak frequency of the spectrum does not shift as expected

during flare development.

Some aspects of the spectra can be modeled as a superposition of spatially distinct source regions, and/or of other plasma or magnetic field inhomogeneities. Simultaneous high-resolution microwave imaging of the bursts can help to clarify the spatial structures involved in complex events (Velusamy and Kundu 1982; Kundu *et al.* 1982; Holman *et al.* 1989; Willson *et al.* 1990; Bogod *et al.* 1990; Gary and Hurford 1990). It is, however, difficult to see how inhomogeneities can produce steep optically thick spectral slopes and relatively fixed peak frequencies without making very special *ad hoc* assumptions on a case by case basis.

In addition, many events show a coevolution in time of both the primary and secondary components (SGH1, SGH2), providing strong evidence that they have a common origin. In modeling the components independently one is faced with a difficult theoretical conundrum. If the spectral components arise in the same location, how does the plasma support two non-interacting radiating populations of electrons for the duration of the burst? Conversely, if they arise in different locations, through what mechanism are these different locations coupled, strongly enough for them to coevolve throughout the course of the burst?

In this chapter, I will investigate microwave spectra using the thermal/nonthermal approach. I employ the basic formulae of gyrosynchrotron radiation, using no approximations, and use for the electron distribution function a nonthermal tail joined to a bulk Maxwellian (eqns [2.49] – [2.54]). Although hybrid distribution functions have been used before (Emslie and Vlahos 1980; Mok 1983), and the effects of a thermal plasma on a nonthermal population have been touched upon by various authors (e.g. Ramaty 1969; Klein 1987), the general approach taken here both uncovers some important new effects, and can serve to clarify some of the previous work.

In §4.2 I briefly review the gyrosynchrotron radiation formulae, and discuss the calculations. In §4.3 I sketch out how this radiation can be related to current sheets. §4.4 is devoted to an analysis of the resultant theoretical spectra, and §4.5 relates these results to observations and demonstrates the applicability of the model. Finally in §4.6 we summarize the results of our study.

4.2 GYROSYNCHROTRON RADIATION

4.2.1 GYROSYNCHROTRON FORMULAE

The following formalism is based on Ramaty (1969), as corrected by Trulsen and Fejer (1970). Further details may be found in Ramaty (1969).

The radiation intensity from a *homogeneous* source region is

$$I_{\pm}(\nu, \theta) = \frac{j_{\pm}}{\kappa_{\pm}} \left[1 - \exp(-\kappa_{\pm} D) \right] \quad \text{ergs(sec sterad Hz cm}^2)^{-1} . \qquad (4.1)$$

Here j is the emissivity, κ is the absorption coefficient, D is the depth of the source, ν is the observation frequency, θ is the angle between the wave normal and the magnetic field direction ($0 \leq \theta \leq \pi$), and $+$ ($-$) refers to the ordinary (extraordinary) mode of polarization. The quantity κD is known as the optical depth of the source,

and many authors denote it by τ. Note that equation (4.1) is radiation intensity per unit *source* area. The total intensity is then $I = I_+ + I_-$.

For an electron distribution function of the form $N_r f(\gamma, \phi)$, where N_r is the number density of radiating electrons, $\gamma = (1 - \beta^2)^{-1/2}$ is the Lorentz factor with $\beta = v/c$, ϕ is the electron pitch angle, and

$$2\pi \int_1^\infty d\gamma \int_{-1}^1 d(\cos\phi) \, f(\gamma, \phi) = 1 \, , \qquad (4.2)$$

the emissivity and absorption coefficient are given by

$$j_\pm(\nu, \theta) = 2\pi N_r \int_1^\infty d\gamma \int_{-1}^1 d(\cos\phi) \, f(\gamma, \phi) \, \eta_\pm(\nu, \theta, \gamma, \phi) \, , \qquad (4.3)$$

$$\kappa_\pm(\nu, \theta) = \frac{2\pi}{m\nu^2 n_\pm} N_r \int_1^\infty \left\{ d\gamma \int_{-1}^1 d(\cos\phi) \, \eta_\pm(\nu, \theta, \gamma, \phi) \times \right.$$
$$\left. \left[-\beta\gamma^2 \frac{\partial}{\partial\gamma} \left(\frac{f(\gamma, \phi)}{\beta\gamma^2} \right) + \frac{n_\pm \beta \cos\theta - \cos\phi}{\beta^2 \gamma \sin\phi} \frac{\partial}{\partial\phi} f(\gamma, \phi) \right] \right\} \, , \qquad (4.4)$$

where n is the index of refraction (given below) and η is the gyrosynchrotron emissivity for a single electron:

$$\eta_\pm(\nu, \theta, \gamma, \phi) = \frac{2\pi e^2}{c} \nu^2 \sum_{s=-\infty}^{\infty} \frac{n_\pm}{1 + a_{\theta\pm}^2} \left[a_{\theta\pm} \left(\frac{\cot\theta}{n_\pm} - \beta \frac{\cos\phi}{\sin\theta} \right) J_s(x_s) - \beta \sin\phi \, J_s'(x_s) \right]^2$$

$$\times \delta\left(\nu - \frac{s\nu_b}{\gamma} - n_\pm \nu\beta \cos\phi \cos\theta\right) \, . \qquad (4.5)$$

Here, $x_s = (s n_\pm \beta \sin\phi \sin\theta)/(1 - n_\pm \beta \cos\phi \cos\theta)$, J_s is a Bessel function of order s, and the prime denotes differentiation with respect to the argument. For ν greater than the radiation cutoff frequencies, we have the restriction $s > 0$. These cutoffs are: the plasma frequency, $\nu_p = \sqrt{(N_{tot} e^2/\pi m)}$ for the ordinary mode (o-mode); and $\nu_x = \nu_b/2 + (\nu_p^2 + \nu_b^2/4)^{1/2}$ for the extraordinary mode (x-mode). The electron gyrofrequency is $\nu_b = eB/(2\pi mc)$, and N_{tot} is the plasma density, including non-radiating particles. The θ-polarization coefficient, a_θ, and index of refraction are given by

$$a_{\theta\pm}(\nu, \theta) = \frac{-2\nu(\nu_p^2 - \nu^2)\cos\theta}{-\nu^2\nu_b \sin^2\theta \pm \left[\nu^4\nu_b^2 \sin^4\theta + 4\nu^2(\nu_p^2 - \nu^2)^2 \cos^2\theta\right]^{1/2}} \qquad (4.6)$$

$$n_\pm^2(\theta) = 1 + \frac{2\nu_p^2(\nu_p^2 - \nu^2)}{\pm \left[\nu^4\nu_b^4 \sin^4\theta + 4\nu^2\nu_b^2(\nu_p^2 - \nu^2)^2 \cos^2\theta\right]^{1/2} - 2\nu^2(\nu_p^2 - \nu^2) - \nu^2\nu_b^2 \sin^2\theta} \, .$$
$$(4.7)$$

Note that, by not restricting n to be unity, the effects of Razin suppression at low frequencies are included.

Because of the presence of the Dirac delta function in equation (4.5), one of the integrals can be done analytically. For $\theta \neq \pi/2$, the resonance condition eliminates the integral over $d(\cos\phi)$, giving us:

$$j_\pm(\nu,\theta) = \frac{4\pi^2 e^2 \nu N}{|\cos\theta|\,c}\frac{1}{(1+a_{\theta\pm}^2)}\int_1^\infty \left\{ d\gamma \sum_{s_{min}}^{s_{max}} f(\gamma,\phi_s)\beta^{-1} \times \right.$$

$$\left. \left[a_{\theta\pm}\left(\frac{\cot\theta}{n_\pm} - \beta\frac{\cos\phi_s}{\sin\theta}\right)J_s(x_s) - \beta\sin\phi_s\, J_s'(x_s)\right]^2\right\} \qquad (4.8)$$

$$\kappa_\pm(\nu,\theta) = \frac{4\pi^2 e^2 N}{mc\nu\,|\cos\theta|}\frac{1}{n_\pm(1+a_{\theta\pm}^2)}\int_1^\infty d\gamma \sum_{s_{min}}^{s_{max}}\beta^{-1}\times$$

$$\left[-\beta\gamma^2\frac{\partial}{\partial\gamma}\left(\frac{f(\gamma,\phi)}{\beta\gamma^2}\right) + \frac{n_\pm\beta\cos\theta - \cos\phi}{\beta^2\gamma\sin\phi}\frac{\partial}{\partial\phi}f(\gamma,\phi)\right]_{\phi=\phi_s}\times$$

$$\left[a_{\theta\pm}\left(\frac{\cot\theta}{n_\pm} - \beta\frac{\cos\phi_s}{\sin\theta}\right)J_s(x_s) - \beta\sin\phi_s\,J_s'(x_s)\right]^2 , \qquad (4.9)$$

where

$$\cos\phi_s = \frac{1 - s\nu_b/\gamma\nu}{n_\pm\beta\cos\theta}, \qquad x_s = \frac{sn_\pm\beta\sin\theta\sin\phi_s}{1 - n_\pm\beta\cos\theta\cos\phi_s},$$

$$s_{min} = 1 + \text{Integer}\left[\frac{\gamma\nu}{\nu_b}(1 - n_\pm\beta\cos\theta)\right], \quad \text{and} \quad s_{max} = \text{Integer}\left[\frac{\gamma\nu}{\nu_b}(1 + n_\pm\beta\cos\theta)\right].$$

Note that $J_s'(x) = \frac{1}{2}[J_{s-1}(x) - J_{s+1}(x)]$.

An alternative approach is used to computing j and κ that allows the summation over s to be taken outside of the integral. The expressions for j and κ are the same as above, but the integration over γ is from γ_1 to γ_2 and the summation is from a minimum value of s to $s = \infty$:

$$s > \left(\frac{\nu}{\nu_b}\right)(1 - n_\pm^2\cos^2\theta)^{1/2} \qquad (4.10)$$

$$\gamma_{1(2)} = \frac{(s\nu_b/\nu)^2 + n_\pm^2\cos^2\theta}{(s\nu_b/\nu) + (-)n_\pm\,|\cos\theta|\,\left[(s\nu_b/\nu)^2 + n_\pm^2\cos^2\theta - 1\right]^{1/2}}. \qquad (4.11)$$

When $\theta = \pi/2$ we use the δ-function to integrate over γ, and obtain the following expressions for j and κ:

$$j_\pm\left(\nu,\frac{\pi}{2}\right) = \frac{4\pi^2 e^2 N}{c}\nu_b n_\pm \sum_{s=1}^\infty \beta_s^2 \int_{-1}^1 d(\cos\phi)\, f(\gamma_s,\phi)Y_\pm(\phi), \qquad (4.12)$$

$$\kappa_\pm\left(\nu,\frac{\pi}{2}\right) = \frac{4\pi^2 e^2 N}{mc\nu^2}\nu_b \sum_{s=1}^\infty \beta_s^2 \int_{-1}^1 d(\cos\phi)\, Y_\pm(\phi)\times$$

$$\left[-\beta\gamma^2\frac{\partial}{\partial\gamma}\left(\frac{f(\gamma,\phi)}{\beta\gamma^2}\right) - \frac{\cos\phi}{\beta^2\gamma\sin\phi}\frac{\partial}{\partial\phi}f(\gamma,\phi)\right]_{\gamma=\gamma_s,\beta=\beta_s}, \qquad (4.13)$$

where $Y_+(\phi) = [J_s(x_s)]^2\cos^2\phi$, $Y_-(\phi) = [J_s'(x_s)]^2\sin^2\phi$, $\gamma_s = s\nu_b/\nu$, $\beta_s = (1 - \gamma_s^{-2})^{1/2}$, and $x_s = s\beta_s n_\pm\sin\phi$.

4.2.2 GYROSYNCHROTRON CALCULATIONS

The above formulae are valid for the general distribution function $f(\gamma, \phi)$. We are primarily interested in thermal *vs* nonthermal effects, and so to gain a certain measure of simplicity, I shall discard any ϕ-dependence in f. I therefore use the isotropic bulk thermal distribution with a power-law tail of §2.3.

For the remainder of this chapter, I will refer to the distribution function (2.53) as a "TNT" (Thermal/NonThermal) distribution function, and a spectrum generated by such a distribution function I will call a TNT spectrum. Similarly, distribution functions and spectra based on only the first or second term of equation (2.53) I shall refer to as of type "TH" or "NT" respectively. As discussed repeatedly throughout this dissertation, the physical distribution function which is expected to be found in solar flares is a single, unified, smooth distribution of momenta, reflecting cotemporal heating and particle acceleration. The separation of such a function into separate thermal and nonthermal parts as is done here (eqn [2.53]), is a mathematical, and especially an analytical, convenience.

I have used a numerical code based on equations (4.1) and (4.5) through (4.11), allowing for Bessel functions to be calculated out to order 1,050 as needed. This is sufficient to allow calculation of gyrosynchrotron spectra, with a 1% accuracy, from the plasma cutoff frequency out to about the 35th harmonic of the electron gy-rofrequency. Each spectrum in practice runs from $1.001\nu_p$ to $33\nu_b$. I will show that the most interesting phenomena occur at the lower harmonics ($s < 10$) and thus the code is quite inclusive. The integrals are performed via the Gaussian Quadrature method, allowing the use of up to 256 points for estimating the value of the integral. If the desired accuracy cannot be achieved, the code uses the cautious, adaptive Romberg extrapolation method, repeatedly subdividing the interval between the limits of integration, until the change in error estimate is within the error requirements.

Into this code I insert the model distribution function, equation (2.53) (eqns [2.49] through [2.54]). I allow the Lorentz factor γ to range from very close to one out to $\gamma = 10$. We cannot allow $\gamma = 1$ because equations (4.8) and (4.9) are singular for particles at rest. I do however include energies much less than thermal. Particles having energies much in excess of 1 MeV contribute negligible amounts to the radiation being studied. I have found that lowering the high-energy cutoff from $\gamma = 10$ has no effect on the resulting spectra until γ_{max} reaches $\sim 2.5 - 3$, when it starts to affect the higher harmonics in the optically thin part of the spectrum. Our allowed range of γ is thus quite inclusive. I have found excellent agreement with Ramaty (1969) for the NT case.

In order to compare with observations, I choose a depth, D, for the radiating source and assign the source an effective area A. This allows the radiation intensity to be computed in solar flux units (1 sfu = 10^{-19}erg cm^{-2} sec^{-1} Hz^{-1}) for each polarization mode, by multiplying equation (4.1) by $10^{19}A/(1 \, AU)^2$.

There are eight necessary input parameters for computing a spectrum: T and N_{th} which characterize the thermal contribution to the distribution; ϵ and δ which characterize the nonthermal component; the magnetic field strength B, source depth D, and area A, which characterize the emitting region in which the single TNT distribution resides; and the viewing angle θ, between the wave vector and the

magnetic field direction, characterizing our orientation with respect to the source region.

Three complete spectra can be calculated for each set of input parameters. The spectra are based separately on equations (2.53), (2.50), and (2.49), i.e. spectra of type TNT, TH, and NT respectively. This allows us to assess the relative contributions of thermal and nonthermal particles at each point in a TNT spectrum.

The individual harmonics of both the emission and absorption coefficients can be separated out, in each of the two polarization modes, for all three types of spectra.

4.3 CURRENT SHEETS AND MICROWAVES

The relationship of the microwave radiation to current sheets is both simpler and more complex than that of the hard X-rays. This is because the gyrosynchrotron radiation is not expected to arise in the current sheets themselves. Rather, the microwave-emitting electrons are expected be thermal electrons in the heated ambient plasma surrounding the current sheets, and nonthermal electrons scattered *out* of the current sheets and *into* the ambient plasma.

The reason for not considering the current sheets as the major sources of the microwave radiation, is because the magnetic field is either absent, or parallel to $\vec{E}$, as discussed in §2.1. Since gyrosynchrotron emission depends on the electron's perpendicular component of velocity with respect to the magnetic field, the emission is either absent ($\vec{B} = 0$), or generated by thermal velocities only, since all of the nonthermal energy gained by an electron is directed *along* the magnetic field.

Although the thermal plasma has none of the complications of a thermal current (§2.2), the mechanism by which nonthermal electrons are scattered out of the current sheets is poorly understood. It is implicit that Coulomb scattering cannot be responsible, because the runaway electrons are nearly collisionless with respect to Coulomb collisions. Thus some turbulence or other current sheet instabilities must be present in order to provide the required pitch angle scattering. This is a subject for future research (§5.2).

The approach taken here to modeling the microwaves is therefore largely descriptive, employing a spectral index δ, and using ϵ primarily as a low-energy cutoff parameter. This is in contrast to the treatment given the hard X-rays in the last chapter, in which more physical parameters, such as current sheet length and electric field strength, were used. The choice of $\mathcal{E}_{cr}$ (i.e. ϵ) for the low energy cutoff to the nonthermal portion of the electron distribution function, reflects the fact that that electrons within the current sheets having $\mathcal{E} < \mathcal{E}_{cr}$ serve to primarily heat the plasma, whereas those with $\mathcal{E} > \mathcal{E}_{cr}$ are the nonthermally accelerated particles. It is possible to still interpret ϵ as the dimensionless electric field strength. The spectral index δ, however, will be a complicated function of electric field strength, current sheet length, and scattering mechanism (cf. Figs 2.3 and 2.4).
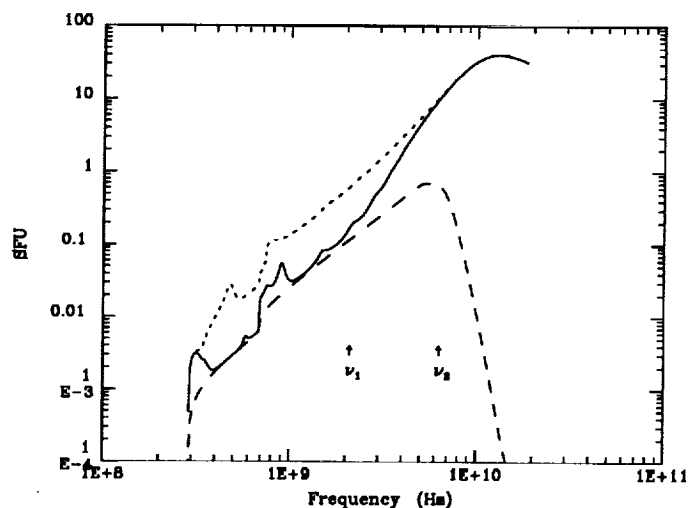
Figure 4.1: A typical TNT gyrosynchrotron spectrum as discussed in the text. Our plotting convention for this and all figures, unless explicitly stated otherwise, is: solid line = TNT spectrum; short dashed = NT; long dashed = TH. The transition frequencies are near ν_1 and ν_2. The input parameters are: $T = 2 \times 10^8\,$K, $N_{th} = 10^9\,$cm^{-3}, $\delta = 3$, $\epsilon = 0.05$, $B = 200\,$G, $D = 10^8\,$cm, $\theta = 45°$, $A = D^2$.

4.4 THEORETICAL MICROWAVE SPECTRA

4.4.1 GENERAL RESULTS

The spectrum of Figure 4.1 shows many of the features typically seen. The plotting convention, consistent with that of §3.3 and §3.4 is: the solid line is the calculated TNT spectrum, the short dashed line is NT, and the long dashed line is TH. The input parameters are: $T = 2 \times 10^8$K; $N_{th} = 10^9$cm^{-3}; $\delta = 3.0$; $\epsilon = 0.05$; $B = 200$G; $D = 10^8$cm; $A = 10^{16}$cm^2; $\theta = 45°$. Figure 4.2 shows the first six harmonics of emissivity in each polarization mode, using the same plotting convention, with the x-axis now being harmonic number. Figure 4.2(a) shows the ordinary mode ($s = 1 - 6$) and Figure 4.2(b) shows the extraordinary mode ($s = 2 - 7$). Harmonics of the absorption coefficient are qualitatively very similar. The polarization is shown as the solid line in Figure 4.10.

I first point out some general features shared, to a greater or lesser extent, by all spectra of the TNT type.

1. At the lowest frequencies, the TNT spectrum closely follows a spectrum produced by purely thermal electrons, except in certain wavebands where the TNT spectrum can be enhanced over the TH spectrum.

2. At the highest frequencies, the TNT spectrum is indistinguishable from a purely NT spectrum, i.e. the bulk thermal population does not contribute to the highest energy radiation.

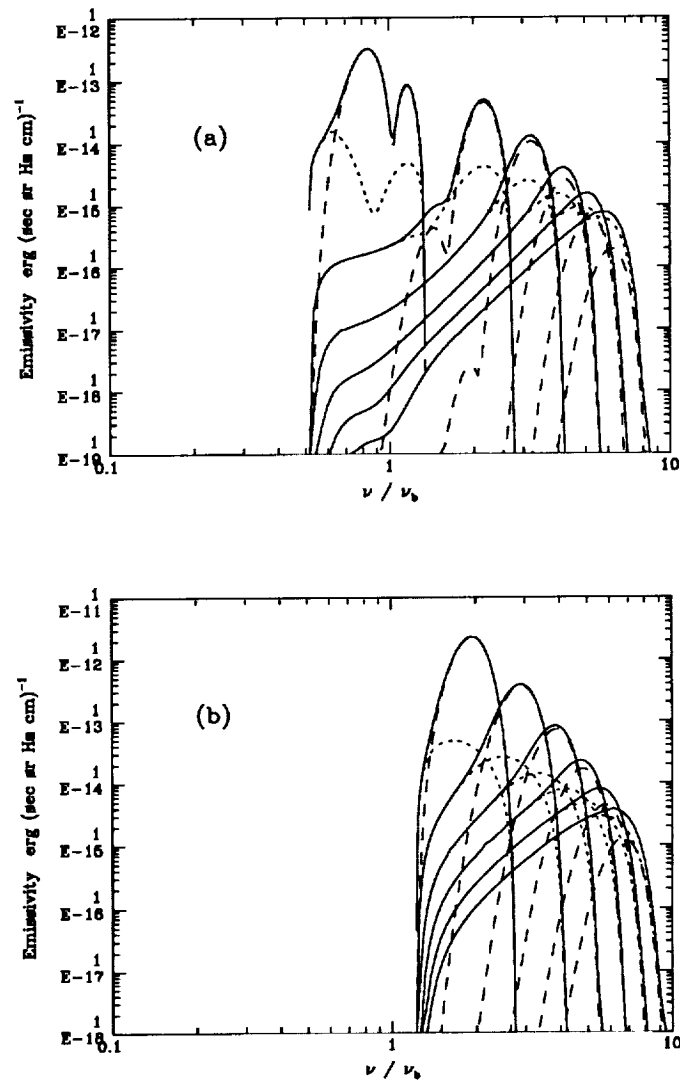3. The transition between these two regimes is characterized by two frequencies,

Figure 4.2: The first six harmonics of the emissivity for the spectrum of Figure 4.1, using the same plotting convention. The x-axis is now harmonic number. (a) Ordinary-Mode. (b) Extraordinary-Mode.

designated ν_1 and ν_2. Their approximate locations are shown on Figure 4.1. In the region between these two frequencies the TNT spectrum can have a steep positive slope.

All of these features are understood by noting that the expressions for the emission and absorption coefficients, equations (4.3) and (4.4) (or eqs. [4.8] and [4.9]), are linear in f, which itself is linear in f_{th} and f_{nt}. In other words the radiative transfer equation (4.1) becomes

$$I(\nu, \theta) = \frac{j_{th} + j_{nt}}{\kappa_{th} + \kappa_{nt}} [1 - \exp(-(\kappa_{th} + \kappa_{nt})D)] \quad \text{ergs(sec sterad Hz cm}^2)^{-1} \quad (4.14)$$

for each polarization mode.

This additivity is clearly seen in Figures 4.2(a) and 4.2(b). The overall intensity spectrum in each polarization is determined, at each frequency, by whichever component (TH or NT) is dominating in each of emission and absorption at that frequency.

For example, the lower transition frequency, ν_1, is that at which the intensity of the TNT spectrum begins to exceed that of the TH spectrum, neglecting the enhancements. At frequencies below ν_1 thermal emission and absorption dominate; that is, we are in the Rayleigh-Jeans regime and the slope on a log(Flux Density) vs log(Frequency) plot is 2. Nonthermal radiation is completely suppressed by the thermal plasma, again neglecting the enhancements.

At frequencies near ν_1 the nonthermal emissivity begins to contribute, although absorption is still dominated by the thermal electrons. Above ν_1 the nonthermal emissivity continues to grow relative to the thermal, eventually dominating completely at some frequency between ν_1 and ν_2.

Similarly, as the frequency is increased to approach the upper transition frequency ν_2, thermal absorption contributes less and less relative to that due to the nonthermal electrons. Since nonthermal emission is already dominating thermal emission, above ν_2 the spectrum is produced completely by nonthermal processes.

Between ν_1 and ν_2 the interesting situation arises in which the nonthermal particles are emitting more radiation than their thermal counterparts ($j_{nt} > j_{th}$), but the thermal particles are able to absorb much more of it than nonthermal self-absorption alone can account for. This additional thermal absorption of nonthermal radiation explains the steep slope seen in this region of the spectrum. In Figure 4.1, the slope between 2.5 and 5.5 GHz is ~ 4.3. Optically thick TNT slopes as steep as 7 have been seen in the course of this study, and it is likely that steeper slopes are possible. Note, as in Figure 4.3(b) below, that although steep slopes are naturally accounted for in this model, they are not inevitable, especially at very high temperatures.

The index of refraction for the plasma of Figure 4.2 is ~ 0.8 at 4×10^8Hz, and decreases rapidly for lower frequencies. This is the regime of Razin suppression, close to the plasma frequency cutoff.

Some additional discussion of point 1 above is now in order, the enhancements mentioned there being of prime observational importance. The lowest harmonics in a gyrosynchrotron spectrum do not overlap and blend as much as the higher ones, as can be seen in Figures 4.2(a) and 4.2(b). This is especially evident for thermal radiation, and the harmonics become still narrower for high viewing angles. The low harmonics of a nonthermal spectrum are broader, since an energetic

electron resonates with a Doppler-shifted gyrofrequency, ν_b/γ. The abundance of high energy electrons in a power-law distribution effectively creates a low-frequency broadening of each harmonic in the NT spectrum. As discussed above and shown in Figure 4.2, for $\nu < \nu_1$ the NT harmonics will have lower peak intensities than the TH harmonics — the spectrum is in the Rayleigh-Jeans regime. Nevertheless, the Doppler broadened NT harmonics can contribute in the frequency bands between the TH harmonics. Within these bands, not only does the NT emissivity exceed the TH, but the TH absorption is also too low to suppress the NT radiation. It is this limited NT contribution, *between* the TH harmonics, which produces the enhancements seen in the theoretical spectra. Since TH harmonics become narrower with either decreasing temperature or increasing viewing angle, it is evident that these NT enhancements can occur between any of the higher TH harmonics that are not sufficiently blended together (cf. Figures 4.3(a) and 4.9 below).

4.4.2 VARIATIONS WITH PARAMETERS

Figures 4.3 – 4.9 show how a basic TNT microwave spectrum (shown in the figures as a dot-dash line), similar to that of Figure 4.1, will typically vary as each of the input parameters is varied in turn. I shall discuss each of them, but first I must point out that these displayed variations, although covering a wide range of values of the parameters, are still somewhat limited. In effect I have taken seven mutually orthogonal excursions from a single point in 7-dimensional parameter space. Nevertheless, the general trends depicted will certainly hold throughout much of parameter space.

I will use the following notation in this discussion: I_{peak} is the intensity at ν_{peak}, the peak frequency. RJ refers to the the low-frequency (Rayleigh-Jeans, thermal) portion of the spectrum, having $\nu < \nu_1$, whether or not enhancements are present. PC refers to the Primary Component (in the nomenclature of SGH1 and SGH2), i.e. all frequencies $\nu > \nu_1$. The enhancements that appear on the optically thick side I will designate H-n, with n = 1, 2, etc. H-1 will always refer to the o-mode nonthermal enhancement below the gyrofrequency ($\nu_b = 1.12 \times 10^9$ Hz for the basic spectrum). Recall that these features are *not* harmonics, but rather are produced between the thermal harmonics. In §4.5 I will identify one or more of the H-n with the secondary components of Stäli, Gary, and Hurford (SGH2).

I do not display variations with area, A, since this factor is a premultiplier and thus simply raises or lowers the intensity of the spectrum *in toto*, leaving its shape unaffected.

The basic spectrum which is varied has these input parameters: $T = 7 \times 10^7$ K; $N_{th} = 10^9$ cm^{-3}; $\delta = 4.0$; $\epsilon = 0.05$; $B = 400$ G; $D = 10^8$ cm; $\theta = 45°$; $A = D^2 = 10^{16}$ cm^2. Note that the vertical scales of Figures 4.4 – 4.10 may vary.

TEMPERATURE, T

Figures 4.3(a) and 4.3(b) show that as the temperature rises, the TNT spectrum varies in four major ways: (1) The underlying thermal spectrum is raised in intensity (and shifts to a slightly higher peak frequency). This shifts the RJ part of the TNT spectrum upward in intensity. (2) I_{peak} increases. (3) ν_{peak} moves to
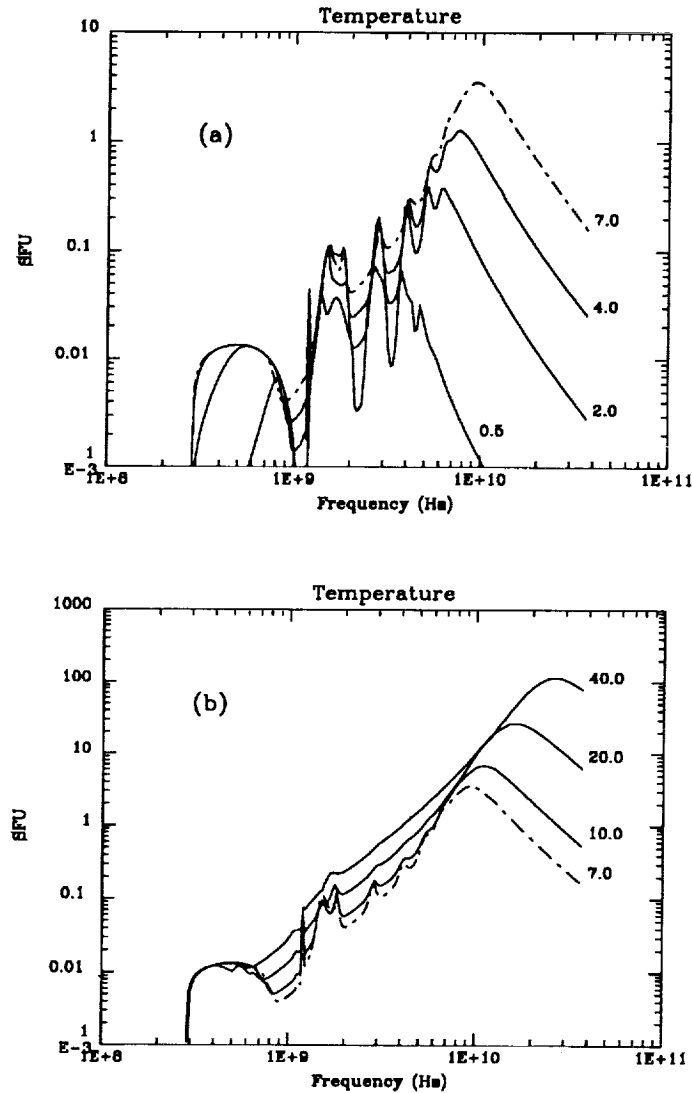
Figure 4.3: Variations with temperature of our basic TNT spectrum (dot-dash line). The basic spectrum has input parameters: $T = 7 \times 10^7 \, \text{K}$, $N_{th} = 10^9 \, \text{cm}^{-3}$, $\delta = 4.0$, $\epsilon = 0.05$, $B = 400 \, \text{G}$, $D = 10^8 \, \text{cm}$, $\theta = 45°$, $A = 10^{16} \, \text{cm}^2$). (a) $5 \times 10^6 \, \text{K} < T < 7 \times 10^7 \, \text{K}$. (b) $7 \times 10^7 \, \text{K} < T < 4 \times 10^8 \, \text{K}$. Note the different vertical scales in (a) and (b). The spectra are labelled in units of $10^7 \, \text{K}$.

higher frequencies. (4) The H-n features become less prominent due to the increased Doppler-broadening of the thermal harmonics. At the highest temperatures, the optically thick spectrum is quite smooth, changing character gradually from classic thermal (slope ~ 2) to nonthermal (slope ~ 3) (Dulk and Marsh 1982; SGH1). At intermediate temperatures, the H-n appear and the transition is more abrupt, having an optically thick slope > 3. As the temperature is lowered, the H-n become more apparent, due to the narrowing of the thermal harmonics, i.e. the wavebands between the thermal harmonics are wider.

DENSITY, N_{th}

Figure 4.4 shows variations with density of the basic TNT spectrum. The main changes as the density increases are: (1) The plasma frequency cutoff moves to higher frequencies, reaching 1 GHz at $N_{th} \sim 10^{10}\,\mathrm{cm}^{-3}$. The total number of thermal and nonthermal particles increases since $N_{nt} \propto N_{th}$, all else remaining unchanged (eq. [2.52]). Thus (2) I_{peak} increases relative to RJ, and (3) ν_{peak} increases, both resulting from the increasing optical depth of the source. (4) As the plasma frequency increases, the H-n structures are successively lost below the cutoff. As H-n is lost, H-(n+1) is enhanced.

SPECTRAL INDEX, δ

Hardening the spectral index increases the nonthermal nature of the TNT spectrum (Figure 4.5). Specifically, (1) I_{peak} increases dramatically with respect to RJ; (2) ν_{peak} increases; (3) The H-n features become increasingly pronounced, consistent with our discussion at the end of §4.4.1; (4) The lower transition frequency ν_1 is shifted downward, i.e. the TNT spectrum departs from TH sooner. (5) The width of the PC increases for two reasons. As the NT contribution increases, more of the optically thick spectrum is at frequencies above ν_2, and has a slope of ~ 3 (Dulk and Marsh 1982; SGH1), whereas the slope between ν_1 and ν_2 is steeper than this. The optically thin slope flattens with harder δ which further widens the PC.

The dashed line in Figure 4.5 is the associated purely thermal spectrum, and is closely approached by $\delta = 8$.

LOW-ENERGY CUTOFF, ϵ

We see in Figure 4.6 that as ϵ rises, i.e. as the nonthermal tail "climbs up" the Maxwellian to lower energies, the dominant changes are (1) to the PC which increases in intensity relative to RJ, and (2) to the H-n which also rise relative to RJ, consistent with our previous discussion. The PC drifts slowly to higher ν_{peak}. Decreasing ϵ below what is shown renders the TNT spectrum indistinguishable from the associated TH spectrum (dashed line), until at some very low intensity level the optically thin thermal slope of $\sim 8 - 10$ will change to $\sim 1.2 - .9\delta$ (§4.5.1), when the nonthermal particles are finally able to contribute to the radiation.
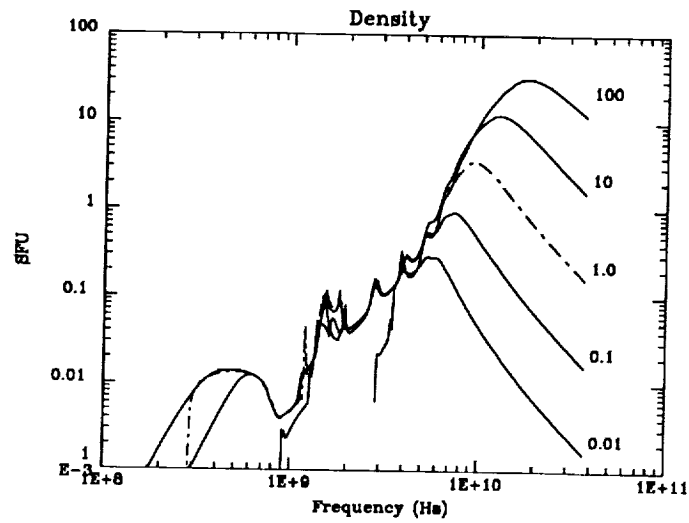
Figure   4.4:   Variations
with density of our basic spectrum. Here, $10^7\,\mathrm{cm}^{-3} < N_{th} < 10^{11}\,\mathrm{cm}^{-3}$. The spectra
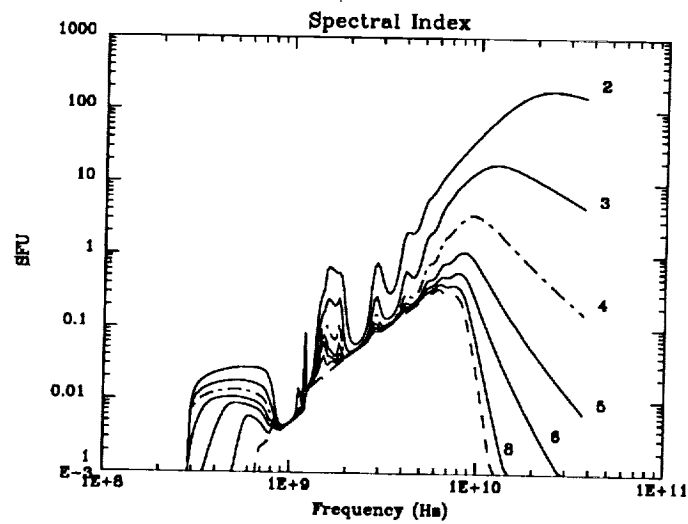are labelled in units of $10^9\,\mathrm{cm}^{-3}$.

Figure 4.5: Variations with electron spectral index $2 < \delta < 8$. The dashed line is the
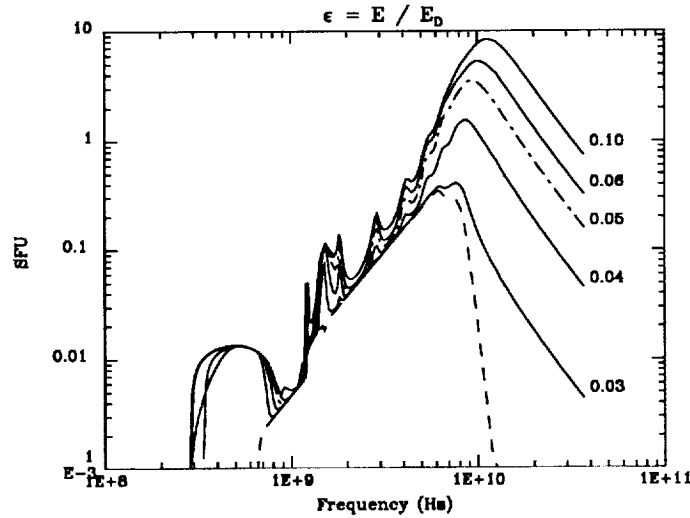associated TH spectrum.

Figure 4.6: Variations with nonthermal parameter, $0.03 < \epsilon < 0.1$. The dashed line is the asociated TH spectrum.

MAGNETIC FIELD, *B*

The intensity of gyrosynchrotron radiation is very sensitive to magnetic field strength, increasing greatly with B. To compensate for this, the three spectra in Figure 4.7 have been multiplied by $400/B$ for clarity. Increasing the magnetic field strength from B_1 to B_2 also translates any spectral feature to a higher frequency. This effect is nearly linear and the frequency translation can often be approximated by a factor of $\sim B_2/B_1$, since a given feature is found near a particular multiple of the gyrofrequency $\nu_b \sim 2.8 \times 10^6 B$. This rough scaling of frequency with B holds as long as the feature at the lower field strength is not too close to ν_p, the plasma frequency.

SOURCE DEPTH, *D*

Figure 4.8 shows the change with depth. Increasing the source depth is commensurate with increasing its optical depth, since the total number of particles along the line of sight increases. Thus we see the PC rise in intensity and shift to higher ν_{peak}. The H-n are unaffected over a wide range of source depths, being reduced for the smallest D's.
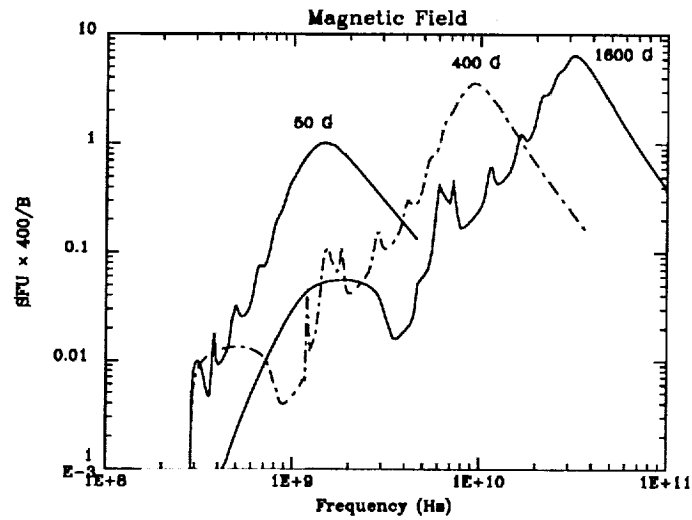
Figure 4.7: Variations with magnetic field strength $50\,\mathrm{G} < B < 1600\,\mathrm{G}$. Note that the vertical scale is different for each of the three displayed spectra.
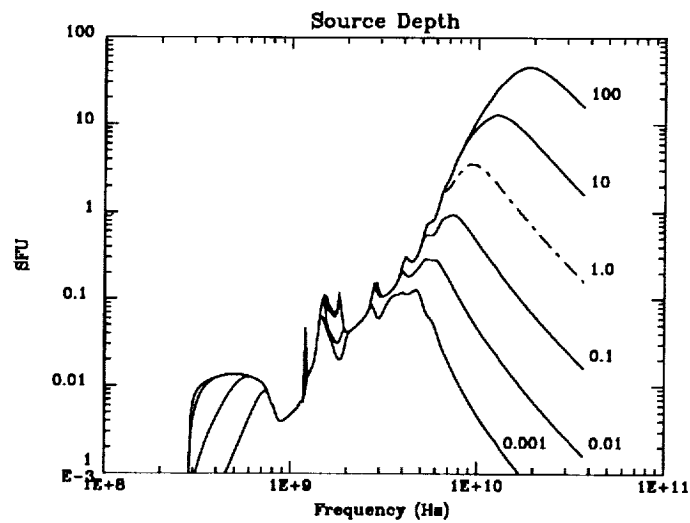

Figure 4.8: Variations with source depth, $10^5\,\mathrm{cm} < D < 10^{10}\,\mathrm{cm}$. The spectra are labelled in units of $10^8\,\mathrm{cm}$.
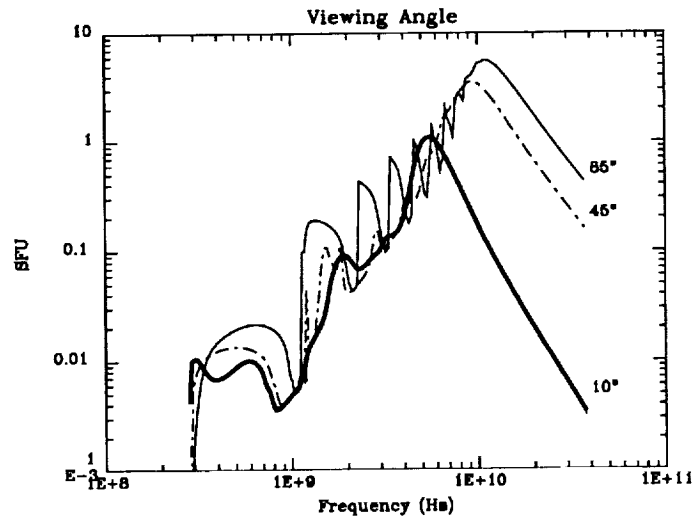
Figure 4.9: Variations with observation angle between the line of sight and the magnetic field, $10° < \theta < 85°$. The bold line for $\theta = 10°$ is for clarity.

OBSERVATION ANGLE, θ

As is known, the harmonic structure of gyrosynchrotron radiation is much more pronounced when viewed at high angles to the magnetic field (cf. Takakura 1960; Takakura and Scalise 1970). This results from all harmonics having both a greater contribution to the spectrum, and a narrower bandwidth. Of course the nonthermal harmonics are still Doppler broadened compared to the thermal harmonics.

The observed consequences are that I_{peak} increases and shifts to higher ν_{peak}, while the individual enhancements become much more apparent. This is borne out in Figure 4.9. In addition, I find that at low angles, the PC narrows and can become quite sharply peaked.

4.4.3 POLARIZATION

In Figure 4.10 I show the fractional polarization

$$\Pi = \frac{I_+ - I_-}{I_+ + I_-} \tag{4.15}$$

for the TNT spectrum of Figure 4.1 (solid line) as well as for the basic spectrum (dot-dashed line). These polarization characteristics are typical for TNT spectra in general: (1) The optically thin emission is x-mode polarized, and can exceed 50%; (2) Neglecting enhancements, the average optically thick polarization is $\sim 5 - 25\%$ in the o-mode; (3) The o-mode polarization of the enhancements can exceed 50%; (3) Where pure thermal emission occurs between the H-n, it is unpolarized. (4) Below the x-mode cutoff, all of the emission is, of course, o-mode. These results are
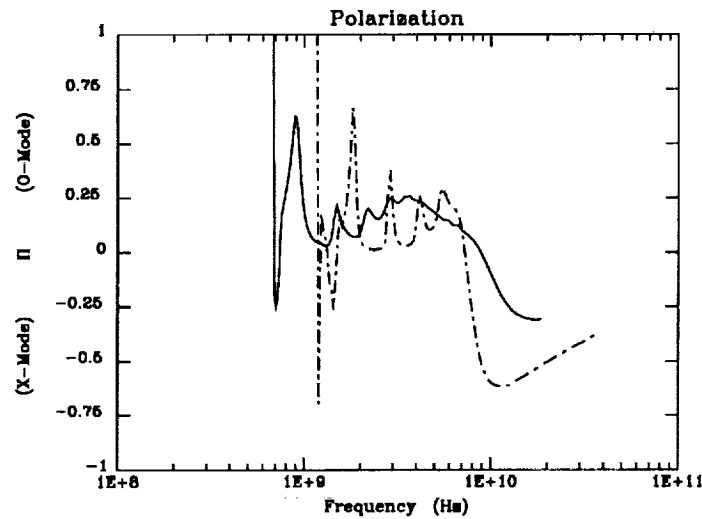
Figure 4.10: The fractional polarization (Eq. [4.15]) for the TNT spectrum of Figure 4.1 (solid line), and for the basic spectrum of Figures 4.3 through 4.9 (dot-dashed line). Below their respective x-mode cutoffs, the spectra are 100% o-mode polarized.

consistent with what is expected from one or the other of thermal and nonthermal particle distributions (Ramaty 1969).

I stress that the polarization discussed here is as it leaves a homogeneous source, with no consideration given to an intervening plasma. It is known that polarization can be reduced by propagation effects, and even reversed if the component of magnetic field along the line-of-sight goes to zero between the source and observer (Zheleznyakov 1970; Bandiera 1982). Bogod *et al.* (1990), and Brosius *et al.* (1991) provide observational examples of these effects. Caution is advised in drawing conclusions based on polarization data without an investigation of the intervening plasma, especially at the lower frequencies.

4.4.4 THE LOWEST HARMONIC

The lowest harmonic which contributes to a spectrum has an interesting structure of its own. It is invariably double-peaked, whether the gyrofrequency is above or below the plasma frequency. It is always o-mode (below the x-mode cutoff) and can be any harmonic of the gyrofrequency (it is $s = 1$ only for $\nu_p \leq \nu_b$). It is possible to observe this harmonic if it corresponds to $s \geq 3$ (cf. §4.5).

To understand this structure, we surmise from Figure 4.2 that the existence of twin peaks is independent of the particular electron distribution function used. This leads us to choose a δ-function distribution, $f \sim \delta(\gamma - \gamma_o)$, insertion of which into equation (4.8) for a single fixed harmonic $s = S$, leads us to the relatively simple

equation

$$j_{\pm} = \frac{4\pi^2 e^2 N}{|\cos\theta|} \frac{1}{c(1 + a_{\theta\pm}^2)} \frac{\nu}{\beta_o} \left[a_{\theta\pm} \left(\frac{\cot\theta}{n_{\pm}} - \beta_o \frac{\cos\phi_S}{\sin\theta} \right) J_S(x_S) - \beta_o \sin\phi_S J_S'(x_S) \right]^2.$$

(4.16)

In Figure 4.11 I plot the o-mode emissivity for $S = 1$ for various values of γ_o, where the different linetypes are used for clarity only and do not correspond to our usual plotting convention. Notice that higher energy electrons radiate at lower Doppler-shifted frequencies, as expected. The double-peaked structure is confirmed for the o-mode, and persists but is modified for higher S (not shown).

This structure is related to the variability with frequency of the θ-polarization coefficient, equation (4.6). When a_θ is set equal to a constant, the two peaks do not appear. Equation (4.6) for $a_{\theta\pm}$ is a monotonically decreasing function of frequency, but differs markedly in the two polarization modes. In the o-mode, $a_{\theta+}$ ranges from $\gg 1$ at the lowest frequencies, to asymptotically approach unity at high frequencies. On the other hand, $a_{\theta-}$ decreases only gradually, from 0 to -1 (in fact it is 0 only at the plasma frequency which is always below the x-mode cutoff [§4.2.1]). It is thus the changing interplay between the two terms in square brackets in equation (4.16) (and the analogous terms in eqns. (4.8) and (4.9)) which produces the observed structure in the o-mode harmonic. That is, at the higher frequencies within this harmonic, the two terms generate the usual rising and falling harmonic structure. As the frequency is decreased, however, at some point the increasing value of $a_{\theta+}$ gives additional weight to the first term so that it again dominates. Finally, at the
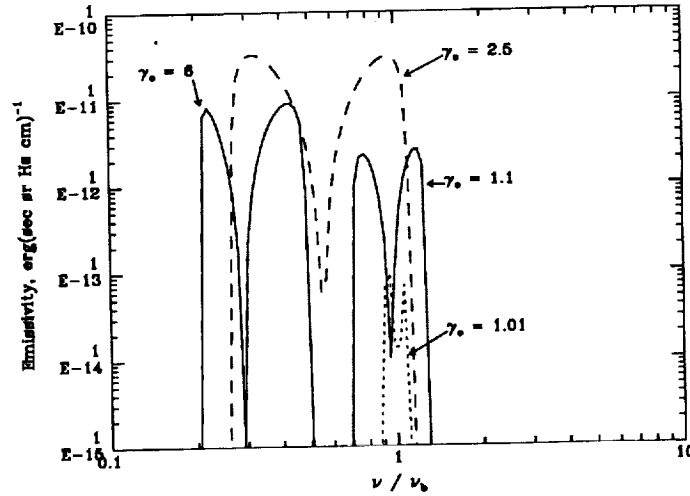

Figure 4.11: The first contributing harmonic (in this case $s = 1$) of the emissivity from a $\delta-$function electron distribution, as discussed in the text, for $\gamma_o = 1.01, 1.1, 2.5, 6$. In this figure the different line types are for clarity only and do not correspond to our usual plotting convention. The input was $N = 2 \times 10^9$ cm^{-3}, $B = 700$ G, and $\theta = 45°$.

lowest frequencies, either Razin suppression or a lack of energetic particles (as in a Maxwellian) cuts off this "anomalous" harmonic entirely. Though this effect can persist for higher harmonics (cf. Fig 4.2[a]), the fact that $a_{\theta+}$ is approaching unity means that, for the higher harmonics, it is less apparent (the first term in square brackets is not as heavily weighted). I remark that this o-mode structure has been noticed before (Tamor 1978), but the explanation of it was incorrect (Tamor 1979).

4.5 MODELING OBSERVED MICROWAVE SPECTRA

4.5.1 A "TYPICAL" SPECTRUM

I have tested this model against observations by fitting a "typical" spectrum from SGH1. Those authors state: "About 80% of the minor spectral components occur on the low frequency side of the main peak in the spectrum, i.e. at frequencies lower than the peak frequency." In Figure 4.12 I show my fit to such a spectrum (SGH1, their Fig. 2*d*). The deduced parameters are: $T = 7.6 \times 10^7$K; $N_{th} = 6 \times 10^9$cm^{-3}; $\delta = 4.5$; $\epsilon = 0.077$; $B = 340$ G; $D = 5.0 \times 10^6$cm; $A = 5.0 \times 10^{17}$cm^2; $\theta = 57°$.The reduced χ-squared statistic is 1.422, giving a χ-squared probability function of 99.4%.

It is seen that our fit is very good for $\nu \gtrsim 2$ GHz, and less acceptable at lower frequencies. This is to be expected, for the following reason. It is difficult for the first or second harmonics of gyrosynchrotron radiation to escape from the solar corona, because of the likelihood of their being reabsorbed as second and third harmonics of a weaker magnetic field. This effect is strongest for the gyrofrequency, and diminishes with successive harmonics. We thus expect that gyrosynchrotron radiation from a homogeneous source will provide a good fit only at frequencies $\nu \gtrsim 3\nu_b \sim 8.4 \times 10^6 B$ GHz, with B the deduced magnetic field strength. In other words, I generally expect the theoretical H-1 and H-2 enhancements to be largely unobservable, while the observed H-3 feature will be somewhat modified. This is consistent with what we see in Figure 4.12, where the "secondary component" near 2 GHz corresponds to H-3 ($3\nu_b = 2.8$ GHz). I have also fit the spectrum assuming this enhancement to be both H-2 and H-4, but the lowest χ_ν^2 results for H-3. At frequencies lower than $3\nu_b$, external absorption, other emission mechanisms, or source inhomogeneities may be important.

A major result of the TNT model is the natural production of low-frequency enhancements. The presence, both observationally and theoretically, of these features provides a powerful diagnostic for flare magnetic field strengths and plasma temperatures.

From the discussion at the end of §4.4.1, it follows that the dips in the spectrum between the enhancements mark the harmonics of the thermal gyrosynchrotron spectrum. The frequencies of these local minima are then related to the magnetic field by $\nu_{l.m.} \sim 2.8 \times 10^6 s B$ with s a positive integer. The separation in frequency between successive minima changes with the s chosen, and so observation of 2 or more such minima can rapidly lead to a determination of the field strength in the radiation-producing region, to within $\lesssim 10$ G. This is how the magnetic field strength was
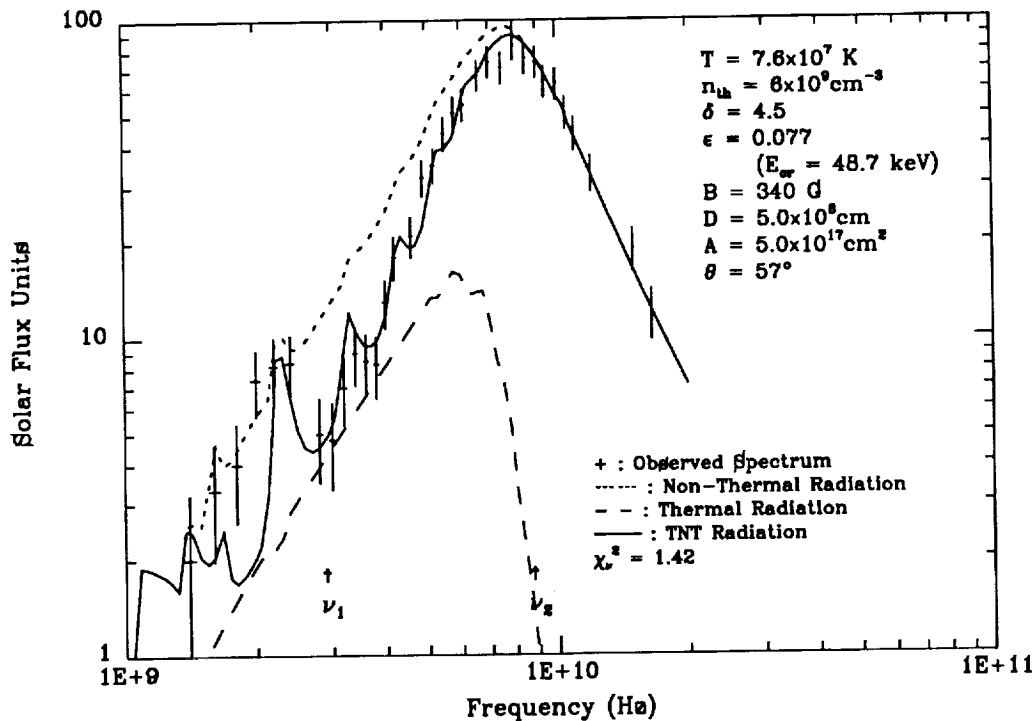
Figure 4.12: A theoretical fit to Fig. 2d of Stäli, Gary, and Hurford 1989. The flare occurred 1981 July 24. The emission is assumed to be entirely gyrosynchrotron radiation from a TNT distribution function. Our plotting convention of Figures 4.1 – 4.9 is used. This complex observed spectrum is well fit except at the lowest frequencies, as discussed in the text. The derived parameters are: $T = 7.6 \times 10^7$ K; $N_{th} = 6 \times 10^9$ cm^{-3}; $\delta = 4.5$; $\epsilon = 0.077$; $B = 340$ G; $D = 5.0 \times 10^6$ cm; $A = 5.0 \times 10^{17}$ cm^2; $\theta = 57°$.

deduced for the spectrum of Figure 4.12.

The intensity of the radiation at these local minima also provides a diagnostic for the temperature in the region. Deep minima imply low-intensity thermal emission and thus a low temperature (cf. Fig 4.3[a]). The converse applies to shallow minima (Fig 4.3[b]). Using the first observed minimum at or above $3\nu_b$ provides the best estimate for the temperature, since higher frequencies are increasingly influenced by the nonthermal particles. A comparison of the TH and TNT spectra in Figure 4.12 bears this out. The temperature deduced for Figure 4.12 is hotter than the typical flare soft X-ray plasma, and consistent with the superhot component seen in hard X-rays by Nitta, Kiplinger, and Kai (1989).

Since ν_{peak} often occurs near or above the 10th harmonic, the negative slope of the optically thin part of the spectrum provides a diagnostic for the nonthermal electron spectral index, through the empirical approximation (Slope) $\sim 1.22 - 0.9\delta$ (Dulk and Marsh, 1982). If brightness temperature is measured instead of flux density, the relation is: $(T_B \text{ Slope}) \sim -0.78 - 0.9\delta$. These expressions are approximately valid for $\delta < 5$ and $20° < \theta < 80°$. For θ near $20°$, the range of δ can be extended to ~ 7.

The presence of fine structure along the steep optically thick slope between ν_1 and ν_2 indicates that the higher order H-n structures are not completely blended. This in turn can provide a diagnostic for the viewing angle θ, to which these structures are very sensitive (cf. Figure 4.9).

The success of the eight parameter fit for a spectrum as complex as that of Figure 4.13 is encouraging. For instance, only one "primary" and one "secondary" component would require eight parameters for a two-triangle description: two peak intensities, two peak frequencies, and four associated slopes. I also point out that OVRO spectra sample up to 40 frequencies between 1 and 18 GHz (34 in Figure 4.13), a number significantly greater than our 8 fitting parameters.

In practice, the TNT model usually provides a *seven* parameter fit, because the optical depth is determined by the product ND, density entering independently only at the lowest frequencies (near ν_p).

As discussed above, the most easily determined parameters are magnetic field strength B, temperature T, and spectral index δ.

Having determined three parameters using gross features of the spectrum, one is faced with an iterative process for determining four more. ND determines in part both the peak frequency and the relative intensities of the main peak and enhancements. The *shapes* of the main peak and enhancements can be subtly influenced by ϵ, as well as their relative intensities and to some extent ν_{peak}. If some fine structure is seen on the steep, positive, optically-thick slope, the viewing angle θ can be determined very reliably for each iterative choice of ND and ϵ. The best-fit area A is uniquely determined for each combination of ND, ϵ, and θ. Having iteratively achieved an acceptable fit above $\sim 3\nu_b$, one can adjust N holding ND constant, to improve the fit at lower frequencies. This in turn may require a readjustment of θ since the enhancements and positive slope fine structure can be subtly affected by changes in N. As discussed above, however, achieving a "better fit" at frequencies below $\sim 3\nu_b$ is not necessarily the same as determining N to higher accuracy, since the role of external absorption and other emission mechanisms is unclear at these low frequencies.

Given our identification of the the enhancement near 2 GHz as H-3, I believe that

the parameters deduced for Figure 4.12 are each determined to within 10% accuracy, and some of them (B, δ, T, θ) to better than 5%. Because of the ambiguity in N and D mentioned above this accuracy applies only to the product ND.

It is interesting that the deduced value for ND implies, for coronal densities, a very small source depth — on the order of 100 km. When combined with the deduced area, one is led to the possibility that the observed gyrosynchrotron emission originates in a thin "disk" somewhere in the leg of a magnetic loop, rather than throughout the loop volume as generally supposed. In retrospect, this is quite reasonable for two related reasons. First, the converging magnetic field becomes stronger as the loop is traversed from its apex toward the chromosphere. Secondly, the converging B-field means that particles can mirror, which in turn increases their momentum perpendicular to the field (although recall that here I have used an isotropic pitch-angle distribution). Both effects increase the intensity of gyrosynchrotron emission, so one might expect to preferentially observe the lower portions of a loop during a burst. If we do in fact observe such a narrow emission region, this could help explain why the TNT model for a *homogeneous* source can work as well as it does.

4.5.2 THE PEAK FREQUENCY

It is known that the peak frequency of a microwave burst changes slowly if at all during the burst's evolution. This is in stark contrast to the predictions of the simpler models in which changes in such quantities as temperature, density, magnetic field strength, or viewing angle produce peak frequency shifts far in excess of those observed (SGH1). In addition, the enhancements are seen to rise and fall together with the main peak (SGH2).

It is beyond the scope of this paper to model any flare *in toto*, but Figures 4.3 – 4.9 indicate that the parameter ϵ is a likely candidate to explain the gross evolutionary changes observed in a flare, perhaps in concert with small changes in δ. Both the "primary" and "secondary" components vary in unison with ϵ, and ν_{peak} stays relatively fixed.

The case for ϵ can be made more plausible by recognizing that ν_{peak} is determined by the optical depth, i.e. absorption coefficient. This in turn depends on the *derivative* of f with respect to γ, and all ϵ-dependence in f can be factored out of the derivative and indeed out of the summation in equation (4.9). This is not true for any of T, δ, B, or θ, while density and source depth directly alter the optical depth by changing the number of particles along the integrated line of sight. As discussed previously (§§2.1, 4.3), ϵ is related to the electric field strength in the acceleration region, which is expected to be a naturally evolving physical quantity in a flare.

The constancy of ν_{peak} and the coevolution of the components could also be due to a changing source area which, as mentioned earlier, is a premultiplier. The area change would have to be independent of other physical quantities, however, so as not to alter the optical depth of the source. Microwave imaging at multiple frequencies will help resolve this point.

I note that the approximation for ν_{peak} (Dulk and Marsh 1982), within the range

of δ discussed above, must be ammended for this model by a factor of

$$\left(\frac{\mathcal{E}_{cr}}{10\,\mathrm{keV}}\right)^{-0.32+0.35\delta-0.03\delta^2} ,$$

since $\mathcal{E}_{cr}$ can be much higher than was assumed by those authors. This correction is valid for $\mathcal{E}_{cr}$ up to at least 150 keV.

4.6 MICROWAVE SUMMARY

In this chapter, I have presented a new approach to modeling solar microwave bursts, which provides new physical insight into high resolution microwave spectra. The model combines elements of the previously disparate thermal and nonthermal models, allowing both of these populations to coexist during a flare. This shifts our perspective from asking whether flare emissions are produced by thermal or by nonthermal particles, to asking how much of a contribution does each population make. The assumption of a thermal/nonthermal electron distribution is both physically reasonable and has important observational consequences.

For the large class of observed flares showing enhancements on the low-frequency side of the spectral peak, I find that this model can successfully address three observational challenges:

(1) The enhancements themselves are explained as nonthermal radiation produced between the lowest of the thermal harmonics. Within these wavebands the otherwise dominant thermal processes are incapable of suppressing the nonthermal emission.

(2) The appearance of steep slopes on the optically thick side of the spectrum is accounted for by the thermal absorption of nonthermally produced radiation.

(3) The relative constancy of the peak frequency throughout a burst, and the co-evolution of the low frequency enhancements, is made plausible if the major contributor to the evolution of the electron distribution is a changing electric field strength.

Physically, the TNT distribution function is placed within a plausible and internally consistent framework, by assuming the presence of current sheets in the flaring plasma. The current sheets provide both primary heating of the plasma, and nonthermal acceleration of particles.

I have demonstrated the applicability of this model by fitting an observed high resolution microwave spectrum. The sophistication of such present generation observations shows the limitations of simpler approaches. The approach presented here can be used to directly model such observations, and can provide us with a more unified perspective from which to study solar flares.

Chapter 5

SUMMARY, PROGNOSIS, AND CONCLUSIONS

5.1 SUMMARY

This dissertation has laid the foundation for a fundamentally new approach to thinking about and modelling solar flares. The *primum mobile* of this approach is the coexistence of thermal and nonthermal particles in the flaring plasma, and their joint contribution to the observed emission from a flare, particularly the hard X-rays and microwaves. The existence of such a thermal/nonthermal plasma reflects the physically reasonable assumption that both plasma heating and particle acceleration are integral parts of the flare phenomenon.

The physical cause of the heating and acceleration is proposed to be macroscopic DC electric currents (current sheets) in the solar atmosphere. This is consistent with the observation that flares are strongly associated with stressed, nonpotential, current-carrying magnetic fields. A fraction of the current-carrying particles are boosted to high energies through the runaway acceleration process, while the bulk of the current is subject to Joule dissipation, thereby heating the ambient plasma in which the current sheets are embedded.

The observed hard X-ray emission is then a combination of thermal bremsstrahlung, arising from the heated plasma, and nonthermal thick-target bremsstrahlung, arising from either some or all of the current-carrying particles being injected into the cooler, denser chromosphere. The observed microwave emission is gyrosynchrotron radiation, generated by the mildly relativistic electrons spiralling around magnetic field lines. This is *not* expected to be significant within the current sheets themselves, which are either coaligned with any magnetic field, or exist in magnetically neutral regions. Any nonthermal particles scattered out of the sheets will, however, have sufficient perpendicular momentum (with respect to the magnetic field) to produce this radiation, in conjunction with the already heated plasma into which they are scattered. The presence of such DC current structures in solar flares imparts both thermal and nonthermal characteristics to both the observed hard X-rays and microwaves. The proposed current sheets thus provide an internally consistent physical framework within which to study flares.

Two possible flare models incorporating current sheets were discussed, and more

are undoubtedly possible. One model involves a large current sheet in the solar corona, situated atop an arcade of magnetic loops (Fig 1.3). Runaway accelerated electrons are scattered out of the current sheet, to stream down the legs of the loops to the chromosphere, where they produce thick-target bremsstrahlung. On their way, these same particles could emit gyrosynchrotron radiation, together with the thermal plasma within the loops. In addition, the current sheet heats the coronal plasma at the top of the magnetic arcade. When the emission measure of this hot plasma becomes large enough, the thermal bremsstrahlung generated here becomes visible as the superhot thermal component of hard X-rays (Figs 3.8 and 3.9). The spatial separation of the thermal and nonthermal hard X-ray components in this model could be seen by a high resolution hard X-ray imager (§3.5).

The other model, only briefly discussed, involves $> 10^4$ oppositely-directed current sheets aligned with, and residing within, one or more magnetic loops in the solar corona. In this picture the currents would terminate in the denser, cooler chromosphere, and all of the current-carrying particles (drifting thermal *and* runaway accelerated) would generate thick-target hard X-ray bremsstrahlung. The currents would, of course, also heat the plasma throughout the loop, generating thermal hard X-ray bremsstrahlung. In addition, some of the accelerated electrons will be scattered out of the current sheets, into the surrounding plasma within the loop, giving this plasma a thermal/nonthermal character. It is this ambient plasma which is the source of the gyrosynchrotron microwave emission. In this model, the superhot thermal component of hard X-rays could, paradoxically, be produced by current-carrying (i.e. *nonthermal*) electrons, as well as by a thermal plasma. Which of them would dominate would depend on the heat transport properties of the plasma.

Electron distribution functions were obtained (Chapter 2) for thermal/nonthermal plasmas. Within current sheets (§2.2), there are runaway accelerated electrons (§2.2.1) and a drifting thermal population (§2.2.2). The ambient plasma, in which the current sheets are embedded, also has a thermal/nonthermal character (§2.3) due to the scattering of particles out of the current sheets.

Various of these distribution functions were used to calculate hard X-ray spectra (Chapter 3) and gyrosynchrotron microwave spectra (Chapter 4). For the hard X-rays, six physical input parameters are required for a spectrum, the same number as in the (less physical) conventional modeling done to date. These are: temperature and emission measure to characterize the thermal emission; electric field strength, current sheet length, and electron density in the current sheets, to characterize the nonthermal electrons; and thick-target area which characterizes the nonthermal source. The effect of each of these parameters on the resultant theoretical spectra was investigated (§3.3). The thermal/nonthermal approach was used to fit two observed spectra (§3.4). It was found that only five parameters are required in practice, and excellent results were obtained. The thermal/nonthermal approach was also employed to model two-ribbon flares imaged in hard X-rays (§3.5), and the importance of such future observations was emphasized.

For the microwave spectra (Chapter 4), it was found that previously unexplainable features could be naturally accounted for within the context of the thermal/nonthermal approach. In particular:

(1) Low frequency enhancements were seen to be nonthermal radiation produced in wavebands where otherwise dominating thermal processes could not suppress it;

(2) Steep positive slopes on the optically thick side of the spectrum were accounted for by the thermal absorption of nonthermally produced radiation;

(3) The coevolution of spectral features, and the relative constancy of the peak frequency throughout a flare, are made plausible if the major contributor to the evolution of the electron distribution function is a changing electric field strength.

Eight input parameters are required for a theoretical microwave spectrum, which was shown to be an acceptable number. These are: temperature and thermal electron density which characterize the thermal particles; low-energy cutoff and spectral index for the nonthermal particles; magnetic field strength, source depth and area, characterizing the source; and line of sight angle to the magnetic field, which characterizes our orientation to the source. Once again, the effect of each of these parameters on the resultant spectra was investigated (§4.4). Once again, an observed high resolution spectrum was fit using the thermal/nonthermal approach (§4.5) with excellent results.

5.2   LOOKING TO THE FUTURE

The ideas presented in the course of this dissertation show great promise for elucidating the physics underlying solar flares. There are many possible applications, extensions, and refinements of these ideas. I will now briefly discuss some of them.

The first, and most important, future task is to apply the thermal/nonthermal approach in detail to flares for which high resolution spectra exist in both hard X-rays and microwaves. No such data sets were in existence during the development of this approach. Now however, following the successful deployment of NASA's Gamma Ray Observatory satellite, it is hoped that spectra taken with the Burst And Transient Source Experiment (BATSE) modules will be of high enough quality to distinguish the superhot component in the hard X-rays. These will be the best spectra ever obtained with a scintillation type detector, reaching photon energies as low as 15 keV, with a full width at half maximum of 4 keV. In addition, in December of 1991, a cooled germanium detector (similar to that used for the observations in Figs 3.8 and 3.9) will be on a long-duration balloon flight in Antarctica. This detector goes down to 12 keV with FWHM of ~ 1 keV. If hard X-ray producing flares are seen at that time, and if they occur during the hours when Owens Valley Radio Observatory is observing the sun (1600 – 2400 UT), this will provide an unprecedented data set to which this approach can be applied.

The detailed modeling of such simultaneous observations will help us to uncover some of the physics underlying the flare phenomenon. Fitting observed high resolution spectra in both wavelength regimes, and following the evolution of these spectra throughout the course of a flare, can tell us many things. First and foremost, we can learn something about the physical link between the microwave-emitting and hard X-ray-emitting plasmas. Such a link has long been known to exist (see Figs 1.1 and 1.2), but its nature has never been satisfactorily elucidated. Using a parameterized form of equation (2.48), this connection can now be made.

Seeing how the various parameters evolve throughout a flare will give us much needed insight into flares. For example, one current popular notion is that nonthermal beams, entering the chromosphere, evaporate much of the chromospheric

C·2

material (cf. Tandberg-Hanssen and Emslie 1988). If the density of the microwave-emitting plasma is found to increase during a flare, this could be evidence that the runaways are indeed driving such an evaporation.

It was argued in §4.5 that a changing electric field strength may be the most important parameter for characterizing the evolution of a flare. If this proves to be true, then it may be possible to deduce the threshhold conditions necessary for the onset of a flare, after analyzing many flares in this manner.

We can also learn about heat transport within flares, since the microwave-emitting plasma outside of the current sheets can be no hotter than the current sheets which are heating it. Thus constrained, following the relationships between the hard X-ray and microwave temperatures and emission measures will tell us about the heating process itself.

The addition of observations in other wavelength regimes (e.g. soft X-rays of $1 - 10$ keV, and Hα) to the data set will provide still more information about energy and particle transport within flares, as well as helping further to constrain the parameters within the flare plasma.

In summary, the detailed modeling of several "typical" flares, using the thermal/nonthermal approach, will go far to improving our understanding of flares, and can provide insight as to how best to approach less well observed events (e.g. by knowing how various parameters typically evolve).

In order to get the most scientific return from the time invested in such modeling, the most accurate possible formalism must be used. Thus the results and corrections due to to MacNeice et al. (§2.4) must be extended to the regime of applicability to solar flares, and incorporated into the runaway electron distribution functions used.

A study of various current sheet instabilities is essential for gaining a deeper physical understanding. For example, in supposing the microwaves to be produced by energetic electrons scattered out of the current sheet, it is implicit that Coulomb scattering cannot be the scattering mechanism. This is because the runaway electrons are nearly collisionless with respect to Coulomb collisions. However, if the current drift velocity exceeds the threshold for a plasma instability, turbulence can be generated in the current sheet(s), greatly increasing the collision frequency of the nonthermal electrons (e.g. Holman 1985). Candidate instabilities for generating such "anomalous resistivity" are the ion acoustic, electrostatic ion cyclotron, lower hybrid drift, and anomalous Doppler resonance instabilities. Each of these should be examined for their relevance to solar flares.

Another role for current sheet instabilities in flares is the generation of very fast time structures. Millisecond spikes have been observed in both hard X-rays (Kiplinger, et al. 1984) and microwaves (Gary, Hurford, and Flees 1991). Such rapid fluctuations are likely to be caused by sudden disruptions of the heating and acceleration processes. The above mentioned instabilities could have a role in these disruptions, and in addition the two-stream instability (associated with the runaway electrons) and the tearing-mode instability (for sufficiently thin current sheets) may be important.

A study of the relevant time scales (growth rate, saturation, heating) for all of these instabilities could be compared with observed time scales (rise time, duration, fall time) for such spikes. It is hoped that one or two flares to be modeled as described above will exhibit such rapid time structures. In this case, a great deal

of information can be learned, both about the large scale (thermal/nonthermal) properties of the flare plasma, and the smaller-scale physics taking place in the current sheets. Thus a significant step will be taken toward realizing the goal of understanding the underlying physical processes in solar flares.

It is likely that the ideas contained in this dissertation have many applications to astrophysical objects other than the sun. Indeed, any system showing both strong magnetic field gradients (in either space or time) and particle acceleration, is likely to contain DC currents, and is thus amenable to a similar analysis. Such systems could include flare stars, close binary stars, accretion disks, neutron stars, galactic nuclei, and jets and lobes of radio galaxies and quasars.

5.3 CONCLUSION

The grand conclusion of this work may be summed up in one sentence: The thermal/nonthermal approach to solar flares, within the framework of DC electric field heating and acceleration, provides a unified, physically reasonable perspective from which to study the flare phenomenon.

It is now possible, in practice as well as in principle, to deduce the relative contributions of thermal and nonthermal processes to the radiation that we observe from flares. This has already allowed us to explain previously unexplainable phenomena, such as microwave spectral features and the presence of a superhot thermal hard X-ray component. It will, I hope, lead to yet other insights which can be glimpsed only dimly at present.

REFERENCES

Anderson, K. A., and Winckler, J. R. 1962, *J. Geophys. Res.*, **67**, 4103.

Bandiera, R. 1982, *Astr. Ap.*, **112**, 52.

Batchelor, D. A. 1989, *Ap. J.*, **340**, 607.

Batchelor, D. A. 1990, *Ap. J. Supp.*, **73**, 131.

Batchelor, D. A., Crannell, C. J., Wiehl, H. J., and Magun, A. 1985, *Ap. J.*, **295**, 258.

Benka, S. G., and Holman, G. D. 1991, *Ap. J.*, submitted.

Bevington, P. R. 1969, *Data Reduction and Error Analysis for the Physical Sciences* (New York: McGraw-Hill).

Bhattacharjee, A., and Wang, X. 1991, *Ap. J.*, **372**, 321.

Bogod, V. M., Korzhavin, A. N., Akhmedov, SH. B., Aurass, H., Hildebrandt, J., and Krüger, A. 1990, *Solar Phys.*, **129**, 351.

Book, D. L. 1987, *NRL Plasma Formulary*, NRL Publication 0084-4040, Naval Research Laboratory, Washington DC 20375-5000.

Brosius, J. W., Willson, R. F., Holman, G. D., and Schmelz, J. T. 1991, *Ap. J.*, submitted.

Brown, J. C. 1971, *Solar Physics*, **18**, 489.

Brown, J. C. 1974, in *Coronal Disturbances - I.A.U. Symposium No. 57*, 395, ed. Newkirk, G. (Boston: D. Reidel).

Brown J. C., Melrose, D. B., and Spicer, D. S. 1979, *Ap. J.*, **228**, 592.

Chubb, T. A., Kreplin, R. W., and Friedman, H. 1966, *J. Geophys. Res.*, **71**, 3611.

Cohen, R. H. 1976, *Phys. Fluids*, **19**, 239.

Connor, J. W., and Hastie, R. J. 1975, *Nucl. Fusion*, **15**, 415.

Crannell, C. J. 1989, in *Geophysical Monograph No.* **54**, 203, eds Waite, J. H. Jr., Burch, J. L., and Moore, R. L.

Crannell, C. J., Frost, K. J., Mätzler, C., Ohki, K., and Saba, J. L. 1978, *Ap. J.*, **223**, 620.

Crannell, C. J., Dulk, G. A., Kosugi, T., and Magun, A. 1988, *Solar Physics*, **118**, 155.

Culhane, J. L. 1969, *Mon. Not. R. Astr. Soc.*, **144**, 375.

deGroot, S. R., van Leeuwen, W. A., and van Weert, ChG. 1980, *Relativistic Kinetic Theory* (Amsterdam: North-Holland).

Dennis, B. R. 1988, *Solar Physics*, **118**, 49.

Dennis, B. R., and Schwartz, R. A. 1989, *Solar Physics*, **121**, 75.

Dreicer, H. 1959, *Phys. Rev.*, **115**, 238.

Dulk, G. A. 1985, *Ann. Rev. Astron. Astrophys.*, **23**, 169.

Dulk, G. A., and Marsh, K. A. 1982, *Ap. J.*, **259**, 350.

Emslie, A. G., and Vlahos, L. 1980, *Ap. J.*, **242**, 359.

Emslie, A. G., Coffey, V. N., and Schwartz, R. A. 1989, *Solar Physics*, **122**, 313.

Fuchs, V., Cairns, R. A., Lashmore-Davies, C. N., and Shoucri, M. M. 1986, *Phys. Fluids*, **29**, 2931.

Fuchs, V., Shoucri, M. M., Teichman, J., and Bers, A. 1988, *Phys. Fluids*, **31**, 2221.

Gary, D. E. 1985, *Ap. J.*, **297**, 799.

Gary, D. E., and Hurford, G. J. 1990, *Ap. J.*, **361**, 290.

Gary, D. E., Hurford, G. J., and Flees, D. J. 1991, *Ap. J.*, **369**, 255.

Gradshteyn, I. S., and Ryzhik, I. M. 1980, *Table of Integrals, Series, and Products* (Academic Press: New York).

Hagyard, M. J., Moore, R. L., and Emslie, A. G. 1984, *Adv. Space Res.*, 4, 71.

Hakim, R. 1967, *Phys. Rev.*, **162**, 128.

Holman, G. D. 1985, *Ap. J.*, **293**, 584.

Holman, G. D. 1986, in *Solar Flares and Coronal Physics Using P/OF as a Research Tool*, 150. NASA Conference Publication 2421, eds Tandberg-Hanssen, E., Wilson, R. M., and Hudson, H. S.

Holman, G. D., Kundu, M. R., and Kane, S. R. 1989, *Ap. J.*, **345**, 1050.

Holt, S. S., and Ramaty, R. 1969, *Solar Physics*, **8**, 119.

Kaastra, J. S. 1985, *Solar Flares: An Electrodynamic Model*, Ph.D. dissertation, University of Utrecht, The Netherlands.

Kane, S. R. 1974, in *Coronal Disturbances - I.A.U. Symposium No. 57*, 105, ed. Newkirk, G. (Boston: D. Reidel).

Karpen, J. T., Antiochos, S. K., and DeVore, C. R. 1990, *Ap. J. (Letters)*, **356**, L67.

Kiplinger, A. L., Dennis, B. R., Frost, K. J., and Orwig, L. E. 1984, *Ap. J. Lett.*, **287**, L105.

Klein, K.-L. 1987, *Astr. Ap.*, **183**, 341.

Koch, H. W., and Motz, J. W. 1959, *Rev. Mod. Phys.*, **31**, 920.

Kosugi, T., Dennis, B. R., and Kai, K. 1988, *Ap. J.*, **324**, 1118.

Kruskal, M., and Bernstein, I. B. 1962, in *Princeton Plasma Physics Laboratory Report No. MATT-Q-20*, 174.

Kulsrud, R. M., Sun, Y-C., Winsor, N. K., and Fallon, H. A. 1973, *Phys. Rev. Lett.*, **31**, 690.

Kundu, M. R. 1965, *Solar Radio Astronomy* (New York: John Wiley & Sons).

Kundu, M. R., Schmahl, E. J., Velusamy, T., and Vlahos, L. 1982, *Astr. Ap.*, **108**, 188.

Leach, J., and Petrosian, V. 1981, *Ap. J.*, **251**, 781.

Lin, R. P., and Hudson, H. S. 1976, *Solar Physics*, **50**, 153.

Lin, R. P., and Schwartz, R. A. 1987, *Ap. J.*, **312**, 462.

Lin, R. P., Schwartz, R. A., Pelling, R. M., and Hurley, K. C. 1981, *Ap. J. L:ett.*, **251**, L109.

Lu, E. T., and Petrosian, V. 1988, *Ap. J.*, **327**, 405.

Lu, E. T. and Petrosian, V. 1989, *Ap. J.*, **338**, 1122.

Lu, E. T. and Petrosian, V. 1990, *Ap. J.*, **354**, 735.

MacNeice, P. *et al.* 1991, in preparation.

Marsh, K. A., Hurford, G. J., Zirin, H., Dulk, G. A., Dennis, B. R., Frost, K. J., and Orwig, L. E. 1981, *Ap. J.*, **251**, 797.

Mätzler, C. 1978, *Astron. Astrophys.*, **70**, 181.

Meyer, J.-P. 1985, *Ap. J. Supp.*, **57**, 173.

Mikić, Z., Schnack, D. D., and Van Hoven, G. 1989, *Ap. J.*, **338**, 1148.

Moghaddam-Taaheri, E., Vlahos, L., Rowland, H. L., and Papadopoulos, K. 1985, *Phys. Fluids*, **28**, 3356.

Mok, Y. 1983, *Ap. J.*, **275**, 901.

Nitta, N., Kiplinger, A. L., and Kai, K. 1989, *Ap. J.*, **337**, 1003.

Nitta, N., White, S. M., Schmahl, E. J., and Kundu, M. R. 1991, *Solar Physics*, **132**, 125.

Nitta, N., White, S. M., Kundu, M. R., Gopalswami, N., Holman, G. D., Brosius, J. W., Schmelz, J. T., Saba, J. L. R., and Strong, K. T. 1991, *Ap. J.*, **374**, 374.

Prince, T. A., Hurford, G. J., Hudson, H. S., and Crannell, C. J. 1988, *Solar Physics*, **118**, 269.

Ramaty, R. 1969, *Ap. J.*, **158**, 753.

Ramaty, R., and Petrosian, V. 1972, *Ap. J.*, **178**, 241.

Singh, N. 1977, *Phys. Lett.*, **63A**, 307.

Spitzer, L., and Härm, R. 1953, *Phys. Rev.*, **89**, 977.

Stäli, M., Gary, D. E., and Hurford, G. J. 1989, *Solar Phys.*, **120**, 351 (SGH1).

Stäli, M., Gary, D. E., and Hurford, G. J. 1990, *Solar Phys.*, **125**, 343 (SGH2).

Syrovatskii, S. I. 1981, *Ann. Rev. Astr. Ap.*, **19**, 163.

Takakura, T. 1960, *Pub. Astron. Soc. Japan*, **12**, 352.

Takakura, T., and Scalise, E. 1970, *Solar Phys.*, **11**, 434.

Tamor, S. 1978, *Nucl. Fusion*, **18**, 229.

Tamor, S. 1979, *Nucl. Fusion*, **19**, 455.

Tandberg-Hanssen, E., and Emslie, A. G. 1988, *The Physics of Solar Flares*, (Cambridge University Press).

Trulsen, J., and Fejer, J. A. 1970, *J. Plasma Phys.*, **4**, 825.

Tucker, W. H. 1975, *Radiation Processes in Astrophysics* (Cambridge: MIT Press).

van Ballegooijen, A. A. 1985, *Ap. J.*, **298**, 421.

Velusamy, T., and Kundu, M. R. 1982, *Ap. J.*, **258**, 388.

Venkatakrishnan, P., Hagyard, M. J., and Hathaway, D. H. 1988, *Solar Physics*, **115**, 125.

Wiehl, H. J., Batchelor, D. A., Crannell, C. J., Dennis, B. R., Price, P. N., and Magun, A. 1985, *Solar Physics*, **96**, 339.

Wiley, J. C., and Hinton, F. L. 1980, *Phys. Fluids*, **23**, 921.

Wiley, J. C., Choi, D-I., and Horton, W. 1980, *Phys. Fluids*, **23**, 2193.

Willson, R. F., Klein, K-L, Kerdraon, A., Lang, K. R., and Trottet, G. 1990, *Ap. J.*, **357**, 662.

Zheleznyakov, V. V. 1970, *Radio Emission of the Sun and Planets*, ed. J. S. Hey (Oxford: Pergamon Press).

INTEGRATED PLANT

1. AGENCY USE ONLY (Leave blank)	2. REPORT DATE December 1991	3. REPORT TYPE AND DATES COVERED Technical Memorandum

4. TITLE AND SUBTITLE	5. FUNDING NUMBERS
A Thermal/Nonthermal Approach to Solar Flares	JON 680-030-09-0101

6. AUTHOR(S)

Stephen G. Benka

7. PERFORMING ORGANIZATION NAME(S) AND ADDRESS(ES)	8. PERFORMING ORGANIZATION REPORT NUMBER
NASA-Goddard Space Flight Center Greenbelt, Maryland 20771	91A02175

9. SPONSORING/MONITORING AGENCY NAME(S) AND ADDRESS(ES)	10. SPONSORING/MONITORING AGENCY REPORT NUMBER
National Aeronautics and Space Administration Washington, D.C. 20546-0001	NASA TM-4323

11. SUPPLEMENTARY NOTES

Stephen G. Benka--current address: E.O. Hulbert Center for Space Research; Code 4170, Naval Research Laboratory, Washington, D.C. 20375.

12a. DISTRIBUTION/AVAILABILITY STATEMENT	12b. DISTRIBUTION CODE
Unclassified - Unlimited Subject Category 92	

13. ABSTRACT (Maximum 200 words)

A new approach for modeling solar flare high-energy emissions is developed in which both thermal and nonthermal particles coexist and contribute to the radiation. The thermal/nonthermal distribution function is interpreted physically by postulating the existence of DC sheets in the flare region. The currents then provide both primary plasma heating through Joule dissipation, and runaway electron acceleration. The physics of runaway acceleration is discussed. Several methods are presented for obtaining approximations to the thermal/nonthermal distribution function, both within the current sheets and outside of them. Theoretical hard X-ray spectra are calculated, allowing for thermal bremsstrahlung from the heated plasma electrons impinging on the chromosphere. A simple model for hard X-ray images of two-ribbon flares is presented. Theoretical microwave gyrosynchrotron spectra are calculated and analyzed, uncovering important new effects caused by the interplay of thermal and nonthermal particles. The theoretical spectra are compared with observed high-resolution spectra of solar flares, and excellent agreement is found, in both hard X-rays and microwaves. The future detailed application of this approach to solar flares is discussed, as are possible refinements to this theory.

14. SUBJECT TERMS			15. NUMBER OF PAGES 112
Sun, Flares, Bursts, X rays, Microwaves, Current Sheets, Runaway Electrons, Thermal, Nonthermal			16. PRICE CODE A06

17. SECURITY CLASSIFICATION OF REPORT	18. SECURITY CLASSIFICATION OF THIS PAGE	19. SECURITY CLASSIFICATION OF ABSTRACT	20. LIMITATION OF ABSTRACT
Unclassified	Unclassified	Unclassified	

PRECEDING PAGE BLANK NOT FILMED

INTENTIONALLY BLANK